Real-time Spatial-phase-locked Electron-beam Lithography

by

Feng Zhang

Submitted to the Department of Electrical Engineering and Computer Science
in partial fulfillment of the requirements for the degree of

Doctor of Science

at the

MASSACHUSETTS INSTITUTE OF TECHNOLOGY

September 2005

© Massachusetts Institute of Technology 2005. All rights reserved.

Author ....
Department of Electrical Engineering and Computer Science
September 09, 2005

Certified by.......................................
Henry I. Smith
Joseph F. and Nancy P. Keithley Professor of Electrical Engineering
Thesis Supervisor

Accepted by... ....
Arthur C. Smith
Chairman, Department Committee on Graduate Students

BARKER

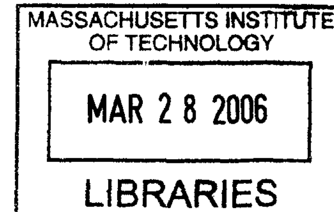

Real-time Spatial-phase-locked Electron-beam Lithography

by

Feng Zhang

Submitted to the Department of Electrical Engineering and Computer Science
on September 09, 2005, in partial fulfillment of the
requirements for the degree of
Doctor of Science

Abstract

The ability of electron-beam lithography (EBL) to create sub-10-nm features with arbitrary geometry makes it a critical tool in many important applications in nano-scale science and technology. The conventional EBL system is limited by its poor absolute-placement accuracy, often worse than its resolution. Spatial-phase-locked electron-beam lithography (SPLEBL) improves the placement accuracy of EBL tools to the nanometer level by directly referencing the beam position via a global-fiducial grid placed on the substrate, and providing feedback corrections to the beam position. SPLEBL has several different modes of operation, and it can be applied to both scanning electron-beam lithography (SEBL) and variable-shaped-beam lithography. This research focuses primarily on implementing real-time SPLEBL in SEBL systems.

Real-time SPLEBL consists of three major components: a fiducial-reference grid, a beam-position detection algorithm and a partial-beam blanker. Several types of fiducial grids and their fabrication processes were developed and evaluated for their signal-to-noise ratio and ease of usage. An algorithm for detecting the beam position based on Fourier techniques was implemented, and $\sim$1 nm placement accuracy achieved. Finally, various approaches to partial-beam blanking were examined, and one based on an electrostatic quadrupole lens was shown to provide the best performance.

Thesis Supervisor: Henry I. Smith
Title: Joseph F. and Nancy P. Keithley Professor of Electrical Engineering

Acknowledgments

I am deeply thankful to my advisors, Professor Hank Smith and Dr. James Goodberlet, for introducing me to the interesting world of nanolithography and nanofabrication. James provided much guidance during the early stages of my research, which helped me tremendously in understanding the subject. Hank gave me the oppertunity to conduct my research independently, yet he was available whenever help was needed. His extraordinary knowledge and creative ideas have assisted me in overcoming many obstacles in my research. His rigorous thinking and methodology have taught me how to be a better scientist and engineer. His great enthusiasm towards science and technology inspires everyone who works around him. I would like to thank the members of my thesis committee, Professor Tayo Akinwande, Professor Rajeev Ram and Dr. Mark Schattenburg, for their insightful questions and helpful comments about my work.

It has been an extremely rewarding experience for me to work with a group of exceptionally talented people in the NanoStructures Laboratory at MIT. I have worked closely with Todd Hastings, Mark Finlayson, Cynthia Caramana and Sander Smits on the same project. The staff of the NanoStructures Lab, Jimmy Carter, Jim Daley and Mark Mondol, have taught me the usage of many pieces of the equipment in the lab. Lengthy discussions with Minghao Qi, Euclid Moon, Rajesh Menon, Mike Walsh, Tim Savas, Amil Patel, Joy Cheng, Dario Gil and many others have been an eye opener for me. Cindy Gibbs has helped me with much of the administrative work. Serving with Minghao as the network adminstrators for the group has also been a very interesting experience for me.

Finally, I would like to thank my wife, Ji Chen, my parents and grandparents for their unconditional love and support throughout my life.

Contents

1 Introduction **15**

1.1 Electron-beam lithography 17

1.1.1 Scanning-electron-beam Lithography 19

1.1.2 Variable-shaped-beam Lithography 24

1.1.3 Electron-projection Lithography 26

1.1.4 Absolute Pattern-placement Accuracy 26

1.2 Spatial-phase-locked Electron-beam Lithography 29

2 Reference Signal & Fiducial Grid **33**

2.1 Reference-signal Generation 34

2.1.1 Secondary Electrons 34

2.1.2 Scintillation Signal 39

2.1.3 Backscattered Electrons 40

2.1.4 Characteristic X-rays & Auger Electrons 40

2.1.5 Noise Analysis 41

2.2 Lithographic Techniques 43

2.2.1 Conventional Interference Lithography 43

2.2.2 Scanning-beam Interference Lithography 47

2.2.3 Near-field Interference Lithography 49

2.2.4 Achromatic Interference Lithography 52

2.2.5 Nanoimprint Stamping 53

2.3 Secondary-electron Grid 55

2.3.1 Grid Material 57

2.3.2 Al Grid 59
2.3.3 Cu Grid 64
2.3.4 Signal Contrast Measurement 67
2.4 Scintillation Grid 69
2.4.1 Scintillation-signal Detection 69
2.4.2 Scintillation Materials 70
2.4.3 Scintillation Signal Analysis 72

3 Electron-beam-position Detection 75
3.1 Parametric Estimator of a Sinusoidal Signal 76
3.1.1 Unbiased Estimator 76
3.1.2 Cramér-Rao Bound 77
3.1.3 Phase Estimation 78
3.2 Spatial-phase-locking Algorithm 84
3.3 Estimation Accuracy with SE Signal 90
3.3.1 SNR Calculation of SE Signal 90
3.4 Implementation of Spatial-phase Locking 92
3.4.1 Experimental Results 97

4 Partial Beam Blanker 101
4.1 Conventional E-beam Blanker 101
4.2 Partial-beam-blanking via Time Modulation 103
4.3 Partial-beam-blanking via Beam Shift 104
4.4 Partial-beam-blanking via Beam Expansion 106
4.4.1 Electrostatic Quadrupole Lens 107
4.4.2 Design Procedure and Considerations 116

5 Conclusion 119

A The Phase and the Periodogram of a Sinusoidal Signal 123

B Trajectory Equations for Electrons 125

List of Figures

1-1 Schematics for an electron-beam lithography system. 19
1-2 Schematics for a scanning-electron-beam lithography system. 20
1-3 EBL exposure strategies. 23
1-4 Raster scan vs. vector scan. 24
1-5 Beam formation for variable-shaped EBL. 25
1-6 Schematic of PREVAIL. 27
1-7 Overview of the evolution of EBL. 28
1-8 Placement errors in SEBL. 29
1-9 SPLEBL overview. 31

2-1 Energy distribution of electron-induced emission. 35
2-2 SE yield vs primary-beam energy. 35
2-3 Secondary-electron generation. 37
2-4 In-lens detector. 38
2-5 Signal path in SPLEBL. 41
2-6 Interference lithography. 44
2-7 Conventional interference lithography. 45
2-8 Lloyd's mirror configuration. 46
2-9 Spatial-phase error plot. 47
2-10 Scanning-beam interference lithography. 48
2-11 Exposure strategy for SBIL. 49
2-12 Near-field interference lithography. 50
2-13 Achromatic interference lithography. 52

2-14 Mask design for AIL. 53
2-15 Nanoimprint stamping. 55
2-16 Resist stack for SPLEBL. 56
2-17 Evaporated C_{60} film on Si substrate. 58
2-18 Al grid fabrication process. 60
2-19 SEM images of an Al grid. 61
2-20 Photochemically etched Al gratings. 63
2-21 Cu-grid-fabrication process. 64
2-22 SEM images of a Cu grid. 65
2-23 Vertical standing wave in IL exposure. 66
2-24 Exposure results through Cu grid. 66
2-25 Contrast measurements for the Al and Cu grids. 68
2-26 The scintillation-signal detector on VS2A. 70
2-27 The scintillation-signal detector on Raith 150. 71

3-1 Periodogram power density. 82
3-2 Cramér-Rao bound simulation. 83
3-3 Orthogonal grid. 85
3-4 Rotated orthogonal grid. 85
3-5 Spectrum contents of a rotated Al grid. 87
3-6 Schematic diagram of the control system for SPLEBL. 93
3-7 Hardware configuration of the spatial-phase locking system. 94
3-8 Distortions in the electron optics. 95
3-9 Multi-block-estimator implementation. 96
3-10 Exposing patterns for field-stitching test. 97
3-11 Exposing layout for field-stitching test. 98
3-12 Stitching error measurements. 99

4-1 Conventional beam blanker. 102
4-2 Double-deflection blanker. 104
4-3 Quadruple-deflection partial-beam blanker. 105

4-4 Beam current modulation via round lens. 106
4-5 3-D structure of an electrostatic quadrupole lens. 108
4-6 Schematic of a quadrupole-lens-based partial-beam blanker. 112
4-7 Partial-beam blanker test setup. 114
4-8 Fluorescent images of an e-beam through a quadrupole-lens-based partial-beam blanker. 115
4-9 Simulation of a quadrupole-lens-based partial-beam blanker. 117

List of Tables

1.1 Image placement requirements for masks in ITRS. 16

1.2 Physical characteristics of different types of electron sources. 21

2.1 Yields and signal quanta for the signal path of SE. 42

2.2 Recipe of photoechant for Al. 63

3.1 Assumed exposure parameters for the SNR calculation. 92

Chapter 1

Introduction

The classic talk given by Nobel Laureate Richard Feynman on December 29th 1959, titled "There is plenty of room at the bottom," marked a new era of miniaturization [a]. Since then, new technologies have been developed to make devices with extremely small sizes, and miniaturization has brought us smaller, lighter, more powerful and more reliable products. Today, manufacturers can make personal-computing devices that fit into one's palm, yet are orders of magnitude faster and more powerful than early-generation computers that filled up rooms. Doctors can conduct diagnosis on a small chip quickly and accurately with little inconvenience to the patients. Engineers and scientists can build higher quality and lighter space-telescopes to better explore and understand the universe. Advances in microprocessor, wireless and optical communication, and storage technologies have revolutionized the way people process, exchange and store information. These products have fundamentally changed myriad aspects of our lives.

By adopting the planar-fabrication process, where devices are built in a layer-by-layer fashion, the semiconductor industry has succeeded in following Moore's Law over the past several decades. While the minimum feature size on a chip has shrunk from tens of microns to sub-micron, and is now approaching nanometer scale, system performance has improved substantially. As the feature sizes are becoming much

[a] Buck et al. at MIT had started some of the earliest research in microlithography about one year prior to Feynman's speech [7].

smaller than the exposure wavelength, traditional photolithography is reaching its physical limit. Several new technologies have been introduced, referred to as the next-generation lithography (NGL), to replace photolithography. Among these technologies, nanoimprint lithography (NIL), electron-projection lithography (EPL) and extreme-UV lithography (EUVL) are the most actively pursued. These three technologies have one thing in common with photolithography: they all require masks or templates for pattern transfer, and the quality of the masks or templates directly affects the quality and the yield of the final product.

Electron-beam lithography (EBL) plays a vital role in mask fabrication for photolithography because of its ability to create patterns with arbitrary geometry and nanometer resolution. Despite its superior resolution, EBL suffers from poor pattern-placement accuracy, and pattern-placement errors on the masks are a major contributor to overlay errors in the planar-fabrication process. Currently, state-of-the-art ELB tools can not achieve absolute placement accuracy better than 10 nm, which is worse than their resolution. According to the 2004 edition of the International Technology Roadmap for Semiconductors (ITRS) [1], current manufacturing tools will be inadequate to meet pattern-placement-error requirements for EPL and EUVL masks by 2008 and 2012, respectively. Although no such requirements have been given for NIL in ITRS, it is expected to be much more stringent as NIL offers no imaging reduction. Table 1.1 provides the image-placement requirements for EUVL and EPL masks for the years of 2008 through 2017.

	2008	2009	2010	2011	2012	2013	2014	2015	2016	2017
Node	65	65	45	45	45	32	32	32	22	22
EUVL	13	12	11	10	9	8	7	6	6	5
EPL	9	8.5	8	7	6	5.5	5	4.5	4	3.8

Table 1.1: Image placement specifications for EUVL and EPL masks adapted from the International Technology Roadmap for Semiconductors [1]. All units are in nanometers. (yellow) Manufacturable solutions are known but not optimized. (red) Manufacturable solutions are NOT known.

Besides mask fabrication, EBL plays an equally important role for direct-write in

many small-volume-device productions. One important example is integrated-optical devices for future generation communication systems. Several types of these optical devices, e.g. designed defects in 3-D photonic crystals, and Bragg-grating-based add-drop filters, require pattern-placement accuracy below 1 nm. These requirements are far beyond what can be achieved by conventional EBL tools.

A novel technology, called spatial-phase-locked electron-beam lithography, or SPLEBL for short, was developed at MIT to achieve absolute-placement accuracy of ~1 nm in EBL systems.

1.1 Electron-beam lithography

Modern electron optics began in 1925 when Louis de Broglie proposed the particle-wave duality theory, which associated wave properties with moving particles, including electrons. Hans Busch later demonstrated that the action of an axially symmetric coil on moving electrons was analogous to that of a spherical lens on light. Based on these theories, Knoll and Ruska built the first transmission electron microscope (TEM) in 1932. In TEM, a specimen is illuminated by a collimated, high-energy-electron beam, and a phase image of the specimen is magnified and projected by a series of objective lenses onto either a fluorescent screen or a recording medium for examination. The specimen used for TEM must be extremely thin, because electrons quickly loose energy, and hence change wavelength, as they traverse solid materials.

As early as 1935, a very different type of electron microscope, the scanning-electron microscope (SEM), was described by Knoll. In 1938, von Ardenne constructed the first scanning-transmission-electron microscope (STEM) by adding scan coils to a transmission electron microscope. STEM utilized a finely focused-electron beam to raster scan across a thin specimen, and the transmitted-electron signal was detected along the scan. An image was formed by plotting the intensity of the transmitted-electron signal as brightness on a recording medium in a similar two-dimensional raster scan. The first SEM that could be used to observe the surfaces of thick, solid specimens was constructed by Zworykin et al. in 1942, but it was the work of Oatley

and his students in the following two decades at the University of Cambridge that greatly improved the performance of the SEM and made the technology feasible for commercialization.

The major difference between STEM and SEM is that SEM generally uses secondary electrons (SE) instead of transmitted electrons to form images, and, unlike transmitted electron, SE are emitted from the same surface that the electron beam enters the specimen. Hence, the thickness of the sample is no longer an issue. SEM provides easy sample preparation, large depth of focus, readily interpreted images, and great flexibility in the size and type of specimen. Today, SEM has become one of the most widely used instruments in scientific research.

The concept of using an energetic electron-beam (e-beam) to conduct lithography was developed in the 1960s [5, 46], and it was considered at the time as a replacement for photolithography for producing extremely fine and complex patterns [39]. The advantages of EBL over photolithography are its flexibility and resolution. Since the wavelength of high-energy electrons is extremely short, e.g. only 3.7 pm for 100 keV electrons, EBL systems are not diffraction-limited.

EBL creates patterns by exposing a sample covered with a thin film of resist to an energized e-beam. The e-beam resist is a material whose solubility in a particular solvent (i.e., the developer) is sensitive to electron irradiation. If the exposed resist becomes more soluble, it is a positive resist, otherwise, it is a negative resist.

There are three forms of EBL: scanning-electron-beam lithography (SEBL), variable-shaped-beam lithography (VSBL), and electron-projection lithography (EPL). Figure 1-1 shows the major components in a typical EBL system: 1) an electron source that generates a beam of electrons, 2) an electron-optical column that accelerates, conditions and projects the beam onto the sample, 3) a laser-interferometer-controlled stage that accurately drives the sample to the desired location, 4) a vacuum system that encloses the before-mentioned components, and 5) control electronics that command and coordinate the operation of various components. The entire electron path must be kept in vacuum because electrons do not travel very far in air.

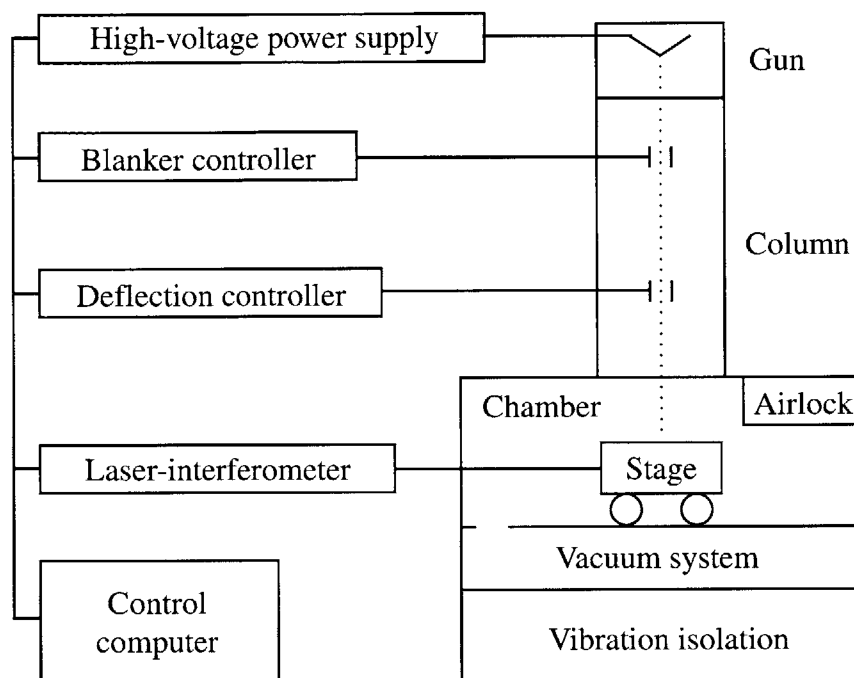

Figure 1-1: Schematics for an electron-beam lithography system. The left-hand side shows a high-voltage power supply for the gun and various control electronics. The right-hand side shows an electron-gun assembly, an electron-optical column, a vacuum chamber, a laser-interferometer-controlled stage and a vibration-isolation platform. A deflection system is used to move the beam to the desired position, and a beam blanker to turn the beam on and off.

1.1.1 Scanning-electron-beam Lithography

A scanning-electron-beam-lithography (SEBL) system operates in a fashion similar to that of an SEM. It uses a finely focused electron beam, typically one to several nanometers, to expose patterns. Figure 1-2 depicts the major electron-optical components in an SEBL system. Since the beam-current density generally has a Gaussian distribution, such systems are sometimes called "Gaussian-beam" systems.

The e-beam is generated by one of three methods: thermal emission, cold-field emission, or Schottky emission. The key parameters of the source that are important to SEBL are its brightness, its emission stability, the energy spread of the electrons, and the virtual source size. Table 1.2 summarizes emission properties of the different types of sources. Thermal emission happens when the source material is heated to

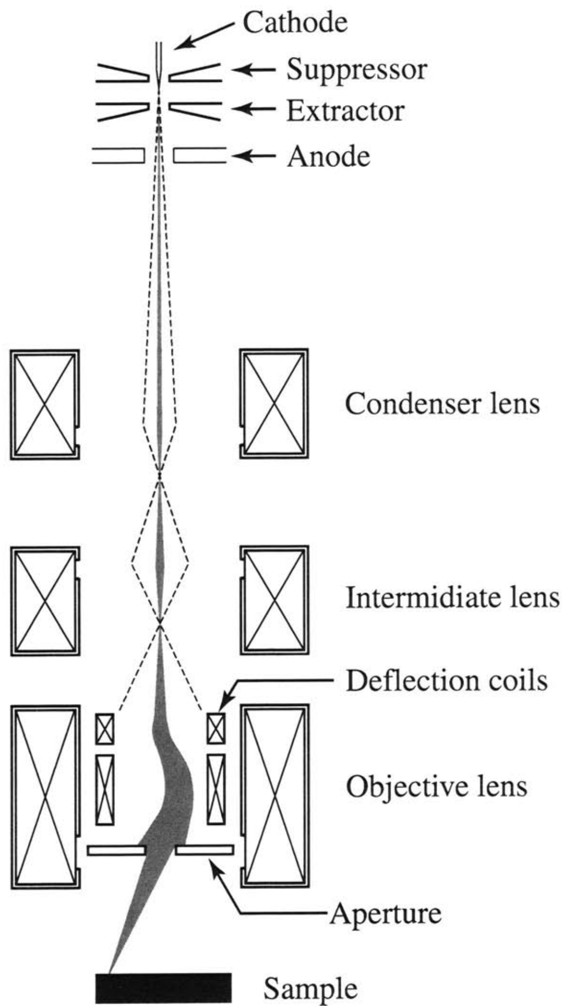

Figure 1-2: Schematics for a scanning-electron-beam lithography (SEBL) system. The configuration shown at the very top is typical for thermal-field-emission sources. The various lenses demagnify and focus the e-beam to form a very small probe at the sample. The deflection coils drive the beam to desired positions on the sample. The beam blanker, which is used to turn the beam on and off, is not shown in this figure.

	Tungsten	LaB_6	Schottky (thermal-field)	Cold-field
Brightness ($A/cm^2/sr$)	10^6	10^7	10^8	10^9
Energy spread (eV)	$1-2$	$1-2$	$0.3-1$	$0.2-0.3$
Virtual source size (nm)	$> 10^4$	10^4	15	3
Short-term beam-current stability (%RMS)	< 1	< 1	< 1	$4-6$
Vacuum (Torr)	10^{-6}	10^{-8}	10^{-9}	10^{-10}
Life time	> 1 yr	> 1 yr	1000 hrs	100 hrs

Table 1.2: Physical characteristics of different types of electron sources.

the point where the electrons gain enough energy to overcome the work function and "boil" off the surface of the source. For thermionic sources, high brightness requires high operating temperature, but higher temperature results in greater energy spread and shorter life-time. Furthermore, not many materials can stand up to the temperatures required by thermal emission. The best candidates are tungsten (W, operates at 2700 K) and lanthanum hexaboride (LaB_6, operates at 1800 K). Comparing with the other two types of sources, thermionic sources suffer from low brightness and short life-time.

Cold-field emission, also known as Fowler-Nordheim tunnelling, is a process in which electrons tunnel through the barrier between the cathode and the vacuum in the presence of an intense electric field. The high intensity of the field is obtained by using an extremely sharp cathode tip. The fine geometry of the tip also contributes to its high brightness. Low temperature operation is both advantages and disadvantages. On the one hand, it provides long life-time for the source and small energy spread for the beam. On the other hand, it allows absorption of residual gas molecules in the vacuum chamber onto the cathode surface, which changes the emission properties of the cathode. Momentarily flashing the tip (i.e. heating it up) helps to clean it, but reabsorption quickly happens again. In addition, gas molecules may be ionized by energized electrons and attracted by the cathode, causing physical sputtering of the

cathode. The sputtering process gradually changes the shape of the cathode and alters its emission properties. Ultra-high vacuum required at the source can reduce, but not eliminate, the sputtering process. The poor long-term stability makes field-emission sources unsuitable for EBL.

Schottky emission, or thermal-field emission, combines the best of both worlds. It utilizes a sharp tungsten tip to obtain high brightness, and it operates at ~1800 K to achieve long-term stability. To further reduce the work-function barrier, the tip surface is coated with zirconium oxide (ZrO). A reservoir of ZrO is located at the upper portion of the cathode. During operation ZrO melts and flows down to the tip and replenishes the evaporated material. Because of its superior performance, modern EBL tools use almost exclusively thermal-field emission sources. Figure 1-2 shows a typical configuration for thermal-field sources.

Once leaving the cathode surface, the e-beam is accelerated, collimated and focused onto the sample by various lenses in the electron-optical column. The lenses are usually rotationally symmetric and can be either electrostatic or magnetic. Electrostatic lenses have worse aberrations than magnetic ones, and hence they are rarely used in commercial EBL systems. They are often used in multi-beam systems where multiple e-beams are bundled together, and the space becomes very limited, making magnetic lenses impractical. Electron lenses generally have much worse aberrations than their optical counterparts because they rely on fields to focus electrons, and in most cases they can be made only to converge, not to diverge. Stigmators are used for correcting various types of aberrations. They are non-rotationally symmetric lenses consisting of multiple pairs of pole pieces. The complexity in the design and fabrication of stigmators limits their usage.

A deflection system is used to steer the beam across the sample, and as for the lens, it can be either electrostatic or magnetic. Electrostatic deflection systems have much faster dynamic response than magnetic ones, but they suffer from worse aberration. High-end EBL tools often adopt multi-stage-deflection systems where long-range deflection is done magnetically to minimize abberation while short-range deflection is done electrostatically for high-speed operation. When deflected off the optical axis,

aberrations in the optics cause the beam shape to deteriorate rapidly. Hence, the deflection-field size is very limited. To expose large patterns, one of two strategies can

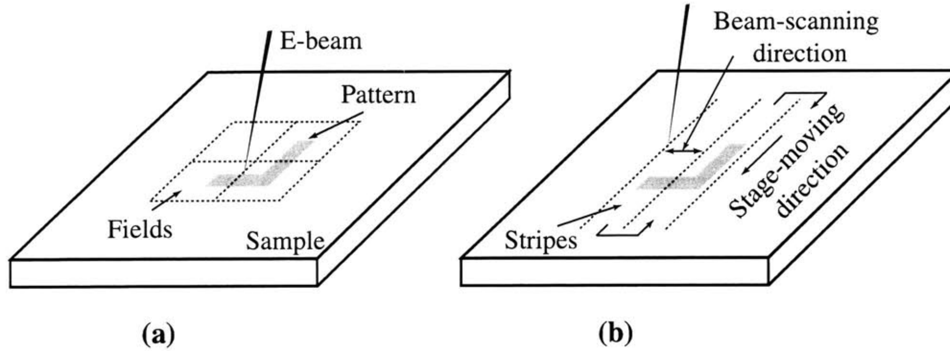

Figure 1-3: Exposure strategies. **(a)** Step-and-repeat where the target area is divided into fields, and the fields are exposed one at a time. **(b)** Continuous scan where the target area is divided into stripes. The beam scans across the stripes while the stage moves continuously. A laser-interferometer-controlled stage is used to precisely move the samples in both cases.

be adopted as illustrated in Fig. 1-3. The step-and-repeat strategy is the more widely used one, in which the target area is divided into square fields, typically hundreds of microns in size, and the fields are exposed one at a time. A laser-interferometer-controlled stage moves the sample from field to field. The other strategy, named continuous scan, is to scan the beam across the sample in stripes while the stage moves continuously in the perpendicular direction. To facilitate easy pattern processing, the field, or the stripe, is addressed in pixels. The distance between two adjacent pixels is defined as the step size, and the number of addressable pixels is determined by the bit number of DAC in the control electronics.

The beam can be turned on and off by a beam blanker. For any reasonable exposure speed (i.e., greater than 1 MHz), an electrostatic beam blanker is used. In high-speed EBL systems there are usually two intermediate focal points, or beam crossovers. One of the crossovers is to facilitate fast beam-blanking. The other one, combined with a pair of zoom lenses, is to provide precise beam-current control (refer to Chapter 4 for more details).

SEBL has two modes of operation: the raster-scan mode and the vector-scan mode

(Fig. 1-4). In the raster mode, the beam scans over the deflection field in a line-by-line

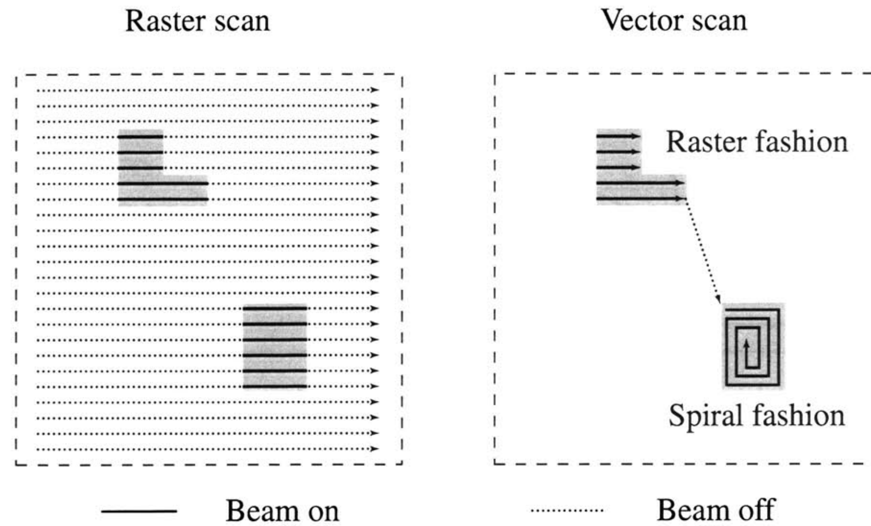

Figure 1-4: Raster scan vs. vector scan. In raster-scan mode, the beam sweeps over the entire deflection field, and patterns are exposed by turning the beam on and off. In the vector-scan mode, the beam only scans over the patterned areas. Patterns can be exposed in either a raster fashion or a spiral fashion.

fashion, similar to that in the CRT tube of a television. The patterns are exposed by appropriately switching the beam on and off. In the vector-scan mode, only the patterns are exposed. Each pattern can be exposed in either a raster fashion or a spiral fashion. Any stage error measured by the laser interferometer can be corrected by the deflection system.

A pattern generator translates the pattern layout into control signals to the deflection system, the beam blanker, and the stage. For large and complicated layouts written in highly descriptive formats, preprocessing can be done to convert them to a format more compatible with the hardware, which will significantly reduce the exposure time.

1.1.2 Variable-shaped-beam Lithography

Gaussian-beam systems are inherently very slow because patterns are delineated by a tightly focused beam in a pixel-by-pixel fashion, and the writing speed is limited by

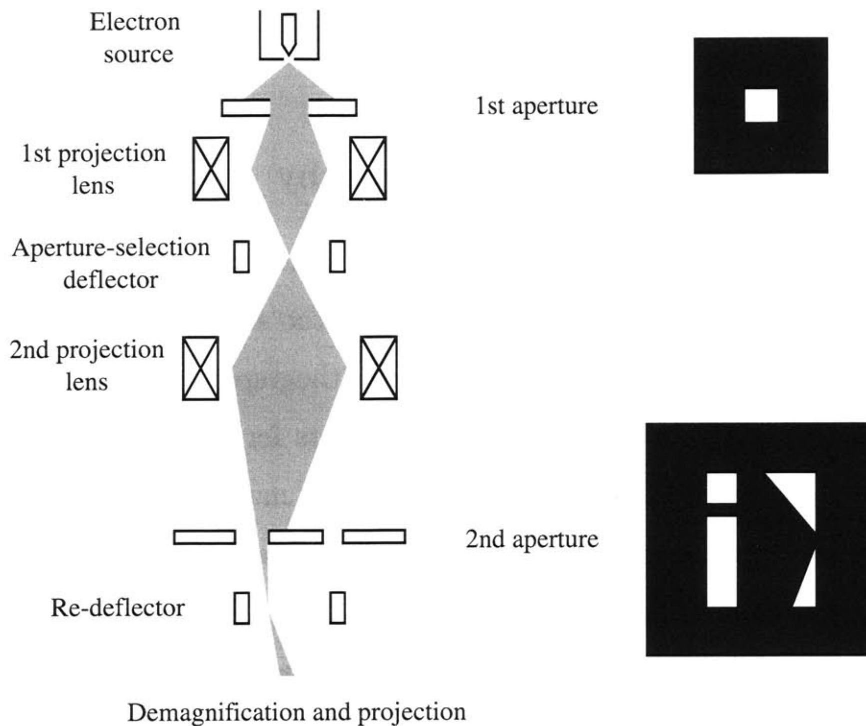

Figure 1-5: Beam formation for variable-shaped EBL. The first aperture is used to form a square beam. The projection lenses project the beam onto the second aperture plate that consists of various shapes. The deflector determines which shape the beam will pass through and by how much. The top view of the aperture plates are shown on the right, and the dimensions of the apertures are much greater than in reality for illustration purposes. The projection part of the system is not shown in the figure.

the maximum deflection speed and the step size. Variable-shaped-beam systems were designed to speed up the process by exposing groups of pixels in the form of primitive shapes such as triangles and rectangles [55, 54, 47, 49]. Each shape typically contains hundreds of pixels. The primitive shapes are obtained by passing the e-beam through two aperture plates as illustrated in Fig. 1-5. The upper aperture is a square, and the lower one consists of various shapes and sizes [64].

The beam is first squared out by the upper aperture, and it is then projected onto the lower aperture by the projection lenses. A deflector above the lower aperture is used to select the shape to be used and the amount of overlapping. The properly shaped beam is then deflected back, demagnified, and projected onto the sample.

Patterns are segmented into primitive shapes, and the shapes are exposed one-by-one in a vector-scan style.

1.1.3 Electron-projection Lithography

VSBL systems are widely used in optical-mask fabrication for their high resolution and medium throughput. They are, however, still too slow for device fabrication for the semiconductor industry. E-beam projection lithography (EPL) was developed as a solution for meeting the throughput requirements for production [33]. Although EPL was invented much earlier [5], it did not attract much attention until the 1990s.

Similar to an optical-projection systems, an EPL system images a mask, or reticle, onto the substrate by using a properly shaped e-beam. The size of the beam is significantly larger than that used in SEBL or VSBL. Two forms of EPL that have been most actively pursued are SCattering with Angular Limitation in Projection E-beam Lithography (SCALPEL [4]) and PRojection Exposure with Variable Axis Immersion Lenses (PREVAIL [56]). The major difference between them is that SCALPEL uses thin membrane masks, and PREVAIL uses stencil masks. Figure 1-6 shows the schematic of PREVAIL. A beam of $\sim 25\,\text{mm}^2$ containing 10^{11} pixels is used to scan the mask [14]. The pattern on the reticle is divided into small "cells" that are on the order of 1μm is size to facilitate supporting struts for the thin stencil mask. An overview of the evolution of EBL is provided in Fig. 1-7.

1.1.4 Absolute Pattern-placement Accuracy

Pattern-placement accuracy is a measurement of an EBL system's ability to place patterns on a substrate with respect of their intended locations. In conventional EBL, the position of the e-beam is calibrated against registration marks on the sample prior to the exposure. During exposure, the beam position is inferred from that of the laser-interferometer-controlled stage. Although the position of the stage can be measured with an accuracy of less than 1 nm, the beam can drift relative to the sample due to external disturbances including mechanical vibration, electromagnetic interference,

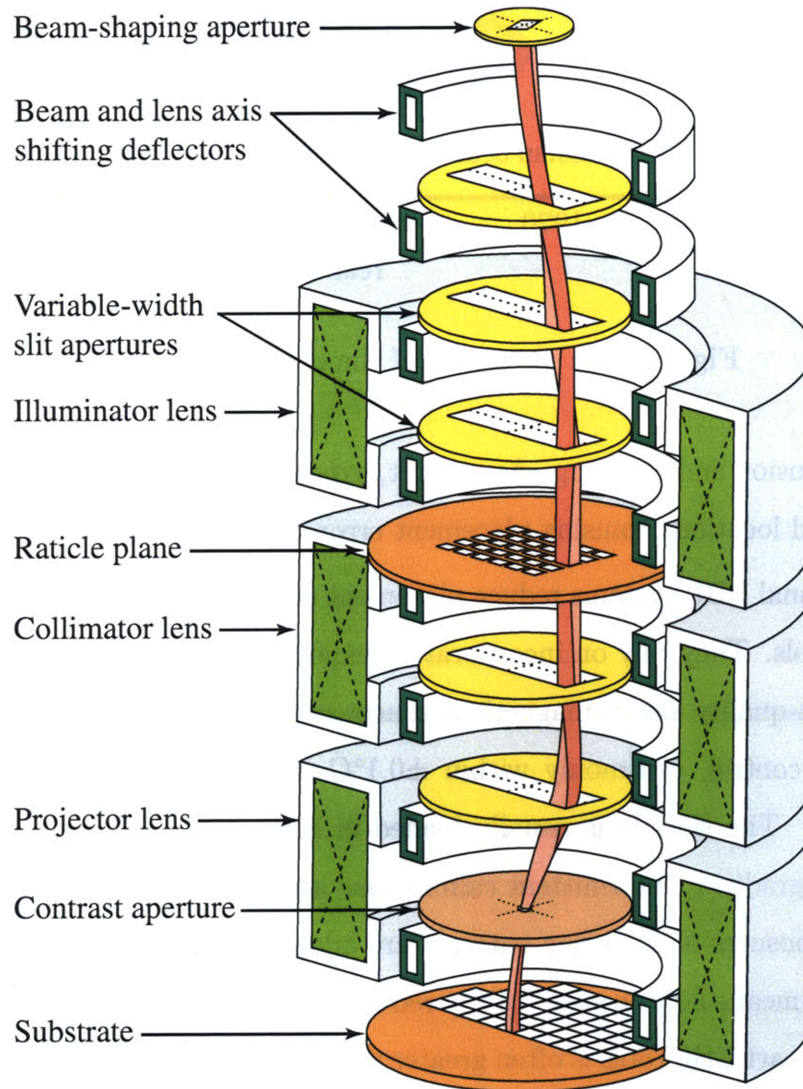

Figure 1-6: Schematic of PREVAIL. The image on the reticle is projected onto the wafer by a square-shaping e-beam. The pattern on the reticle is separated into "cells" to facilitate supports for the stencil mask.

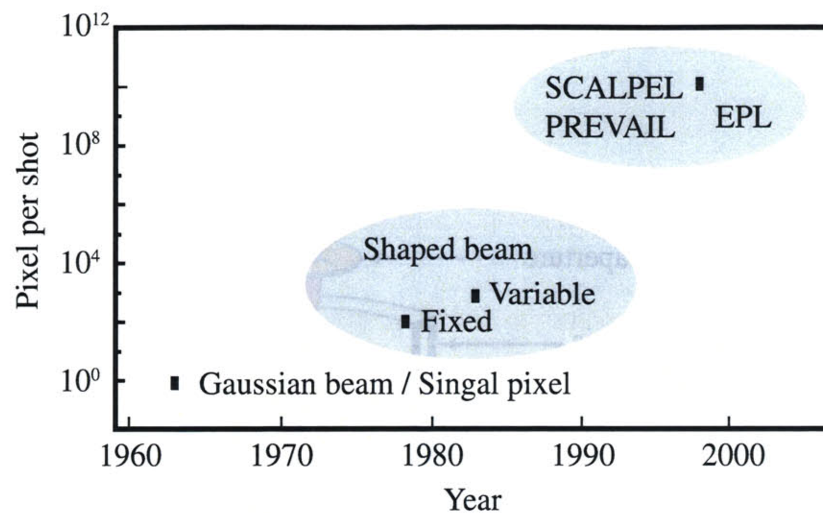

Figure 1-7: Overview of the evolution of EBL.

thermal expansion and charging. As a result, exposed patterns can be misplaced from their intended locations, causing placement errors.

Conventional EBL systems reduce placement errors by tightening up the environmental controls. They rely on incorporating expensive vibration-isolation platforms, applying high-quality electromagnetic and acoustic shielding, and adopting stringent temperature control, commonly within $\pm 0.1°C$. Special procedures must be taken for exposure. The sample is usually loaded-in hours before the exposure to avoid temperature gradient, intermittent calibrations are conducted during exposure, and multipass exposures of the same patterns are adopted to average out the errors. Although these means help to significantly reduce the disturbances, the placement error of state-of-the-art EBL tools is often greater than 10 nm (3σ) [65, 48], a number worse than their resolution.

The frequency contents of the disturbances range from several hundred hertz to well below 1 Hz, depending on the nature of the sources. High frequency noises are much easier to deal with than low frequency ones. Depending on their locations, placement errors can be categorized as inter-field distortion and intra-field distortion, as depicted in Fig. 1-8.

Intrafield distortion occurs within one deflection field. It can be a combination

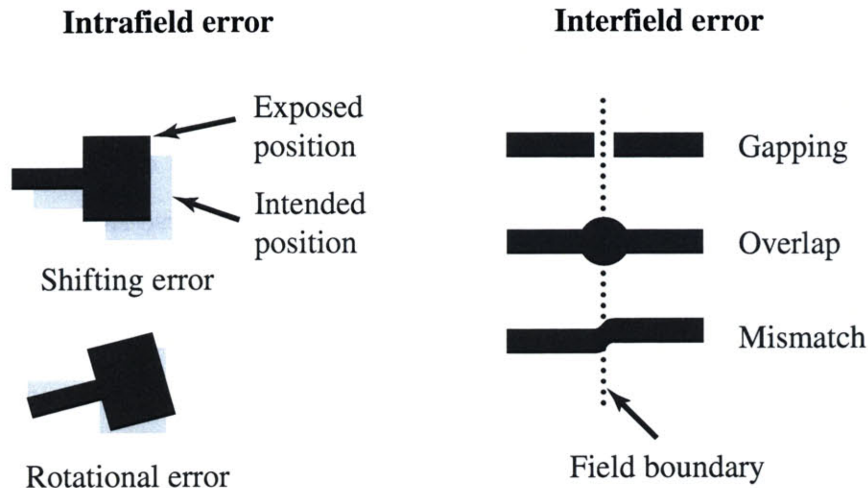

Figure 1-8: Placement errors can be categorized as intra-field distortion and inter-field distortion. Intra-field distortion can be a combination of shifting and rotational errors. Inter-field distortion can be gapping, overlapping or mismatch. Inter-field distortion is generally much worse than intra-field distortions.

of shifting and rotational errors assuming the magnification is perfect. Interfield distortion occurs at the field boundaries. It can be in any of the various forms of gapping, overlapping, or mismatch. Since the worst aberration generally happens at the field boundary, and low-frequency disturbances affect inter-field distortion the most, inter-field distortion is much worse than intra-field distortion.

1.2 Spatial-phase-locked Electron-beam Lithography

Spatial-phase-locked electron-beam lithography (SPLEBL) significantly improves the placement accuracy of EBL by providing direct referencing of the e-beam position. It relies on a global fiducial grid placed on the substrate to generate a reference signal. This reference signal is then used to detect the actual position of the beam, and any error is fed back to the deflection system for correction. In other words, the beam is "locked" onto the reference grid, and therefore the name SPLEBL.

There several different modes of SPLEBL [28, 27, 29, 26], depending on how the correction is calculated and when it is applied. The first two modes are termed the "look-then-write" mode, where the grid is scanned and the correction is calculated before exposure. In the segmented-grid mode, the grid exists only in non-patterned areas, preferably at the four corners of the field. In the sparse-sampling mode, the entire field is coarsely scanned at a sub-exposure dose. The third mode is termed the "look-while-write", or real-time mode, where the beam position is continuously monitored and corrected during exposure. This mode of SPLEBL provides the best placement result, and it will be the focus of this thesis.

SPLEBL has been developed for both Gaussian-beam systems and shaped-beam systems. This thesis focuses on the implementation of SPLEBL on Gaussian-beam systems for demonstration purposes, and the implementation on shaped-beam systems is described elsewhere [25]. Suitable strategies have not yet been developed for EPL systems.

Figure 1-9 depicts the schematics of SPLEBL for a Gaussian-beam system. It consists of three major components: reference-signal generation and detection, beam-position detection and correction, and partial-beam blanking.

The fiducial grid plays a key role in SPLEBL, and a unique set of requirements makes its fabrication process a challenging task. The grid and its fabrication process must not interfere with normal EBL exposures. The grid-fabrication process must be simple and "user-friendly". The grid should possess the highest signal-to-noise ratio (SNR) feasible to achieve maximum dynamic performance. Since the grid provides an absolute reference for the beam location, its long-range-spatial coherence determines the absolute-placement error of SPLEBL. Chapter 2 describes a user-friendly fabrication process for the fiducial grid, as well as the reference-signal generation process and the detector technology.

Beam position is detected by calculating the phase of the reference signal via a Fourier technique. By using such a technique, the SNR of the reference signal can be greatly improved, and requirements on the fiducial grid can be significantly relaxed. Phase detection of a sinusoidal signal with additive Gaussian white noise is well

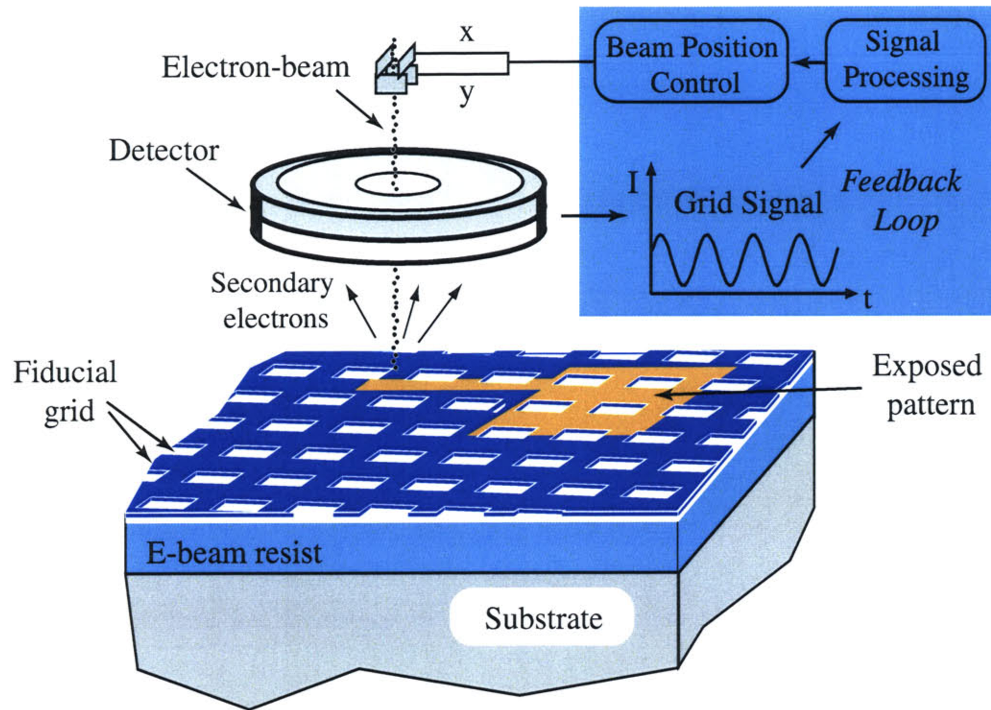

Figure 1-9: Spatial-phase-locked e-beam lithography relies on a reference signal for beam-position detection and error correction. The reference signal is generated during exposure by a fiducial grid placed on the sample. It is then processed in real time to extract beam-position errors, and the correction is fed back to the deflection system.

established [73]. The reference grid generates two distinctive frequencies to facilitate detection of the two coordinates (i.e., x and y) of the beam position. Chapter 3 provides details of the detection algorithm, and evaluates its performance.

The requirement of a partial-beam blanker is unique for Gaussian-beam systems. To achieve continuous referencing during exposure, the raster-scan exposure strategy is adopted, and the beam must be "partially on", e.g. 10% of the full-exposure dose, over "non-patterned areas". Hence, a dose modulation scheme is required. Dose modulation can be accomplished by varying either the dwell time of the beam at each pixel, or by varying the beam current. The first method is not very appealing because it requires an extremely fast, high-performance beam blanker. Chapter 4 demonstrates several partial-beam blanker designs that facilitate beam-current modulation in real time.

Chapter 2

Reference Signal & Fiducial Grid

In SPLEBL, the global-fiducial grid is used to generate a reference signal for beam-position detection. A unique set of requirements imposes some interesting engineering challenges on the fabrication process of the fiducial grid. To achieve direct referencing for maximum placement accuracy, the grid must be placed on the sample. The quality of the fiducial grid directly impacts the performance of the overall system. The grid must possess the highest SNR feasible to maximize the dynamic performance of the system. As an absolute global reference, the fiducial grid must possess long-range-spatial-phase coherence across the entire sample. The SNR of the reference signal determines the accuracy of the position-detection algorithm (discussed in the next chapter). On the other hand, random fluctuations and non-uniformities in the range of several grid periods are tolerable, because the detection algorithm typically conducts calculations over hundreds of periods, and any local random fluctuations can be averaged out. The fiducial grid and its fabrication should be non-perturbative to the standard EBL process, i.e., they should not adversely affect the exposure results. The fabrication process must be simple and "user-friendly" for general use. This chapter provides a detailed description on reference-signal generation/detection, and fiducial-grid fabrication.

2.1 Reference-signal Generation

When an e-beam enters a solid sample, the primary electrons undergo a series of collisions with surrounding atoms while losing their energy and being scattered off from their original paths. The collisions can be either elastic or inelastic, depending on whether energy exchange occurs. Most of the energy exchanged is converted to heat through phonon excitation, and the rest of the energy induces various types of emissions, such as secondary electrons (SE), back-scattered electrons (BSE), Auger electrons, X-rays, and other photons. Not all of these emissions are suitable for serving as the reference signal for SPLEBL. Some of them have very low SNR or spatial resolution, while others are not compatible with the EBL process.

2.1.1 Secondary Electrons

SE emission was first observed by Villard in 1899 [68]. When primary electrons undergo inelastic collisions with the surrounding atoms while travelling through a solid sample, part of the energy exchanged excites the outer-shell electrons of these atoms. These electrons will then diffuse in the solid as internal SE. After undergoing multiple inelastic scattering themselves and losing much energy, a small portion of the internal SE may escape from the sample surface into the vacuum. By convention, SE are defined as electrons emitted with energies less than 50 eV, and the majority of them have energy less than 10 eV. A typical energy spectrum of SE is plotted in Fig. 2-1 [59].

Because of their extremely low energies, only the internal SE that are very close to the sample surface can escape. The escape depth of SE is in general 2 to 20 nm for metals and 5 to 50 nm for insulators [71]. The small interaction volume provides SE signals a superior spatial resolution. The SE signal is used extensively in SEM imaging for its high generation efficiency and spatial resolution. Signal contrast in SE images is largely due to topography, difference in SE yields of sample materials, and sample charging.

The SE yield of a material is influenced by many factors such as the energy of the

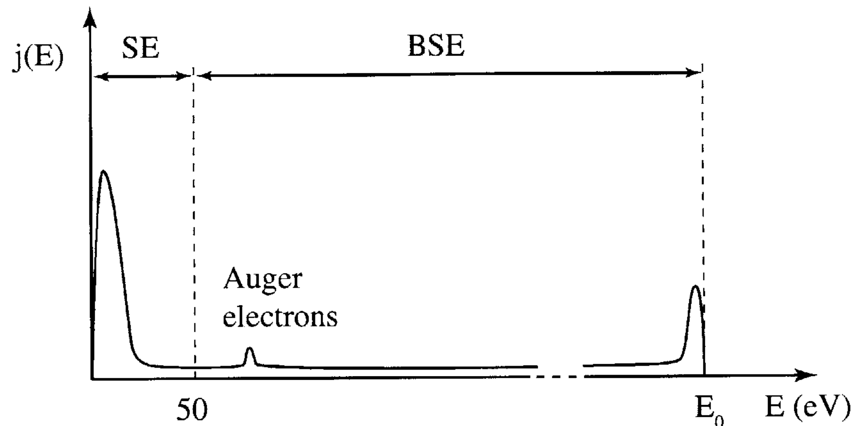

Figure 2-1: Energy distribution of electrons generated by primary electrons. Secondary electrons are defined as electrons that have energy less than 50 eV. Energy distribution of secondary electrons (after Goldstein et al. 1981).

primary beam, and surface conditions and physical properties of the material. Figure 2-2 plots a typical SE-yield curve as a function of the primary-beam energy. Surface

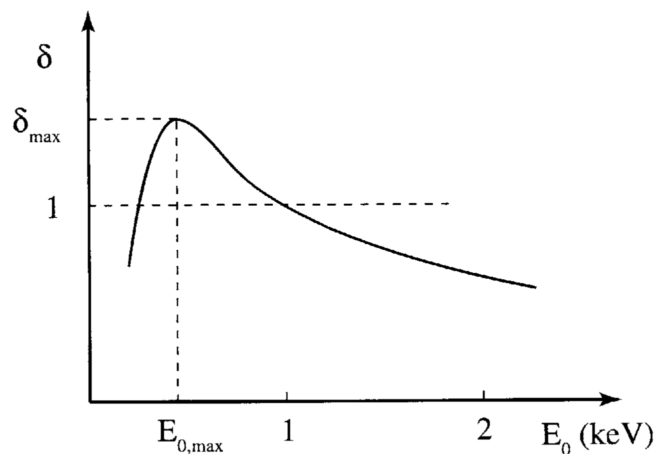

Figure 2-2: A curve of typical SE yield vs primary-beam energy. The SE yield increases with the primary-beam energy, reaches its peak at $E_{0,max}$, and then decreases. $E_{0,max}$ is several hundreds of electronvolts for most materials, especially metals.

conditions greatly affect the SE yield by altering the work function (for conductors) or the electron affinity (for insulators) of the sample. For example, a metal surface

covered by its native oxide or some kind of carbonaceous contaminates may have a higher work function than a clean one, resulting in a lower SE yield [34, 6]. Under modest chamber pressure, e.g. 10^{-6} Torr, contamination can build up on the sample during e-beam exposure. Physical properties of the material, e.g. single crystalline, polycrystalline or amorphous substrate, determines the escape depth of SE [45]. A properly prepared diamond film exhibits an exceptionally high SE yield [63], but graphite, another form of carbon, has an SE yield almost two orders of magnitude lower [17]. For insulators, part of the primary electrons will be trapped in the sample and induce charging, which will change the energy of the primary beam and cause the SE yield to vary over time.

The SE-emission process can be described by three stages: the excitation of the valence or conduction electrons, the diffusion of the excited electrons to the sample surface, and the escape of the electrons into the vacuum [62, 59]. (Other models can be found in references [59, 38].) Because of the complex nature of the process, theoretical formulations of the emission process were only modestly successful for so-called nearly-free-electron metals such as aluminum. The conduction electrons of these metals can be modelled as free-moving gas molecules [59]. Numerous numerical models based on Monte Carlo simulations were established for various materials and exposure conditions [15, 75, 58, 17], but the applicability of these models is always very limited.

Intensive experimental studies have been conducted on SE emissions of various materials, and enormous amount of data are available. Joy has compiled an exhaustive and comprehensive database including measurements from 1898 to 2001 [37]. The consistency of these data is, however, fairly poor due to variations in sample preparation and measurement conditions. In some cases the sample was placed in an ultra-high vacuum and its surface cleaned by ion bombardment to remove all contaminations, while in other cases the measurements were done in a normal SEM without any sample cleaning [36]. Although the first group of data is more repeatable and can be considered closer to the "true" values, the second group is more resemblant of the day-to-day situation and hence more useful for SPLEBL. Measurement data on

insulators diverge even more widely because of the different methods applied to deal with sample charging. The discrepancies between experimental results and calculations, from either theoretical or numerical models, can be as large as 20%, and the available data are at best a guideline.

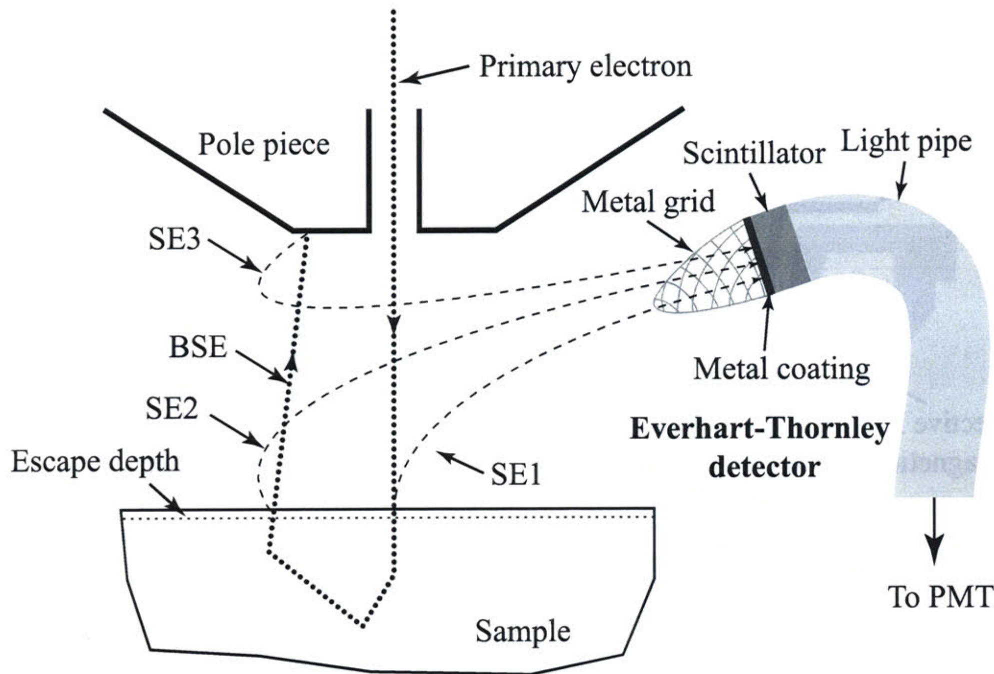

Figure 2-3: Secondary-electron generation. SE can be one of three types depending on their location of generation. SE1 are generated right around the primary beam. SE2 are generated by BSE that are further away from the primary beam. SE3 are generated by BSE at the polepiece or the chamber walls. The detector shown on the right is the Everhart-Thornley type. The metal grid is biased positively (e.g. +200 V) to attract SE. The metal coating on the scintillator is biased at several kilovolts to accelerate the SE so that they will strike the scintillator and generate many photons. The photons will be guided by the light pipe to a photo-multiplier tube (PMT) located outside of the vacuum chamber, where the optical signal is converted to an electrical signal and amplified.

As indicated in Fig. 2-3, SE can be classified as SE1, SE2 and SE3, depending on their origins of generation. SE1 are generated by the primary electrons and BSE produced in the vicinity of the beam. Because SE1 are localized within nanometers of the primary beam, they possess the highest spatial resolution. SE2 are generated

by BSE emerged further away from the primary beam, up to several microns for a 10 keV beam, so they do not carry much high-resolution information. SE3 are generated when BSE hit the chamber walls, or the pole piece of the column. Hence they do not contribute any spatial information, and are purely background noise. For most high-resolution applications, SE2 and SE3 are considered as part of the background noise.

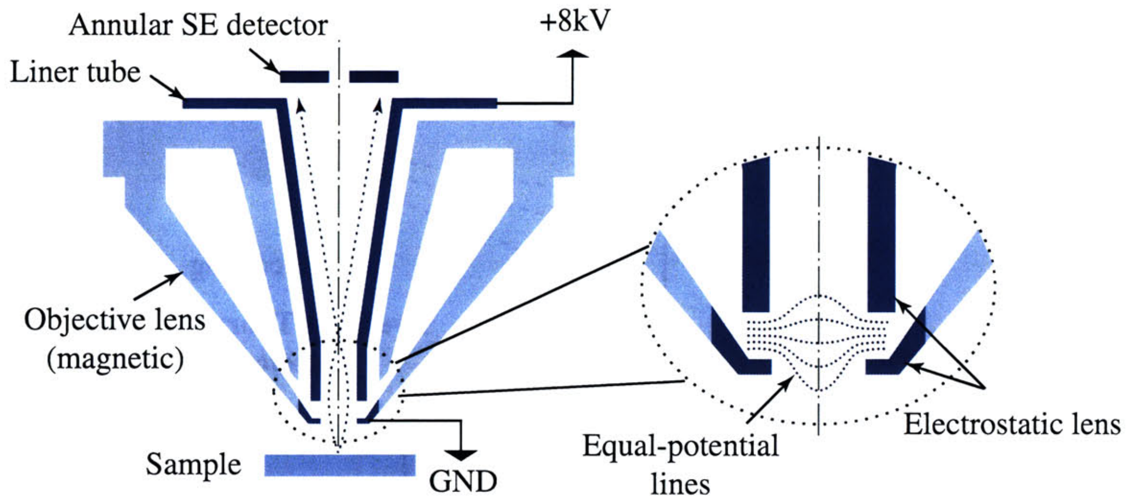

Figure 2-4: In-lens detector located above the objective lens. This configuration allows the detector to eliminate SE3 from SE1 and SE2, and hence decrease the background noise.

SE detectors have been well studied for decades. There are two different types. The Everhart-Thornley detector is depicted in Fig. 2-3. It consists of a metal grid, a scintillator and a photo-multiplier tube (PMT). The positively biased metal grid attracts SE towards the scintillator, and the photons generated by the scintillation process are detected and amplified by the PMT. The PMT signal can be further amplified and processed outside the vacuum. The Everhart-Thornley detector can not distinguish SE1, SE2 and SE3. Another type of detector, the in-lens detector, is shown in Fig. 2-4. The scintillator of this type of detector resides inside of the electron column, above the upper polepiece of the objective lens [41]. An electrostatic lens created between the liner tube and the pole piece of the objective lens attracts generated SE into the column and focuses them onto the scintillator. This config-

uration allows the detector to completely eliminate SE3 from SE1 and SE2, and to significantly decrease the background noise. The greatly increased SNR makes the in-lens detector an important component for the effectiveness of SPLEBL.

2.1.2 Scintillation Signal

Scintillation is a process in which photons are generated when a material is exposed to various radiations, including energetic electrons. The scintillating material, or scintillator, can be a gas, a liquid or a solid. As discussed previously, the scintillator plays an essential role in SE detection by converting the SE signal to an optical signal. A detector based on the combination of a scintillator and a PMT has a higher conversion efficiency, and much better reliability, than one that depends on an electron detector alone. The optical signal is more easily collected and manipulated than the SE signal. By choosing the appropriate material, a scintillation signal could potentially be used as the reference signal for SPLEBL.

Solid scintillators can be either organic or inorganic. Inorganic scintillators are usually made of alkali-halide crystals (e.g. NaI and CsI) or oxides (e.g. bismuth germinate). The electrons in the solid will be excited to higher energy levels when exposed to radiation, and when they de-excite to lower energy levels photons are emitted. Organic scintillators are composed of aromatic hydrocarbons, and the energy-absorption-release cycle happens at the molecular level.

Because the organic scintillators are composed of low-Z and low-density materials, and are not very efficient in absorbing the radiation energy, their conversion efficiency, especially for high-energy electrons, is much lower than that of inorganic counterparts. Organic scintillators can be quickly quenched under extensive radiation and lose their ability to emit light, while inorganic scintillators can last much longer. Organic scintillators have shorter decay constants than inorganic scintillators with the exception of BaF_2. The decay constants are typically $\sim$5 ns for organic scintillators and $\sim$100 ns for inorganic scintillators. The slow decay constants of inorganic scintillators make them unsuitable for high-speed applications.

2.1.3 Backscattered Electrons

When primary electrons interact directly with atomic nuclei, they experience large-angle scattering. Many of these electrons will reemerge from the surface of the sample and become BSE. Since little energy exchange occurs during large-angle scattering, many of the BSE possess energy close to that of the primary electrons (Fig. 2-1).

The BSE yield of a material is a function of the beam energy and the atomic number and density of the material. It is insensitive to sample-surface conditions due to the high energy of BSE. In commercial EBL systems, the beam energy is typically $\geq 10\,\text{keV}$, and the large escape depths of BSE in these systems can be up to tens of microns. Hence, the spatial resolution of BSE images is generally much worse than that of SE images. BSE signals are widely used in EBL systems for aligned exposures, because BSE can penetrate great depths to detect registration marks buried under the e-beam resist, and high-spatial resolution is not required in such applications. Solid-state detectors are usually used for signal detection.

To use BSE as the reference signal for SPLEBL, the grid must be made of relatively thick, high-Z materials to obtain a good signal contrast. Such a grid causes significant beam scattering, which makes it suitable only for the segmented-grid mode of SPLEBL [27]. The advantage of using a BSE grid is that it can be placed underneath the e-beam resist, and that makes the fabrication process much easier.

2.1.4 Characteristic X-rays & Auger Electrons

While travelling through the sample, primary electrons will occasionally ionize inner-shell electrons of the sample atoms. The ionized atoms are in a highly excited state, and will quickly relax back to a lower-energy state. During the relaxation process, electrons at the outer shells fall back to fill the inner shells, and the energies are released by either characteristic X-rays or Auger electrons. Since the yields of both the characteristic X-rays and the Auger electrons are several orders of magnitude lower than those of SE and BSE, they are not suitable as reference signals for SPLEBL.

2.1.5 Noise Analysis

The generation and detection of the reference signal can be characterized as a series of stochastic processes. Statistical noise generated in these processes will influence the accuracy of the beam-position-detection algorithm. The SNR of the overall system is usually limited by the so-called noise bottleneck, where the relative noise level is the highest. The SNR performance of the SE signal will be analyzed here as an example.

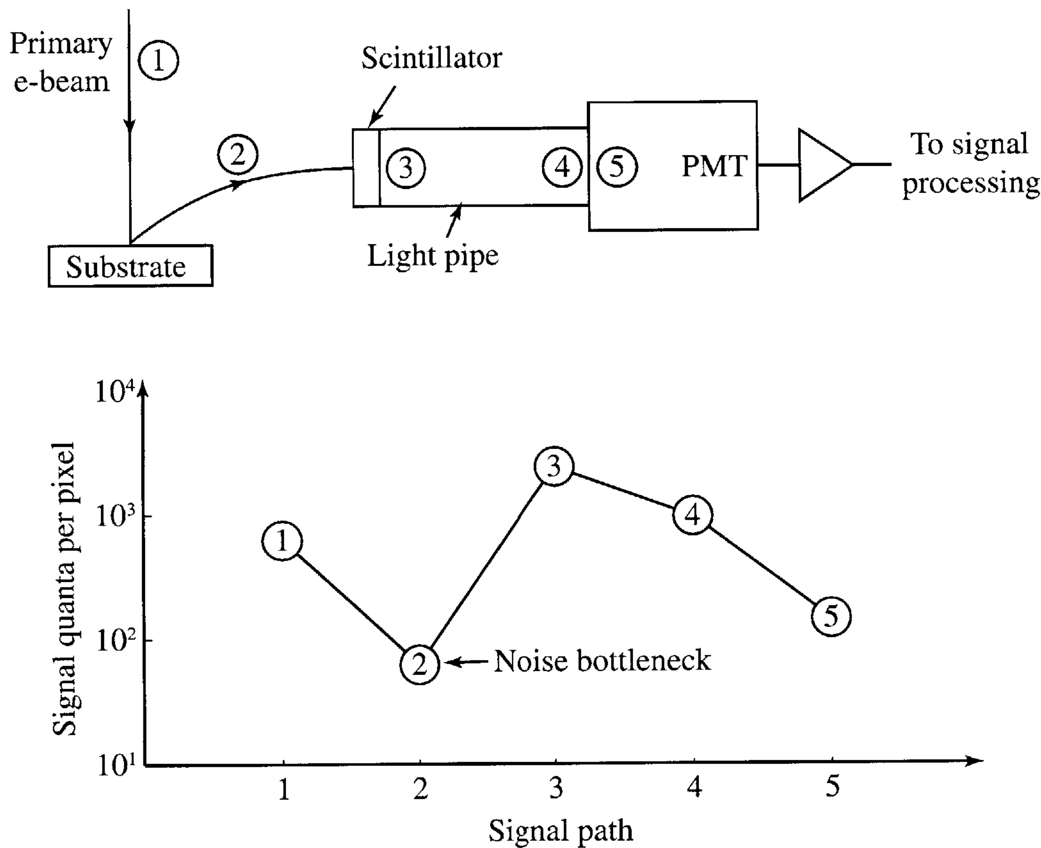

Figure 2-5: The signal path of SE in SPLEBL. The numbers ① to ⑤ indicates the five stages in the signal path: ① primary electron beam; ② SE generation and collection; ③ photon generation at the scintillator; ④ light guiding by the light pipe; ⑤ photoelectric conversion at the PMT. The lower figure plots the signal quanta generated at each stage. Please refer to Table 2.1 for the values in the plot.

Figure 2-5 depicts the signal path of the SE signal in SEM and SPLEBL, starting from the generation of the primary beam. The signal path consists of five stages labelled by numbers from ① to ⑤ in the figure, and each stage corresponds to a

stochastic process that follows the Poisson distribution. The values for the signal quanta at each stage are typical for an SEM converted system. The yield and signal quanta shown in the plot of Fig. 2-5 are given in Table 2.1

Stage		Yield	Signal quanta
①	Primary beam generation	–	625
②	SE generation	0.10	62
③	Scintillation @ 400 nm	52	3224
④	Light guiding	0.40	1290
⑤	Photoelectric conversion (PMT)	0.15	193

Table 2.1: Yields and signal quanta for the signal path of SE.

Stage ① provides the number of primary electrons deposited at each pixel that corresponds to a 10 nm step size and $100\mu\text{C/cm}^2$ exposure dose. The yield at Stage ② includes both the SE yield and the collection efficiency of the detector. Stage ③ assumes that the SE are accelerated to 8 kV prior to striking the scintillator, and 2% of that energy is converted to 400 nm (3.1 eV) photons. Some of the assumptions are adopted from reference [71].

Under most circumstances, each of the five stages can be modelled as a Poisson distribution, and the SNR of the rth stage, K_r, can be defined in terms of the mean of the signal quanta at that stage, n_r:

$$K_r = \frac{\bar{n}_r}{\sqrt{\bar{n}_r}} = \sqrt{\bar{n}_r}\ . \tag{2.1}$$

Since the stochastic processes associated with the five stages are independent of one another, K_r can be expressed as:

$$\frac{1}{K_r^2} = \frac{1}{\bar{n}_1} + \frac{1}{\bar{n}_2} + \frac{1}{\bar{n}_3} + \cdots + \frac{1}{\bar{n}_r}. \tag{2.2}$$

It is clear from the above equation that the SNR of the reference signal is dominated by the process whose signal quanta is the smallest. Hence, the corresponding stage is the noise bottleneck of the reference-signal-generation system. In the cases of the SE

signal, the BSE signal, and the scintillation signal, the noise bottleneck is between the substrate and the collector, i.e. Stage ②.

When conducting SEM imaging, the SNR can be significantly improved by taking multiple scans and averaging over the same sample area. A larger number of scans gives higher SNR and higher quality images. This method increases the number of primary electrons deposited at each pixel, $\bar{n}_1$, and the signal quanta in the following stages increase accordingly. In an EBL process, on the other hand, the number of primary electrons per pixel is determined by the exposure dose and the step size. Hence, the only way to improve the SNR is to improve the yield and the collection efficiency at Stage ②.

2.2 Lithographic Techniques

The lithographic technique used to pattern the grid defines both the resolution and the long-range-spatial-phase coherence of the grid. Lithographic techniques suitable for patterning periodic gratings or grids over large areas are based on either interference lithography (IL) or nanoimprint lithography (NIL). For simplicity and practical issues, the period of the fiducial grid is set to 250 nm. The optimal lithographic technique used in producing the grid is highly dependent on the grid material and the substrate.

2.2.1 Conventional Interference Lithography

Interference lithography (IL) is the preferred method of producing periodic gratings over large areas. The exposable area is dependent mainly on the experimental setup. As depicted in Fig. 2-6, IL uses two interfering light beams to form a lateral standing wave, or interference fringes, at the substrate, and the standing wave is recorded in the photoresist. The grating period of the standing wave, Λ_G, is determined by

$$\Lambda_G = \frac{\lambda}{2\sin\theta}, \tag{2.3}$$

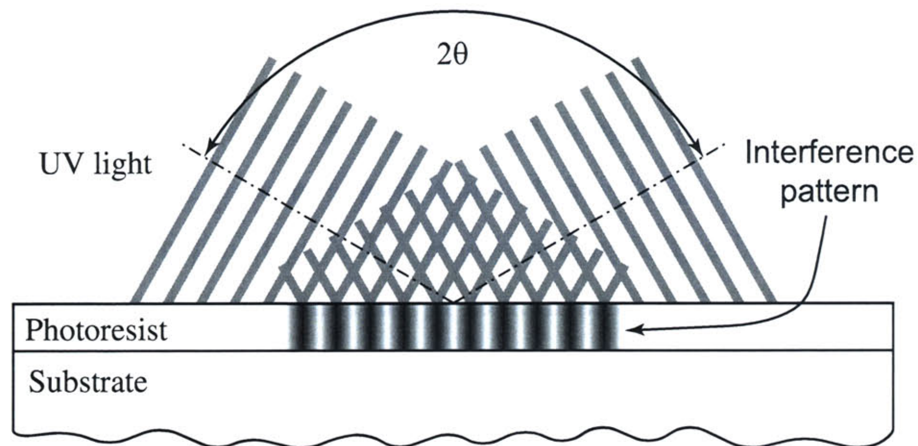

Figure 2-6: Interference lithography. The photoresist on the substrate records the interference pattern formed by the two light beams.

where λ is the wavelength of the light, and θ is the half angle between the two light beams.

Figure 2-7 illustrates the "conventional" IL setup (the Mach-Zehnder configuration) at MIT [69]. The source is an Ar-ion laser with $\lambda = 351.1\,\text{nm}$. The laser beam is split into two and then recombined by the mirrors to form the standing wave at the substrate. Because it is extremely difficult to obtain perfect plane waves due to limitations in the optical components, two high-quality spherical beams are used instead. The spherical beam is created by using a spatial filter, which consists of a lens and a pinhole. The lens focuses the laser beam to a fine spot at the pinhole, causing a high-quality spherical wave to emerge from the other side of the pinhole. Portions of the two beams passing by the substrate are split by the lower beamsplitter. Each pair of the split beams interfere at one of the two photodiodes. A phase-error sensor compares the outputs of the photodiodes and provides an indirect reference to the locations of the interference fringes. Any movement of the fringes during IL exposure will cause the phase-error sensor to send a correction signal to the Pockels cell. The Pockels cell will then shift the phase of one of the laser beams, causing the fringes to move back to their original locations. A variable attenuator is used to balance the intensities of the two beams. The current system is capable of producing high-quality gratings and grids up to 10 cm in diameter at spatial periods down to 200 nm.

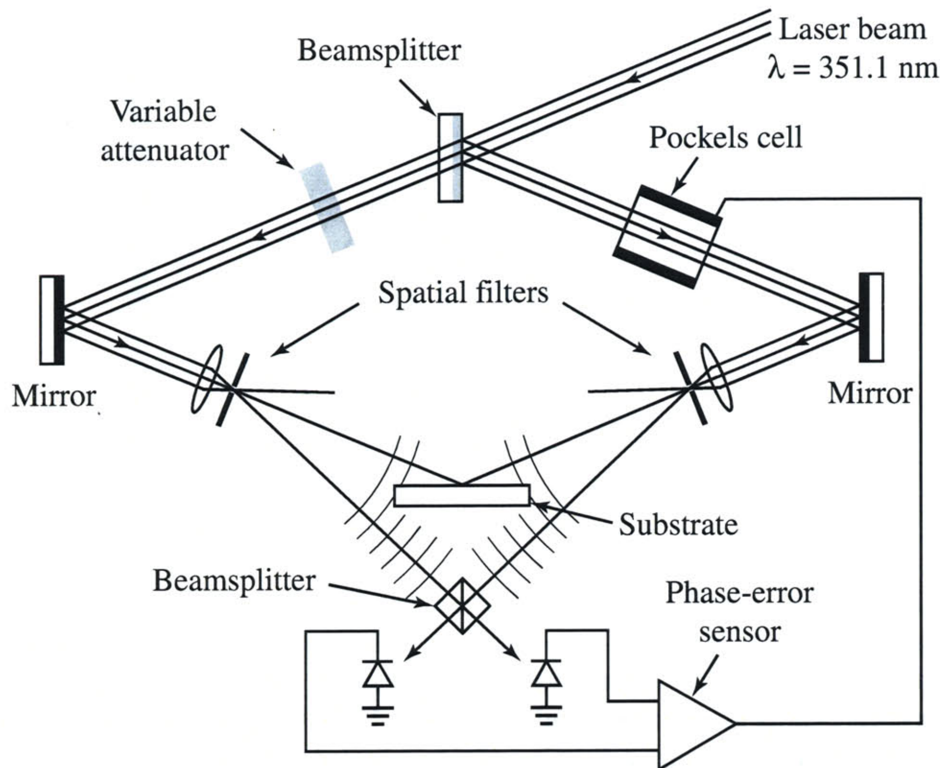

Figure 2-7: Conventional interference lithography setup at MIT. The wavelength of the laser beam is 351.1 nm. The entire system occupies a 2 m× 3 m optical bench. The phase-error sensor and the Pockels cell form a feedback control that stabilizes the standing wave from environmental disturbances during IL exposure.

Setting up the conventional IL system to obtain various grating periods is a very tedious and time-consuming task. Alignment between the beams and the substrate must be very precise to ensure uniform exposure. The Lloyd's mirror configuration shown in Fig. 2-8 provides a much simpler alternative for producing gratings over a smaller area [69]. A HeCd laser beam ($\lambda = 325\,\text{nm}$) is expanded to a spherical wave by a spatial filter (not shown in the figure). The distance between the spatial filter and the sample holder is 2 m. When the beam reaches the sample holder, a mirror reflects half of the beam, causing it to interfere with the other half at the substrate. The angle between the mirror and the substrate is fixed at 90°. No feedback control is required to lock the interference fringes because of the rigid connection between the mirror and the substrate. The period of the exposed grating can be changed by

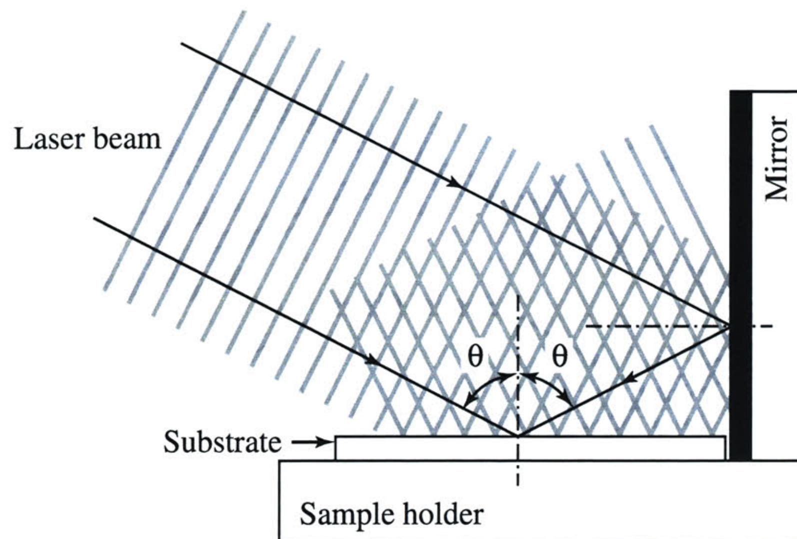

Figure 2-8: Lloyd's mirror configuration for IL. A portion of a single spherical beam is folded onto itself by the mirror to form interference fringes. When the mirror and the substrate is fixed to 90°, the interference beams are automatically aligned. Different grating periods can be obtained by simply adjusting the incidental angle of the laser beam to the sample holder, θ.

rotating the sample holder so that the incident angle of the beam to the substrate, θ, is set to the desired value according to (2.3). The size of the exposable area is dependent on the uniformity of the beam wavefront, the incidental angle θ, and the coherence length of the source. The wavefront is largely affected by the quality of the spatial filter (e.g. the quality of the lens and the size of the pinhole) and air turbulence in the environment. Most of the IL exposure results shown in this thesis were conducted on the Lloyd's mirror setup. The Lloyd's mirror setup does not provide as high a quality grating as does the Mark-Zehnder configuration.

Both configurations discussed above use spherical beams, which are known to introduce hyperbolic phase progression [18, 19]. The phase deviation from linear can be reduced, but not eliminated, by keeping large distances between the spatial filters and the substrate, or by substrate curvature [70, 69]. The distance between the spatial filters and the substrate in the Mach-Zehnder configuration is $\sim$1 m, and that in the Lloyd's mirror configuration is $\sim$2 m. The phase progression for the Mach-

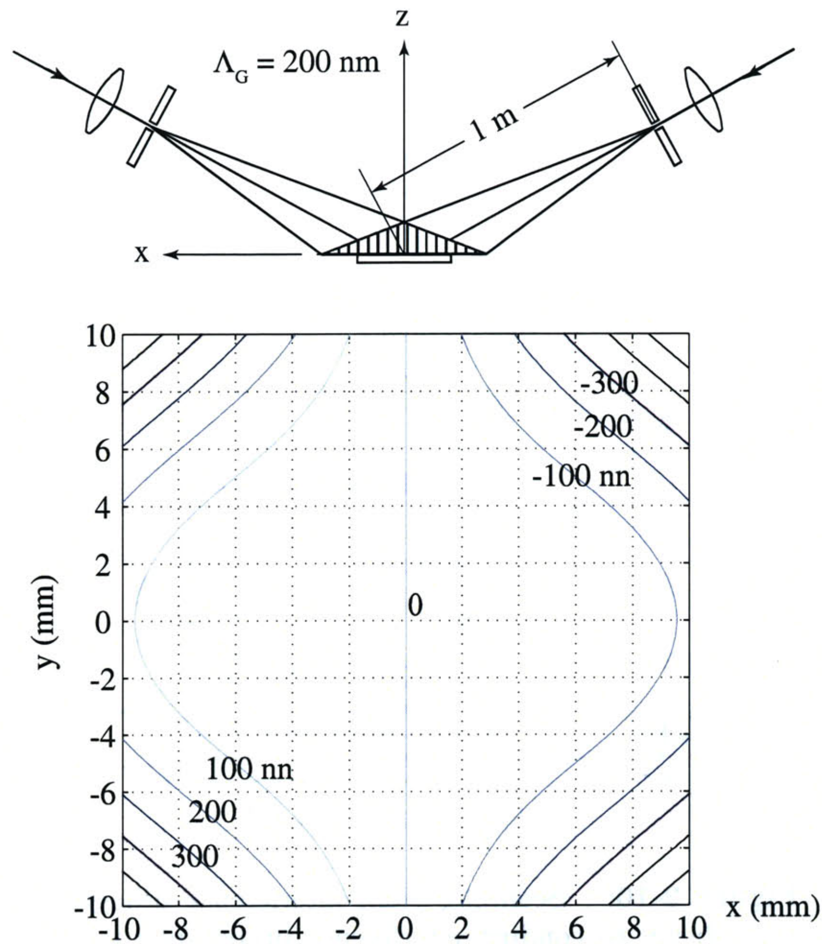

Figure 2-9: The lower plot shows the spatial-phase deviation from a linear phase of a 200 nm period grating over a 10 mm× 10 mm area on the MIT Mark-Zehnder IL system shown in the upper figure.

Zehnder configuration was studied carefully by Ferrera, and the result for a 200 nm period grating over a 10 mm× 10 mm area is plotted in Fig. 2-9. Although the phase deviation can be measured after the pattern has been developed, it is impractical to conduct such measurement for every substrate.

2.2.2 Scanning-beam Interference Lithography

A new and unique technology, Scanning-beam Interference Lithography (SBIL), was developed by Schattenburg et al. at MIT to eliminate the hyperbolic phase progression that troubles conventional IL systems [42, 10, 11]. As shown in Fig. 2-10, SBIL

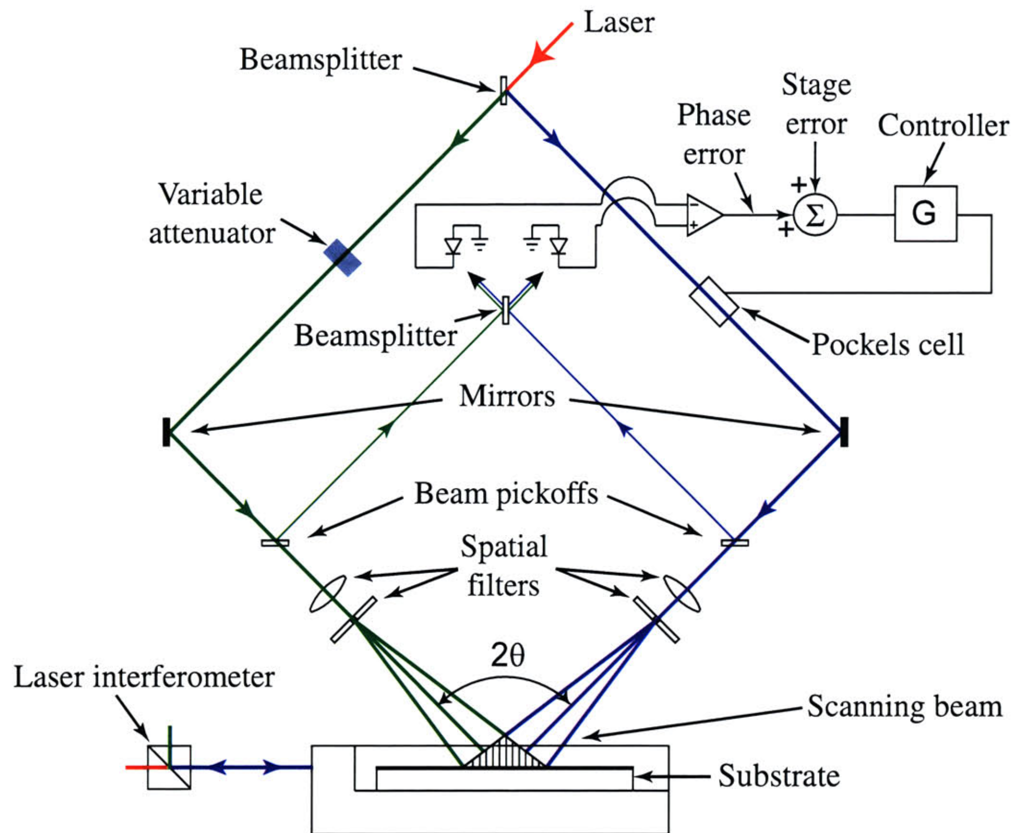

Figure 2-10: Scanning-beam interference lithography uses a very small beam to conduct interference lithography to avoid hyperbolic-phase progression. The setup is very similar to that of the Mach-Zehnder configuration. The beam pickoffs take portions of the beam for fringe locking. The feedback controller corrects for both stage errors and fringe shifts.

closely resembles the Mach-Zehnder configuration. The major difference is that SBIL uses a very small interfering beam, typically between 200 μm and 2 mm in diameter, to conduct exposure. The phase distortion over such a small area is essentially negligible. Large-area gratings are printed in a step-and-scan fashion as illustrated in Fig. 2-11. A laser-interferometer-controlled stage moves the substrate back and forth while ensuring its precise placement. The two beam pickoffs are essentially two beamsplitters that pick up portions of the two beams for fringe locking. A feedback controller provides both stage-error correction and fringe locking during exposure. The exposable area is limited only by the travelling range of the stage. A 400 nm

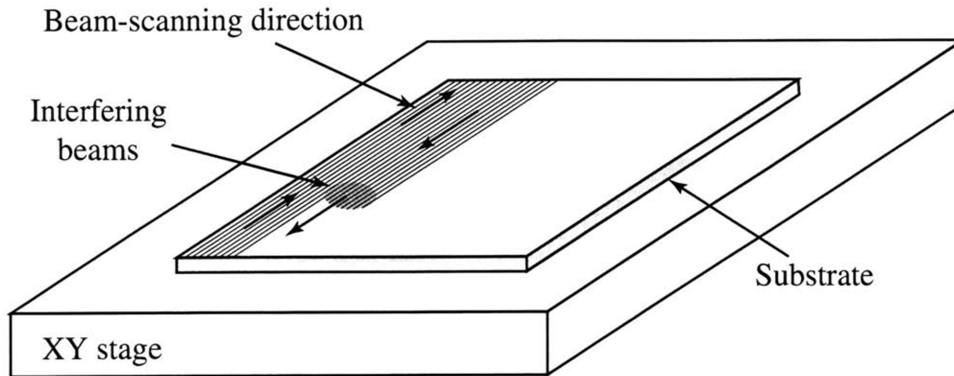

Figure 2-11: Step-and-scan exposure strategy used by SBIL. A laser-interferometer-controlled stage is used to precisely move the substrate back and forth under the small beam for producing gratings over large areas. The scan direction can also be perpendicular to that shown in the drawing.

period gratings over a 300 mm diameter substrate, with 2 nm 3σ phase repeatability has been demonstrated. With further improvements, 1-nm-level absolute-placement accuracy should be achievable.

Using SBIL to expose the fiducial grid for every substrate is not considered practical because the SBIL system is very expensive and the exposure is somewhat time-consuming. Hence, it is more feasible to use SBIL to produce a mask or template, and to replicate the fiducial grid from the mask or template onto the substrate. Several lithographic techniques based on masks/templates will be introduced in the rest of this section.

2.2.3 Near-field Interference Lithography

Near-field Interference Lithography (NFIL) is a variation of IL that uses masks [69]. Figure 2-12 describes the principles of NFIL. When a normal-incident laser-beam passes through a grating mask of appropriate spatial period, it diffracts into many different orders. By carefully choosing the wavelength of the source and the grating period, all diffracted beams with orders higher than unity can be suppressed. The ±1 order beams will interfere at the substrate to form a standing wave with a period

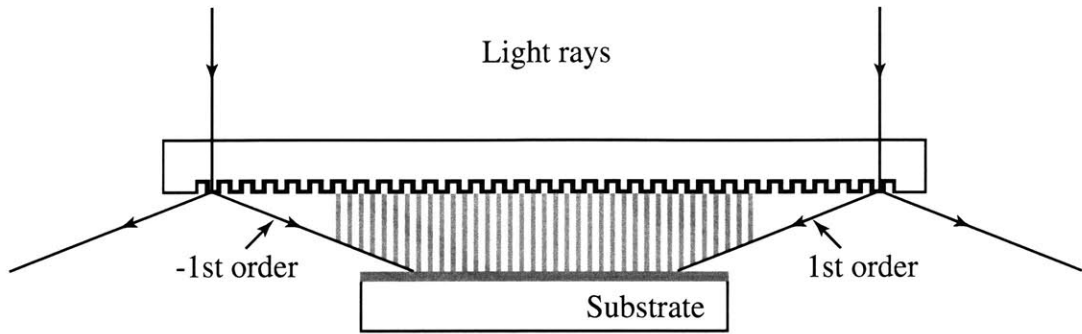

Figure 2-12: Near-field interference lithography. The beam enters the mask grating and diffracts into ± 1 order beams. These two beams form interference fringes at the substrate. The grating teeth cause a π-phase shift to the light so that the zeroth order beam is suppressed. The period of the grating is set such that the higher-order beams are reflected back by the mask.

that is half that of the master-grating. With a phase grating, the strength of the zeroth order beam can be reduced to near zero by adjusting the height of the grating teeth. Suppose that the wavelength of the light source is λ, and the period of the mask grating is Λ, the diffraction angle of the first-order beams, θ, is given by

$$\theta = \arcsin\left(\frac{\lambda}{\Lambda}\right) \, , \tag{2.4}$$

and the period of the standing wave Λ_{G} at the substrate is

$$\Lambda_{\mathrm{G}} = \frac{\lambda}{2 \sin\theta} = \frac{\Lambda}{2} \, . \tag{2.5}$$

If the limited spatial-coherence range of the source is limited, the contrast of the interference pattern will decrease when moving away from the mask. Hence, to transfer the interference pattern into the photoresist, the substrate should be placed very close to the mask, usually from several microns up to tens of microns. A laser source is much better than a regular UV lamp, because it has a much better spatial-coherence. Temporal coherence is not much of a concern for this system. Semiconductor lasers are ideal for this application because of their compact physical sizes and low cost, and they are available at various wavelengths. With $\lambda = 400\,\mathrm{nm}$ and $\Lambda = 500\,\mathrm{nm}$, the

diffraction angle of the first-order beams is 53.13°, and the exposed grating period is $\Lambda_G = 250\,\text{nm}$. The second-order beams will not propagate to the substrate, because their diffraction angle is greater than 90°.

The requirement on gapping control between the mask and the substrate is fairly relaxed. The error in the exposed grating period, $\Delta\Lambda_G$, due to gapping non-uniformity is given by

$$\Delta\Lambda_G = \frac{\Delta h^2}{L}\ , \tag{2.6}$$

where Δh is the difference in gapping between two points on the substrate, and L is the distance between the two points. For a 150 mm substrate, a 1 μm gapping difference on the edges corresponds to a mere 6.56 pm in the grating period. A big variable is the zeroth order beam. The zeroth order beam, if not completely suppressed, can interfere with the first order beams, and cause intensity variations along the vertical direction, which makes the exposure very sensitive to gapping uniformity between the mask and the substrate.

The laser beam is usually very small in diameter. Large substrates can be exposed by either expending the laser beam, or scanning the small beam over the mask. For the second option, multiple sources may be used to reduce the exposure time. The mask should be larger than the substrate to ensure full coverage. A thick quartz wafer should be used as the mask material to minimize distortions in the master grating. Particle control could be an issue because of the small gaps between the mask and the substrate.

With a grating mask, two perpendicular exposures are required to produce a grid pattern, and accurate rotational alignment between the two exposures is a challenging task, especially for large substrates. To ensure 1 nm-relative-placement accuracy between the center and the edge of a 150 mm substrate, the rotational misalignment can be no larger than 1.33×10^{-8} rad. To avoid this difficulty, a grid mask, generated, for example, on the SBIL system, can be used instead of the grating mask.

2.2.4 Achromatic Interference Lithography

Achromatic Interference Lithography (AIL) is another form of a mask-based IL system [61, 60]. Figure 2-13 depicts AIL. In this configuration, the light beam is diffracted

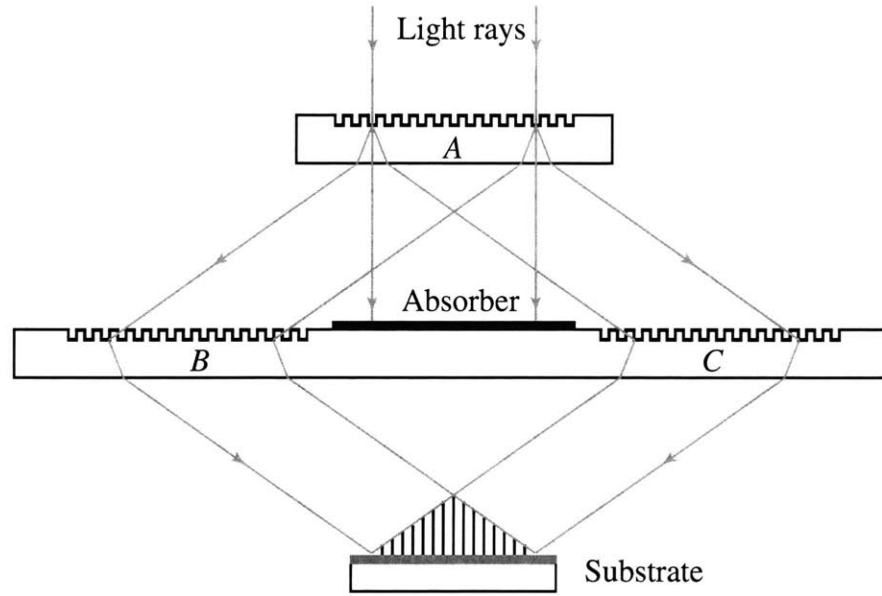

Figure 2-13: Achromatic interference lithography. The 0th order beam is blocked by the absorber. The gratings B and C diffract the ± 1 order beams, and two of the resulting diffracted beams interfere at the substrate.

by the grating mask A. The ± 1 order beams are then recombined by gratings B and C, while the zeroth-order beam is blocked by the absorber. All higher-order beams can be eliminated by choosing appropriate source wavelength and grating period as described previously. The gap between the masks and the substrate is substantially greater than that in NFIL, and particles become a much smaller problem. This scheme also completely prevents the zeroth order from reaching the substrate.

Figure 2-14 shows the top view of the masks used for AIL. There are two issues associated with AIL. Firstly, the area of grid A must be large enough to cover the entire substrate, and that of the second set of gratings, which includes B, B', C and C', must be at least nine times greater. To produce such a large mask would be very costly. If B, B', C and C' are made on separate mask plates, aligning them for a

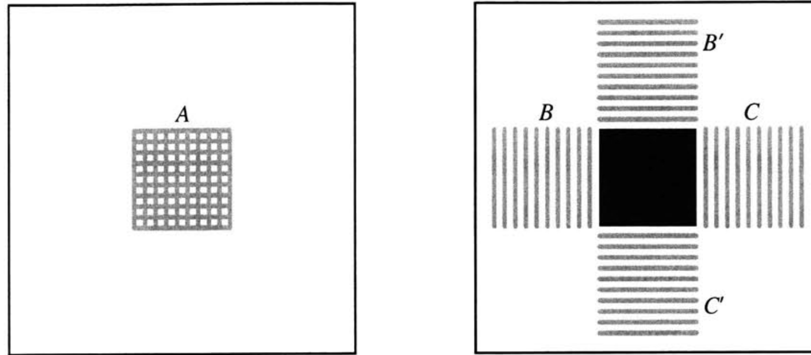

Figure 2-14: Mask design for AIL. The area of grid A must be large enough to cover the entire substrate, and that of the second mask will be nine times larger.

proper exposure could be a daunting task for the end users. Secondly, the gap between the two masks, and the lower mask and the substrate, is given by $L \cdot \cos\theta$, where L is the length of the substrate and θ is the diffraction angle. This large distance makes gapping control difficult and expensive.

2.2.5 Nanoimprint Stamping

Nanoimprint lithography (NIL) and microcontact printing (μCP) are two lithographic techniques that use templates. NIL conducts lithography in two steps [12]. In the first step, a topographically-patterned hard template, or mold, usually made of Si or SiO_2, is pressed into a thin polymer resist covering the substrate. After the mold is released, relief structures are created in the resist. In the second step, residual resist in the compressed area is removed by anisotropic reactive-ion etching. The operating conditions, e.g. temperature and pressure, are dependent on the resist used, and some implementations, such as the Step-and-Flash imprint lithography (S-FIL) [13], require neither elevated temperature nor high pressure. The hard mold of NIL ensures minimum distortion in the printed features, but the required etching step is not compatible with the standard EBL process, because the UV light generated by the plasma during etching will expose most types of e-beam resists.

In contrast, μCP uses a soft mold, typically made of poly(dimethylsiloxane)

(PDMS) elastomers [72, 74], and a pattern medium, or the "ink", is applied onto the mold. When the mold is brought into contact with the substrate, the ink is transferred onto the substrate by the difference in interfacial energies between the ink, the substrate, and the mold. The ink is typically made of self-assembled monolayers (SAM) and is extremely thin. Because a substrate is never perfectly flat, the soft mold ensures intimate contact with the substrate. The interfacial energy between the ink and the substrate must be much greater than that between the ink and the mold for complete pattern transfer. In this process, no etch back is required after pattern transfer. Pattern placement for this technique, however, is very poor because the mold is soft and can be easily distorted.

Figure 2-15 illustrates a method of combining NIL and μCP for pattern transfer, which we named Nanoimprint Stamping (NIS). An NIS mold consists of a rigid body and a soft layer. Patterns are encoded in the soft layer. The pattern-transfer process is the same as that of μCP. The ink is first coated over the mold, and the mold is then pressed against the substrate. The rigid body minimizes distortions in the mold, and the soft layer ensures intimate contact with the substrate.

Lateral distortions in the soft layer under pressure will be directly transferred into the grid. The severity of the distortion is dependent on the ratio between the soft-layer thickness and the grid period. If the distortions are localized within a small number of periods and are randomly distributed, they will have little effect on the placement accuracy of SPLEBL, because the detection algorithm, introduced in the next chapter, averages over hundreds of periods to calculate the beam position, and random errors will be averaged out.

The greatest challenge of NIS is to identify the appropriate ink material that can be easily coated on the mold, and transferred to the substrate. If the ink will be used as part of the grid, it has to be kept very thin, $< 50\,\mathrm{nm}$ for organic materials and $< 10\,\mathrm{nm}$ for metals. Another possibility is to pattern the substrate with a SAM, and then coat the substrate with a material that only sticks to SAM-covered areas. The mold usually has a limited lifetime. They can, however, be easily replicated from a master template. Particles will not be a major issue because NIS, like S-FIL [2], is a

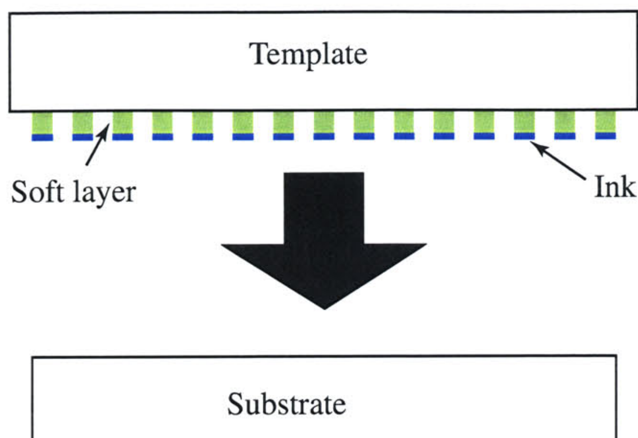

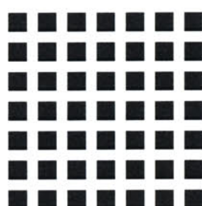

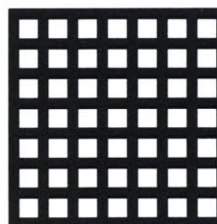

Figure 2-15: Nanoimprint stamping (NIS), a lithographic technique that combines NIL and μCP. The mold consists of a rigid body and a soft layer. The soft layer carries the grid pattern. The rigid body minimizes the distortion during pattern transfer, and the soft layer ensures intimate contact between the mold and the substrate. The grid pattern can be either "positive" or "negative" as shown on the bottom. The dark area represents the protruding part of the mold. The positive mold will have greater random distortions, while the negative mold will have more systematic distortions.

self-cleaning process. The excessive ink left on the mold after each stamping can be cleaned with an appropriate solvent.

2.3 Secondary-electron Grid

Besides the lithographic technique, the choice of grid materials and post-exposure processes are equally important to the success of the fiducial grid. SE was chosen to

serve as the reference signal for its high spatial resolution, high conversion efficiency, and efficient detector. Because an SE grid can be made very thin, it is the least disturbing one to EBL processes. The SE grid must be placed on top of the e-beam resist due to the short escape depth of SE, and thus complicates the fabrication process. Many standard processes such as reactive-ion etching, sputtering, or those requiring elevated temperatures can not be used in fabricating the grid on the e-beam resist as they may alter the resist properties.

The contrast of the reference signal is created by the difference in SE yields of two materials, e.g., the grid material and the material on which it sits, as illustrated in Fig. 2-16(a). In this figure, δ_h and δ_l represent high-SE-yield and low-SE-yield materials,

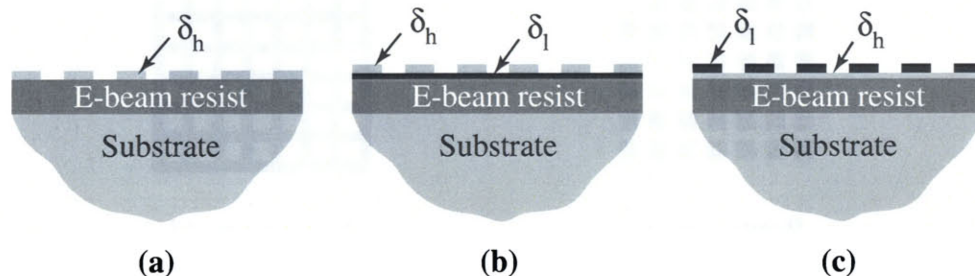

Figure 2-16: Resist stack for SPLEBL. δ_h stands for high SE-yield material, and δ_l stands for low SE-yield material. **(a)** Grid placed directly on resist. **(b)** δ_h grid placed on δ_l layer. **(c)** δ_l grid placed on δ_h layer.

respectively. Although this "ideal" stack seems very attractive for its simplicity, it may not be practical for various reasons. For example, the δ_h material may be difficult to pattern. The SE yield of the e-beam resist may be comparable to that of the grid material, making the signal contrast very low. Furthermore, most e-beam resists are insulating polymers whose SE yields will change during exposure. This will make the signal contrast sensitive to the beam position, and will reduce the accuracy of the detection algorithm. In such circumstances stacks shown in Fig. 2-16(b) and (c) appear more attractive. In certain cases where the grid material is incompatible with the e-beam resist, additional layers can be added to separate the grid material from the e-beam resist.

Although, as mentioned above, the grid period is chosen to be 250 nm for convenience, it should not be set too far off. A much larger period will reduce the accuracy of the detection algorithm, and a much smaller period will complicate the fabrication and cause phase-wrapping errors. The thickness of the grid should not exceed the escape depth.

2.3.1 Grid Material

Ideally, a material with the highest SE yield should be used as δ_h. It is, however, not always possible. For example, diamond has an exceptionally high SE yield, but the extreme conditions required for its growth rule it out. Low-atomic-number metals are good candidates because they have relatively high SE yields and can be easily prepared by evaporation. Furthermore, using metal can prevent sample charging and provide stable SE generation. In fact, it is a common practice in SEBL to evaporate a few nanometers of aluminum on top of the e-beam resist to prevent charging. High-atomic-number metals should not be used because they cause significant forward scattering of the e-beam, and adversely affect the exposure result. Insulators such as SiO_2 or polymers are suitable as δ_l for their low SE yields.

Three metals, aluminum (Al), chromium (Cr) and copper (Cu), have been actively pursued as the δ_h material. The SE yield of a bulk material usually differs from that of the corresponding thin film, because SE yield is very sensitive to the backscattered-electron (BSE) yield of the material [71]. For thin films used in this investigation, the BSE yield is simply that of the substrate. The SE yields of 7 nm Al, Cr and Cu films were measured, and the results were the same within the measurement accuracy of the equipment. Cu was eventually chosen as the grid material for its low stress and easy processibility. Evaporated Cr films are generally under high compressive stress, and can cause the e-beam resist to buckle. Al is too reactive with both acidic and basic solutions, and hence incompatible with many processes such as wet etching and photoresist-development.

Several other materials including single-wall carbon nanotubes (SWCNT) and fullerenes (C_{60}) were also under investigation for their high SE yields. Figure 2-17

shows a 70 nm thick evaporated C_{60} films on a Si substrate. The SE yield of a C_{60} film

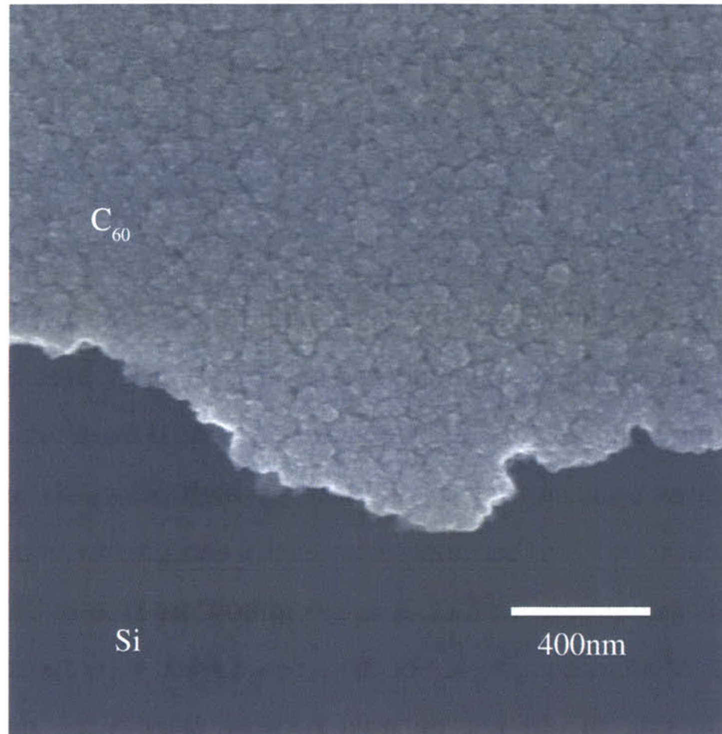

Figure 2-17: Evaporated C_{60} film on Si substrate. The film is 70 nm in thickness. The measured SE yield is twice that of the Cu film.

increases with the film thickness, and reaches its maximum at around 70 nm. The SE yield of the 70 nm C_{60} film is more than twice that of the 7 nm Cu film. SWCNT show even higher SE yield, but it is difficult to form uniform thin films with them because they tend to bundle together. Attempts have been made to mix SWCNT with various polymers for spin-coating, but it only worked well when the concentration of SWCNT is very low. These new materials have not yet been used for making the grid.

Signal contrast can also be improved by identifying materials with extremely low SE yields to serve as the δ_l material. Tetracyanoquinodimethane (TCNQ), a conducting polymer, and its potassium salt (KTCNQ) may serve this role well as both of them have very low SE yields comparing with other materials [37]. TCNQ can be prepared either by evaporation [53, 40] or by spin-coating [35].

2.3.2 Al Grid

Al was first evaluated as the grid material because of its low atomic number, low density, and easy deposition. In standard EBL processes, a thin film of Al is often applied on the substrate to avoid charging, and a high-energy e-beam can penetrate it with little scattering. With a native oxide layer, Al is very stable under normal conditions, which makes its handling extremely easy. However, Al is reactive with both acidic and basic solutions. This poses a major problem for the grid fabrication because most developers of the i-line photoresists used for IL exposure are strong basic solutions. NIS may help to solve the problem once an appropriate ink can be identified.

Liftoff

To avoid direct contact with basic solutions, a process based on liftoff was developed for an Al grid. Figure 2-18 shows the process flow. The e-beam resist is poly(methyl-methacrylate) (PMMA), a common high-resolution positive resist. A successful liftoff process depends on a resist profile with straight or undercut sidewalls. An anti-reflection-coating (ARC) layer is necessary to eliminate vertical standing waves during IL exposure and to obtain a good resist profile. However, removing ARC usually involves using strong oxidants at elevated temperatures, which will inevitably affect the e-beam resist. Hence, the ARC layer is placed beneath the e-beam resist. The evaporated SiO is to prevent intermixing between the photoresist and the e-beam resist. Adhesion between SiO and the photoresist is a common problem in photolithography, and it can be easily solved by applying a layer of adhesion promoter, such as Hexamethyldisilizane (HMDS). The IL exposure is conducted on the Lloyd's mirror setup introduced previously. Figure 2-19 shows an SEM image of a 250-nm-period Al grid.

This process worked quite well, and it provided all sample substrates that were used for early real-time SPLEBL experiments described in the next chapter. It involves three spin-coatings and two evaporations. After e-beam exposure and devel-

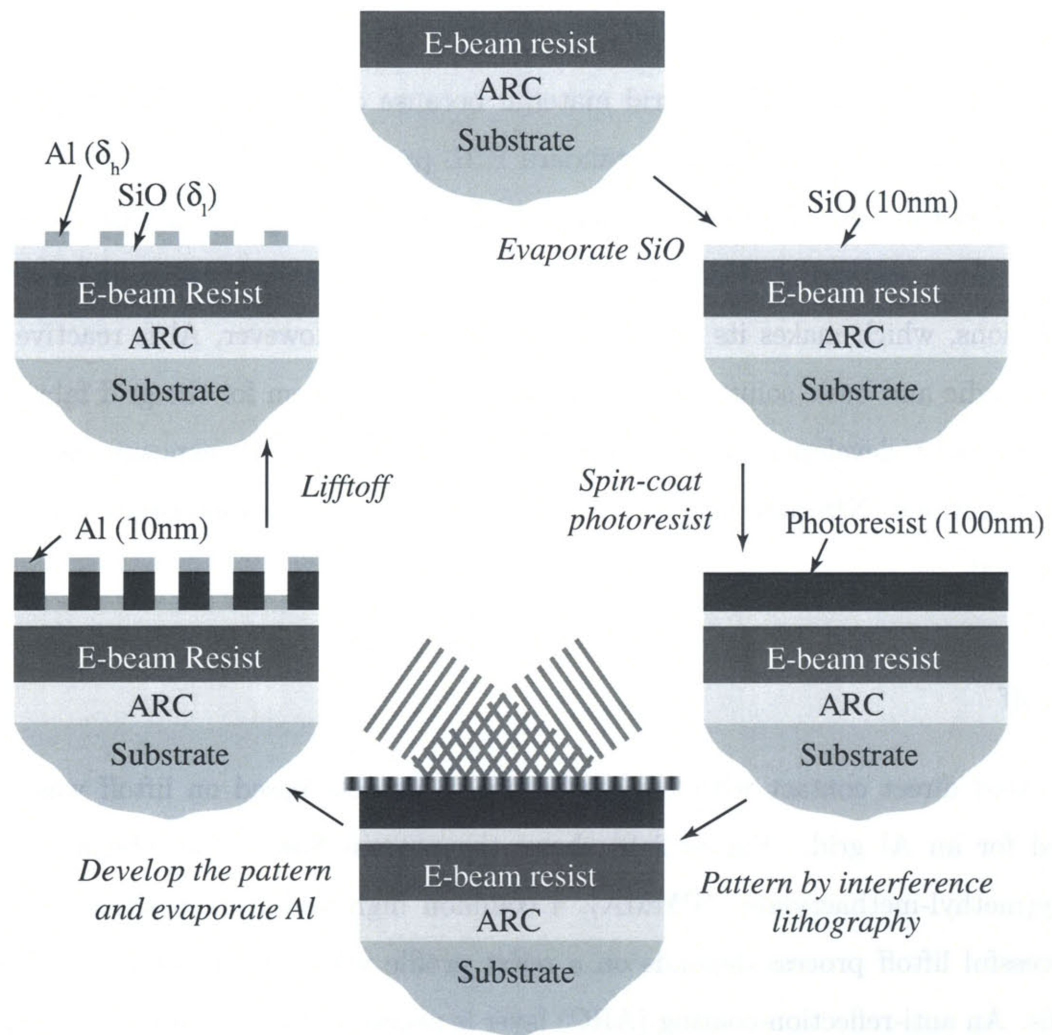

Figure 2-18: Al grid fabrication process. The process starts with a substrate coated with ARC and the e-beam resist. A layer of SiO (10 nm) is evaporated over the e-beam resist. The substrate is then spin-coated with photoresist (100 nm). After IL exposure and development, 10 nm Al is evaporated on the substrate. The grid is completed after a liftoff process.

opment, the pattern needs to be transferred twice, first into the ARC layer and then onto the substrate. The complexity of this process severely limits its usage for general practice, especially in production.

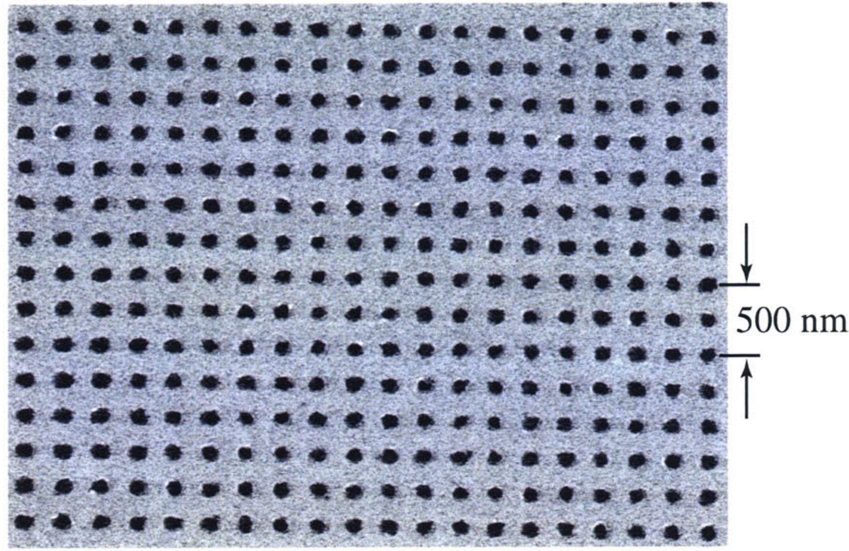

Figure 2-19: SEM images of an Al grid. The signal contrast is due to the differential yield between Al and evaporated SiO. The bright area is Al, and the dark area is SiO.

Photo-activated Etching

Vannikov et al. discovered that a mixture of certain organic chemicals can etch metal films, such as Al and Bi, when exposed to UV light of $300 \sim 400\,\text{nm}$ [67, 66, 24]. The mixture, or photoetchant, includes a donor, an acceptor, a precursor, and a binder. It can be spin-coated onto the metal as a thin film. When the donor and the acceptor react under the UV light, an acid forms. The acid will react with the metal, and the product will be moved into the photoetchant film by the precursor. After exposure, the photoetchant will be removed by an appropriate solvent, and the metal under the unexposed area will be left intact. The polymer binder is used to hold the donor and the acceptor together and to facilitate easy spin-coating.

The donor can be either diphenylamine (DPA), or diphenylbenzylamine (DPBA). DPA is more efficient in generating reactive radicals. The acceptor is either tetrabromomethane (CBr_4) or hexabromomethylsulfone ($CBr_3SO_2CBr_3$). The latter is highly toxic, hence, not suitable for general use. The concentration of the photoetchant is limited by the quality of the spin-coated film. When the concentration is too high, the photoetchant will form tiny crystals, and it becomes difficult to obtain uniform

coating. The polymer binders that have been tested are PMMA, poly(vinyl chloride) (PVC), polystyrene (PS), and *m*-cresol-formaldehyde novolac resin. Novolac resin provides good quality films with the highest photoetchant concentration. In addition, ferrocene is added as a catalyst to increase the sensitivity of the photoetchant, and a poly(vinyl alcohol) (PVA) coating is applied on top of the photoetchant to keep oxygen in the air from diffusing in.

When the donor (DPA) reacts with the acceptor (CBr_4) under UV, the following reaction occurs:

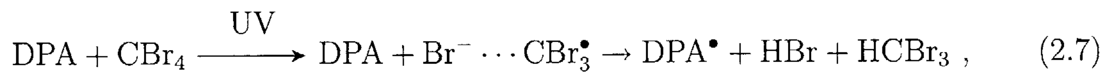

$$\mathrm{DPA} + \mathrm{CBr_4} \xrightarrow{\mathrm{UV}} \mathrm{DPA} + \mathrm{Br^-} \cdots \mathrm{CBr_3^\bullet} \rightarrow \mathrm{DPA^\bullet} + \mathrm{HBr} + \mathrm{HCBr_3}\ , \qquad (2.7)$$

and the acid reacts with Al:

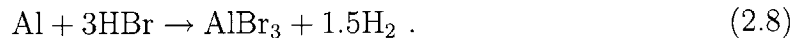

$$\mathrm{Al} + 3\mathrm{HBr} \rightarrow \mathrm{AlBr_3} + 1.5\mathrm{H_2}\ . \qquad (2.8)$$

After exposure, the substrate is baked at 70°C, under which DPA, the radical $DPA^\bullet$, and CBr_4 will react to form a colored product 4,4',4"-tri(anilino)triphenylmethane bromide (opal blue). Opal blue is responsible for the dissolution of $AlBr_3$ into the polymer binder so that the etching reaction can continue deep into the metal. Ferrocene also reacts with CBr_4 during both exposure and post-bake to form large amount of $Br^- \cdots CBr_3^\bullet$ radicals, which will help to produce the acid and opal blue. Details on the reactions can be found in [24].

The best etching result was achieved with a recipe given in Table 2.2. The reactants were then mixed in the novolac resin solution of 0.5 g/ml in chloroform. The substrate was covered with 100 nm PMMA and 8 nm evaporated Al. The photoetchant was spun at 3000 rpm to form ~300 nm thick film. It was then covered by 1 μm of PVA. The exposure was done with contact printing, where a mask was brought into intimate contact with the substrate while exposing to the light. The source used was a mercury-arc lamp. After exposure, the sample was left at room temperature for 14 hours before the photoetchant was removed.

Figure 2-20 shows an SEM image of the photochemically etched Al gratings. The

	DPA	CBr_4	ferrocene
Molecular formula	$C_{12}H_{11}N$	CBr_4	$C_{10}H_{10}Fe$
Molecular weight	169.21g	331.65g	210.05g
Molarity	1.2	2.1	1.0
Mass	67.69g	696.46g	210.05g

Table 2.2: Recipe of photoechant for Al.

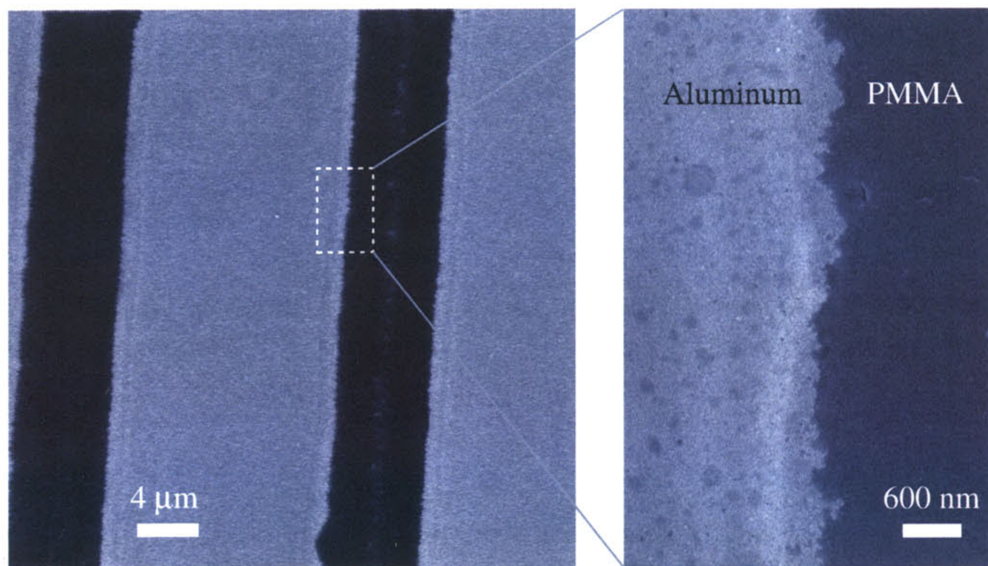

Figure 2-20: Photochemically etched Al gratings. A zoomed-in SEM image on the right side reveals the severe line-edge roughness, which can be explained by the non-uniformity in the chemical reaction.

result shows complete etching at exposed areas. A closer examination reveals that the line-edge roughness of the grating is about 150 nm, which is unacceptable for fabricating 250 nm grids. Baking at 70°C significantly shortens the reaction time, but it also increases line-edge roughness. The line-edge roughness can be explained by the non-uniformity of the reaction. The reaction starts at isolated locations, or hot spots, and these hot spots are randomly distributed. As the reaction continues, the spots grow larger, and eventually become continuous. However, semicircular "mouse bites" can form at the edge of the exposed area.

2.3.3 Cu Grid

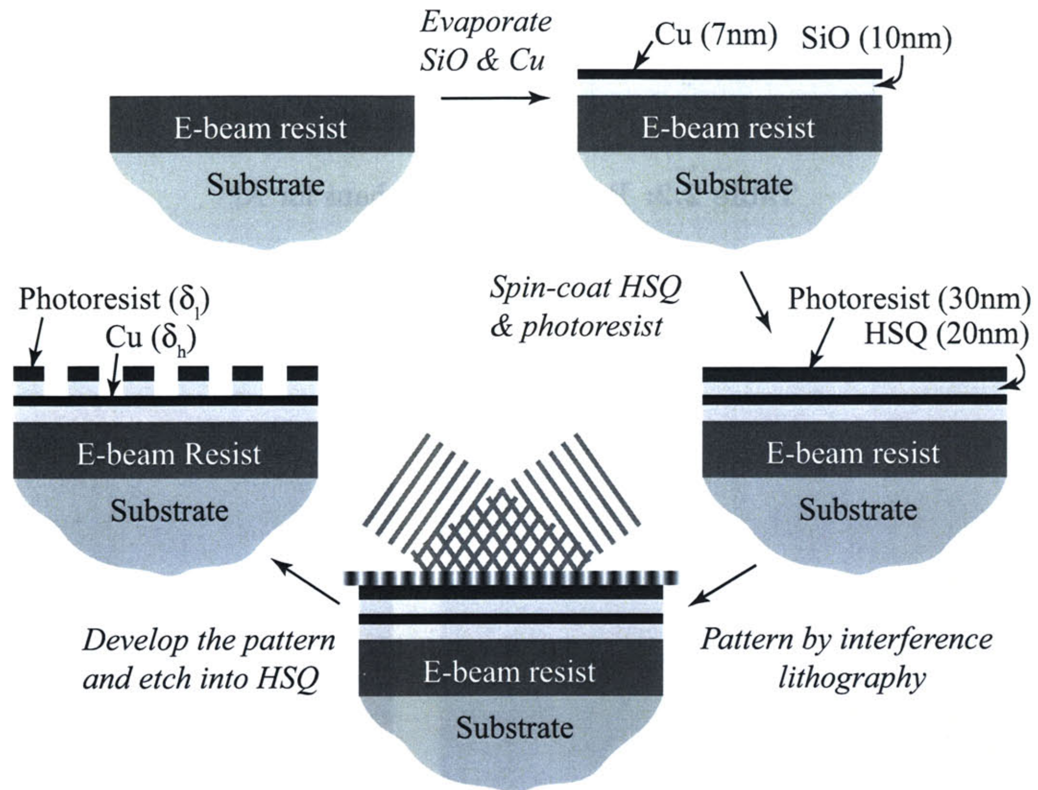

Figure 2-21: Cu-grid-fabrication process. A layer of SiO (10 nm) and Cu (7 nm) is first evaporated over the e-beam resist. The substrate is then spin-coated with HSQ(20 nm) and photoresist (30 nm). The grid is patterned by IL followed by development. HSQ is etched during development.

Figure 2-21 illustrates the process flow for making a Cu grid. A layer of 10 nm SiO and 7 nm Cu was first evaporated onto PMMA. SiO compensates the tensile stress in the Cu film; without it, cracks form in the Cu film. The substrate was then spin-coated with 20 nm hydrogen silsesquioxane (HSQ) and 30 nm PFI-88 (a positive i-line photoresist by Sumitomo). The baking conditions were 5 min at 90°C for HSQ and 1 min at 90°C for PFI-88. HSQ is a flowable low-k dielectric material, soluble in developers for common novolac-based photoresist, such as PFI-88. After the double IL exposure, the sample is developed for 30 sec, which etches the grid directly into HSQ. No further process is necessary before the e-beam exposure. SEM images of

a fabricated grid are shown in Fig. 2-22. The signal contrast is produced by the

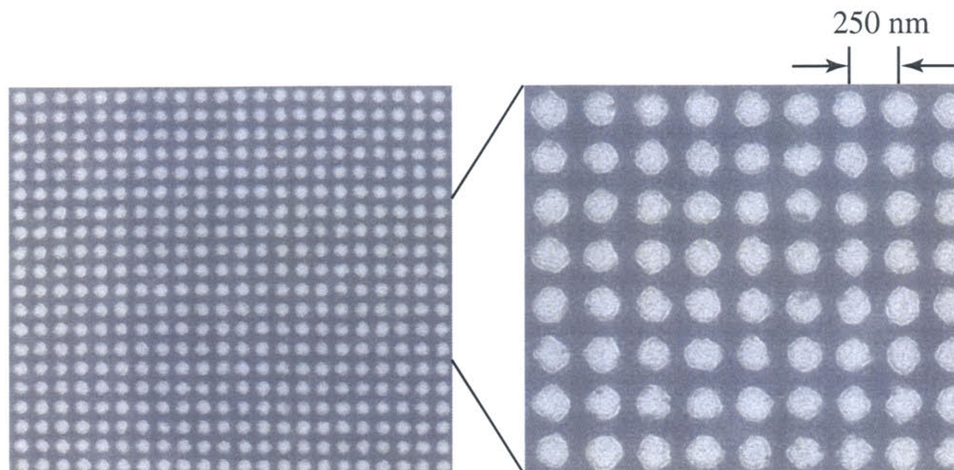

Figure 2-22: SEM images of a Cu grid. The signal contrast is due to the differential yield between Cu and photoresist. The bright holes are uncovered Cu, and the dark areas are masking photoresist.

differential SE yield between Cu and the photoresist. The exposed Cu appears as bright circles, and the surrounding areas covered by HSQ and photoresist appear dark. The uniformity is excellent over areas defined by IL exposure. There are some variations in the size, shape and placement of the holes, but these variations are random and localized and should not have any effect on the detection accuracy as explained in Chapter 3.

To avoid vertical standing waves, the thickness of the photoresist was kept very thin. As illustrated in Fig. 2-23, the thicknesses of the various layers were adjusted, based on a computer program, so that the null of the standing wave did not occur in the resist, and the difference in intensity between the top and bottom of the resist was minimized. In the experiments that difference factor was 2.4.

After e-beam exposure, the photoresist and HSQ can be removed by a flood exposure followed by development. Cu and SiO can be striped off using Cu etchant and buffered HF. Normal post-exposure processes for the e-beam resist can then be applied as usual. Figure 2-24 shows 200 nm gratings e-beam exposed through the grid at 10 keV. No deleterious effects of the fiducial grid on the exposure are observed.

During test exposures we discovered that although the Cu grid had little effect

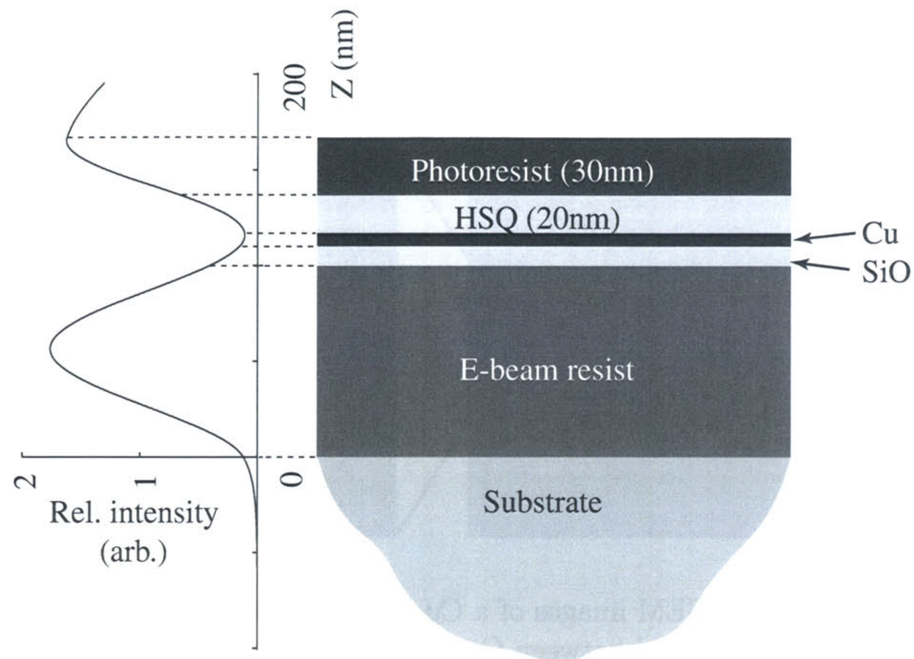

Figure 2-23: Relative light intensity in the resist stack during IL exposure. The e-beam resist used in this experiment is PMMA. The plot shows that a null occurs at the Cu surface. To achieve uniform exposure, 20 nm HSQ was placed between Cu and the photoresist. The intensities between the top and the bottom of the photoresist differ by a factor of 2.4.

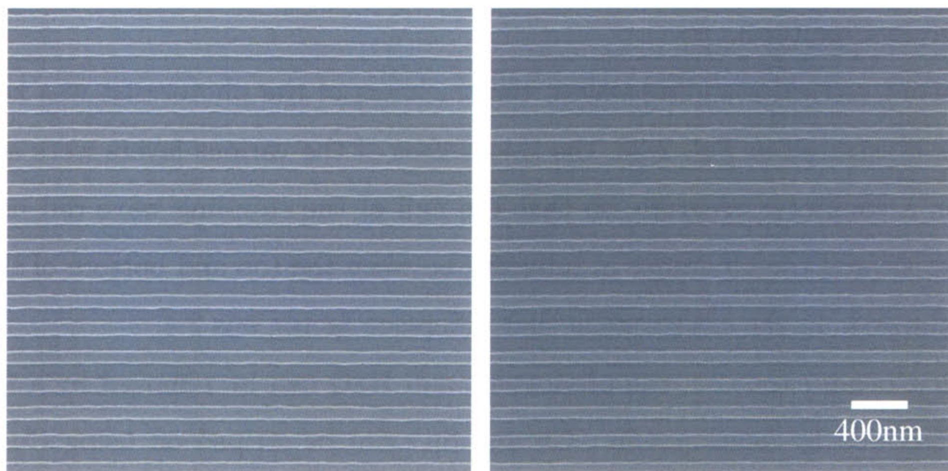

Figure 2-24: Exposure results at 10 keV. SEM image on the left shows gratings exposed in PMMA only. SEM image on the right shows gratings exposed through the grid.

on the line-edge roughness of the exposed gratings, the clearing dose became significantly lower. This increase in resist sensitivity can be explained by the unintentional exposure during e-beam evaporation. When the e-beam bombards the Cu target during evaporation, a significant amount of high-energy electrons are scattered into the chamber and expose the resist. This issue can be solved by using thermal evaporators instead. Another issue is the use of SiO. By adjusting the evaporation conditions such as pressure and deposition rate, it is possible to obtain low- or no-stress Cu films, and thereby eliminate the SiO layer. This will further reduce the complexity of the process, and avoid using HF.

2.3.4 Signal Contrast Measurement

As discussed in the next chapter, the accuracy of the beam-position-detection algorithm depends on the SNR of the reference signal. Assuming the reference signal is the sum of a sinusoidal signal and Gaussian white noise, its SNR (power ratio) can be expressed as

$$\mathrm{SNR} = \frac{A^2}{2\sigma^2}, \tag{2.9}$$

where A is the amplitude of the sinusoid and σ is the standard deviation of the white noise. Since the signal contrast is due to the differential yield of the grid materials, and the SE generation can be modelled as a Poisson process,

$$\mathrm{SNR} = \frac{D(\delta_h - \delta_l)^2}{8\delta_h} \tag{2.10}$$

where D represents the dose, or the number of primary electrons deposited at each pixel.

Measuring SE yields of the grid materials requires special equipment and is difficult to conduct. The signal contrast (SC), on the other hand, is very easy to measure with high accuracy. It is related to the SE yields by

$$\mathrm{SC} = \frac{A}{I_{mean}} = \frac{I_{max} - I_{min}}{I_{max} + I_{min}} = \frac{\delta_h - \delta_l}{\delta_h + \delta_l}, \tag{2.11}$$

where I_{mean} is the average intensity, or the dc component, of the signal, and I_{max} and I_{min} are the maximum and minimum intensities of the fundamental harmonics, respectively. Therefore,

$$\begin{aligned} \mathrm{SNR} &\propto \frac{\delta_h}{8}(\mathrm{SC})^2 \quad \text{for} \quad \delta_h \gg \delta_l \\ \mathrm{SNR} &\propto \delta_h(\mathrm{SC})^2 \quad \text{for} \quad \delta_h \approx \delta_l. \end{aligned} \tag{2.12}$$

Direct measurement of the SNR of the Cu grid is not available for us. However, performance data for the Al grid is available from previous experiments [29], which are presented in the next chapter. Since thin Cu and Al films have very similar SE yields, by comparing SEM images of Cu and Al grids, we can estimate the signal quality of the Cu grid. High-SNR SEM images of the Cu and Al grids were taken on MIT's Raith 150 SEBL tool. The signal contrast is then calculated with (2.11). The imaging conditions are identical for both grids, and the black level is measured at the Faraday cup on the sample holder. Figure 2-25 shows the SEM images for

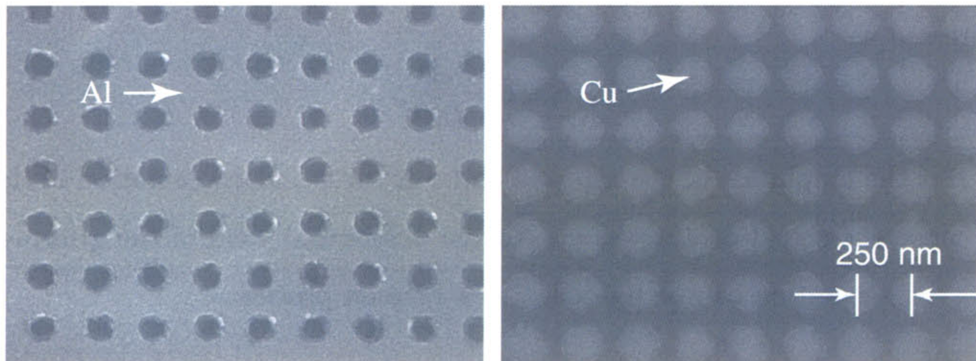

Figure 2-25: Contrast measurements for the Al and Cu grids. Signal contrasts are calculated for the fundamental frequencies in both cases. The signal contrast is 0.11 for the Al grid and 0.14 for the Cu grid. The black level is measured at the Faraday cup.

the Al and Cu grids used to calculate the signal contrasts. The Cu appears darker than Al, partly because most of the area on the Cu grid is covered by the low-yield photoresist, and BSE are much less efficient in generating SE from photoresist than from Al. The signal contrast of the Cu grid (0.14) is slightly higher than that of the

Al grid (0.11). Hence, the performance of the Cu grid is expected to be comparable to that of the Al grid.

2.4 Scintillation Grid

During early development stages of SPLEBL, the scintillation grid was the primary candidate for providing the reference signal. As discussed previously in this chapter, inorganic scintillators have higher conversion efficiencies, but slower response times than organic scintillators. The crystalline structures of the inorganic scintillators also make thin-film deposition difficult. Inorganic scintillators are much more resistant to radiation damages than organic ones, which can be both advantageous and disadvantageous. Organic scintillators can be easily spin-coated onto the substrate. They can be permanently quenched by UV or electron radiation. Hence, patterning grids into organic scintillators can be easily achieved with any of the IL schemes introduced in this chapter, and the process is extremely simple.

2.4.1 Scintillation-signal Detection

We designed two detection systems for scintillation signals: one installed on MIT's VS2A SEBL tool, and the other on the Raith 150 tool. The VS2A SEBL system was a research tool donated to MIT by IBM in the early 1990s. Figure 2-26 describes the detection system installed on VS2A. The PMT is positioned on the side of the substrate because of the limited space available in the vacuum chamber. To increase the collection efficiency, an elliptical mirror was installed. Figure 2-27 depicts the detection system installed in Raith 150. In this setup, a lens is placed close to the substrate to collect the photons. The scintillation signal is filtered before entering the PMT.

It is clear from the figures that the collection efficiencies are not very high on both systems. Assuming that the photons are emitted uniformly over all directions, the

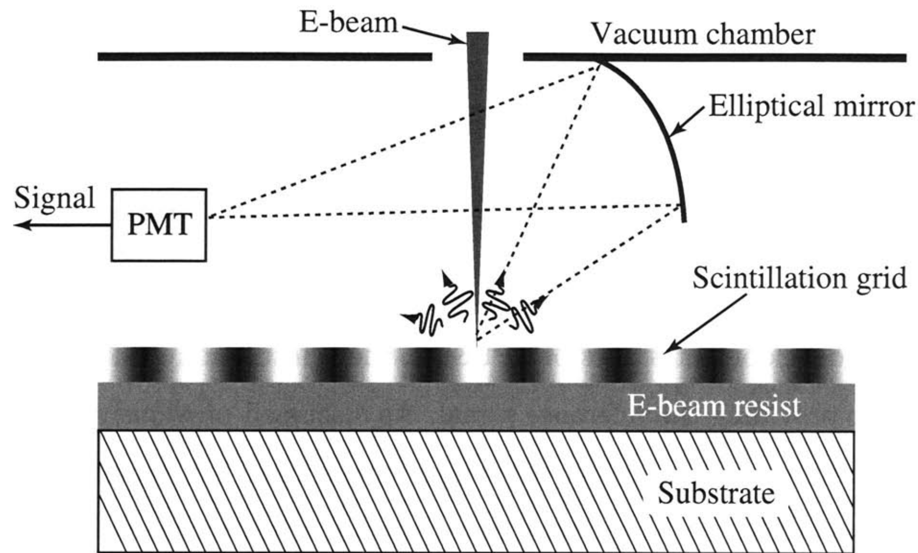

Figure 2-26: The scintillation-signal detector on VS2A. Because of the limited room available in the vacuum chamber, the PMT (Hamamatsu R7400U) is set to the side of the substrate. The photons generated during exposure is collected and focused onto the PMT by an elliptical mirror.

collection efficiency is simply

$$\text{collection efficiency} = \frac{\Omega_{\text{collecting element}}}{2\pi}\,, \tag{2.13}$$

in which the collecting element is the mirror and the lens for the two systems, respectively. The collection efficiencies are less than 5% for both systems.

2.4.2 Scintillation Materials

Based on a scintillation composition used for particle detection, Goodberlet et al. developed a recipe to suit the needs for SPLEBL. It consists of anthracene (the primary scintillator), 1,4-bis(t-phenyl- 2-oxazolyl)benzene (POPOP, the secondary scintillator), naphthalene (the energy-transfer molecule), and a polymer host that binds all the components together. The primary scintillator absorbs the radiation energy and emits photons in the UV region. The secondary scintillator shifts the wavelength of the emitted photons into the visible region to accommodate the spectrum peak of the

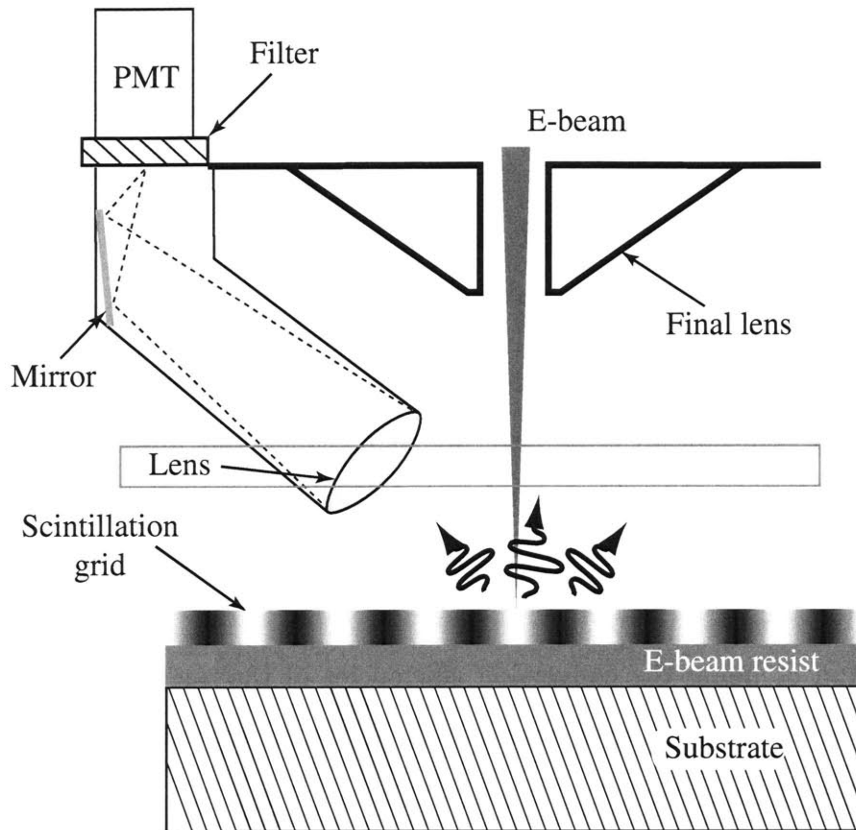

Figure 2-27: The scintillation-signal detector on Raith 150. The light is collected by the lens located just above the substrate, and reflected into the PMT (Hamamatsu R6094) installed outside of the vacuum chamber. The optical filter placed in front of the PMT blocked the HeNe light from the laser interferometer.

PMT. The energy-transfer molecule improves the conversion efficiency by transferring part of the energy absorbed by the host polymer to the primary scintillator. This scintillator system can be easily quenched by the 351 nm UV light used on the IL system. However, its poor resistance to e-beam exposure, in particular the backscattered electrons, decreases the SNR of the reference signal during exposure.

In the early experiments, the scintillation materials were directly mixed into PMMA, which acted as both the host binder for the scintillator and the e-beam resist. Since the additives affected the properties of PMMA as an e-beam resist, later development focused on different host polymers. Finlayson systematically studied several groups of scintillation materials and host polymers. One of the brightest scintillation

system was based on para-terphenyl (primary), POPOP (secondary), and poly-vinyl toluene (PVT) (host polymer). It achieved 3.6 times higher efficiency and 3 times higher e-beam-exposure resistance than the scintillator developed by Goodberlet.

2.4.3 Scintillation Signal Analysis

Hastings and Finlayson conducted a detailed analysis on the various scintillators, and the results were presented in [26] and [20]. From their analysis we can conclude that 1) most of the scintillation grids have higher contrast, but lower SNR than the Al-based SE grid for a comparable spatial period, e.g., 1μm, and 2) the signal contrast of the scintillation grid decreases dramatically when the grid period becomes less than 1μm.

Let δ_l and δ_h being the conversion efficiencies of the quenched and unquenched regions of the scintillation grid, and $a = \delta_l/\delta_h$ the signal contrast defined in (2.11) can be expressed as

$$\mathrm{SC} = \frac{1-a}{1+a} \, . \tag{2.14}$$

For grid period greater than 1μm, most scintillation grids have lower a than the Al-based SE grid, hence, their signal contrast is also higher. A higher signal contrast, however, does not automatically guarantee a higher SNR. According to equation (3.45) given in the next chapter, the SNR, γ, of the scintillation grid is also proportional to the conversion efficiency of the unquenched scintillator

$$\gamma \propto (1-a)^2 \, \delta_h \, . \tag{2.15}$$

To estimate the conversion efficiency of a 100 nm-thick PMMA-based scintillator film, we assume that the energy loss of the primary electrons follows the Bethe Law [23, 32]:

$$\frac{dE}{ds}\left(\frac{\mathrm{keV}}{\mathrm{cm}}\right) = -2\pi e^4 \frac{n_e}{E} \ln\left(\frac{1.166E}{J}\right) \, , \tag{2.16}$$

where E is the energy of the primary electrons, $2\pi e^4 = 1.304 \times 10^{-19}$ for E in keV, n_e is the number of atomic electrons per cm^3, and J the mean excitation energy. J is

obtained empirically to be 65.6 eV for PMMA [3]. Let $E = 10\,\text{keV}$, and assume that the primary electrons travel in straight paths in the thin PMMA layer, the energy lost in PMMA is ~266 eV. Suppose that 2% of the deposited energy gets converted to 400 nm photons (a very optimistic assumption), and the collection efficiency of the detector is 5%, then the efficiency of the signal-generation system before PMT is only 8%, which is lower than that of the Al grid. As the backscattered electrons damage the scintillator in the surrounding area during e-beam exposure, the conversion efficiency of the scintillation becomes even lower.

When the grid period goes below 1μm, the signal contrast of the scintillation grid degrades rapidly. This phenomenon is caused by two different effects. During IL exposure, the vertical standing wave formed in the scintillator layer reduces the quenching contrast. This problem exists for both large- and small-period grids, but becomes much more pronounced for the latter. In addition, the IL exposure with 351 nm only damages the secondary scintillator. For small-period grids, photons generated by the primary scintillator have a high probability of travelling in the material and exciting secondary scintillation molecules in the unquenched region. Light with shorter wavelengths can effectively quench the primary scintillator, but it will also alter the properties of many e-beam resists, hence not suitable for SPLEBL.

Because of its low SNR, low spatial resolution, and poor damage resistance to e-beam exposure, scintillation grid was eventually surpassed by the SE grid for real-time SPLEBL.

Chapter 3

Electron-beam-position Detection

In EBL exposure, the number of primary electrons deposited per pixel is limited by the step size and the exposure dose of the e-beam resist, and this number is extremely low under normal conditions. For an exposure dose of $100\,\mu\mathrm{C/cm^2}$ at a 10 nm step size, a typical setting for PMMA at 10 keV, only 625 electrons are deposited per pixel. Although the generation efficiency of SE is one of the highest among all types of electron-induced emissions, it is still much lower than 100% at high-acceleration voltages. For example, the SE yields for most materials are below 30% at 10 keV, and they decrease further as e-beam energy becomes higher. At such a low signal level, stochastic noise often dominates the SE-reference signal. The analysis in the previous chapter illustrates that the noise bottleneck is at the SE generation and collection, and signal amplification at the following stages will not improve the SNR of the reference signal. As a result, the SNR of the reference signal is poor, and the detection accuracy suffers accordingly. To achieve acceptable beam-position-detection accuracy with the reference signal available, a high-performance estimation algorithm becomes essential.

An estimation algorithm based on Fourier techniques provides an elegant solution to this problem. The algorithm calculates a phase based on a large number of samples of the reference signal, and uses the phase to determine the beam position. This special technique is referred to as spatial-phase locking. By doing so, the noise in the reference signal is effectively averaged out, and the SNR of the reference signal is

significantly improved. Although the improvement comes at a cost of reduced bandwidth of the feedback loop, it does not necessarily degrade the dynamic performance of SPLEBL. The analysis given in Chapter 1 shows that the targeted disturbances have frequencies that are orders of magnitude lower than the sampling frequency of the reference signal.

The Fourier-based algorithm also allows the use of a grid period that is much larger than the targeted placement accuracy. For example, a change of 1 nm in beam position can be readily detected with a grid of 250 nm-period when the algorithm has a phase detectivity of 1.44°. Such a detectivity can be easily achieved with a reasonable SNR. Furthermore, the algorithm is insensitive to randomly-distributed local defects in the fiducial grid, such as misplacement or irregularity in the grid shapes, because the signal noise caused by these defects can also be averaged out by the algorithm. These properties of the algorithm relax considerably the complexity of the grid-fabrication process.

3.1 Parametric Estimator of a Sinusoidal Signal

Randomness is always present in the physical world, and any physical signal is more or less corrupted by noise. Estimation theory was developed for estimating a variable x based on the observation of another variable z when the latter is heavily corrupted by noise. The variable x can be either random or nonrandom [73]. In the first case, the relationship between x and z can be fully characterized by the conditional density distribution $p_{z|x}(z|x)$. In the second case, x can be viewed as an unknown parameter of z, and their relationship is described by $p_z(z;x)$.

3.1.1 Unbiased Estimator

Let $\hat{x}(z)$ denote an estimator of x, the bias and the error covariance of the estimator are defined respectively as the expected value and the variance of the estimation error

$\mathrm{e}(z) = \hat{x}(z) - x$, or

$$\mathrm{b}_{\hat{x}}(x) = E\left[\mathrm{e}(z)\right] = E\left[\hat{x}(z) - x\right] \tag{3.1}$$

$$\mathrm{var}\left(\mathrm{e}(x)\right) = E\left[\left[\mathrm{e}(z) - \mathrm{b}_{\hat{x}}(x)\right]^2\right] \ . \tag{3.2}$$

As for any stochastic process, the bias and error covariance characterize the behavior of the estimator. When evaluating the performance of an estimator both factors must be taken into consideration. There are many examples of estimators with small error covariances but large biases, and these estimators are certainly not desirable. In general, it is impossible to find an estimator that minimizes both the bias and the error covariance, hence the searching effort is focused on the so-called unbiased estimators that have $\mathrm{b}_{\hat{x}}(x) = 0$. The goal then becomes to find an unbiased estimator with the minimum error covariance. For an unbiased estimator, the error covariance is simply the variance of the estimator:

$$\begin{aligned}\mathrm{var}\left(\mathrm{e}(x)\right) &= E\left[\mathrm{e}^2(z)\right] \\ &= E\left[(\hat{x}(z) - x)^2\right] \\ &= \mathrm{var}\left(\hat{x}(x)\right) \ .\end{aligned} \tag{3.3}$$

An unbiased estimator does not always exist. In fact, when the relationship between x and z is nonlinear, an unbiased estimator does not exist. Fortunately, the Fourier-based estimator used for SPLEBL will behave like an unbiased estimator when certain conditions are satisfied. More details will be given later.

3.1.2 Cramér-Rao Bound

The Cramér-Rao bound (CRB) is a lower bound on the variances of all unbiased estimators $\hat{x}$ for x, and is defined as:

$$\lambda_{\hat{x}}(x) \geq \frac{1}{I_z(x)} \ . \tag{3.4}$$

The nonnegative quantity $I_z(x)$ is referred to as the Fisher information, which can be calculated by

$$\begin{aligned} I_z(x) &= E\left[\left(\frac{\partial}{\partial x}\ln p_z(z;x)\right)^2\right] \\ &= -E\left[\frac{\partial^2}{\partial^2 x}\ln p_z(z;x)\right] . \end{aligned} \tag{3.5}$$

An unbiased estimator that satisfies the CRB is called an efficient estimator. The existence of an unbiased estimator does not guarantee an efficient estimator. On the other hand, once an efficient estimator is found, one needs look no further, because this is the best achievable.

3.1.3 Phase Estimation

In the case of SPLEBL, the observation is the reference signal, and the variable to be estimated is the spatial phase of the reference signal, from which the beam position can be calculated. Before jumping into the two-dimensional (2-D) case, the analysis of the one-dimensional (1-D) case is given below. For simplicity, a sinusoid will be used to represent the reference signal in the 1-D case.

A sinusoidal signal corrupted by an additive white Gaussian noise can be expressed as

$$z[n] = x[n] + w[n] = A\cos(\omega_0 n + \Theta) + w[n], \; n = 0, 1, \ldots, N-1, \tag{3.6}$$

where $A > 0$, $0 \leq \omega_0 < \pi$, and $w[n]$ are independent, identically distributed random variables with Gaussian probability distribution function $N(0, \sigma^2)$. A, ω_0, and Θ are all nonrandom parameters that can be estimated from the observation $z[n]$. For SPLEBL, ω_0 is predetermined by the grid, and A is of no importance. Estimating the phase Θ is the focus of SPLELB.

The joint probability function of

$$\mathbf{z} = \begin{bmatrix} z[1] \\ z[2] \\ \vdots \\ z[N-1] \end{bmatrix} \tag{3.7}$$

is simply

$$p_z(\mathbf{z};\Theta) = \left(\frac{1}{\sigma\sqrt{2\pi}}\right)^N \prod_{n=0}^{N-1} \exp\left(-\frac{[z[n] - A\cos(\omega_0 n + \Theta)]^2}{2\sigma^2}\right) . \tag{3.8}$$

It turns out that a convenient phase estimator, commonly denoted as $\hat{\Theta}$, is the *periodogram-based* estimator defined by:

$$\hat{\Theta}(z) = \tan^{-1}\left(\frac{\mathrm{Im}\{Z_N(e^{j\omega_0})\}}{\mathrm{Re}\{Z_N(e^{j\omega_0})\}}\right) = -\tan^{-1}\left(\frac{\mathrm{Im}\{Z_N(e^{-j\omega_0})\}}{\mathrm{Re}\{Z_N(e^{-j\omega_0})\}}\right) , \tag{3.9}$$

where

$$Z_N(e^{\pm j\omega_0}) = \frac{1}{\sqrt{N}} \sum_{n=0}^{N-1} z[n] e^{\mp j\omega_0 n} \tag{3.10}$$

is the periodogram of the data segment $z[n]$ at ω_0. Both forms of the estimator shown in (3.9) will work equally well, and the first form will be used for analysis here. (A detailed description of the relationship between the phase of the sinusoidal signal and its periodogram is provided in Appendix A.) This estimator is both intuitively appealing and computationally efficient. For large N,

$$\begin{aligned} Z_N(e^{j\omega_0}) &= \frac{A}{\sqrt{N}} \sum_{n=0}^{N-1} \cos(\omega_0 n + \Theta) e^{-j\omega_0 n} + \frac{1}{\sqrt{N}} \sum_{n=0}^{N-1} w[n] e^{-j\omega_0 n} \\ &\approx \frac{A}{\sqrt{N}} \sum_{n=0}^{N-1} \cos(\omega_0 n + \Theta) e^{-j\omega_0 n} , \end{aligned} \tag{3.11}$$

i.e., the summation term of the white noise $w[n]$ averages to zero. From (3.1), the

bias of the estimator is

$$\begin{aligned} b_{\hat{\Theta}}(\Theta) &= E\left[\hat{\Theta}(z) - \Theta\right] = E\left[\hat{\Theta}(z)\right] - \Theta \\ &= E\left[\tan^{-1}\left(\frac{\mathrm{Im}\{Z_N(e^{j\omega_0})\}}{\mathrm{Re}\{Z_N(e^{j\omega_0})\}}\right)\right] - \Theta \\ &= 0 \end{aligned} \tag{3.12}$$

for large N. Hence, this estimator is an asymptotically unbiased estimator. In other words, when the number of samples N is large, the estimator becomes unbiased. More precisely, N is considered large when

$$\frac{\pi}{N} \ll \omega_0 \ll \pi\left(1 - \frac{1}{N}\right) . \tag{3.13}$$

The left half of (3.13) implies that there should be a reasonable number of samples per period, and the right half of it implies that the samples should be collected over a reasonable number of periods.

From (3.8),

$$\ln p_z(\mathbf{z};\Theta) = -\frac{N}{2}\ln(2\pi\sigma^2) - \frac{1}{2\sigma^2}\sum_{n=0}^{N-1}\left[z[n] - A\cos(\omega_0 n + \Theta)\right]^2 \tag{3.14}$$

the Fisher information can be calculated by (3.5):

$$\begin{aligned} I_z(\Theta) &= -\frac{1}{\sigma^2}\sum_{n=0}^{N-1} A^2 \sin^2(\omega_0 n + \Theta) \\ &= \frac{A^2 N}{2\sigma^2}\left(1 - \frac{1}{N}\sum_{n=0}^{N-1}\cos(2\omega_0 n + 2\Theta)\right) . \end{aligned} \tag{3.15}$$

When N is large in the sense of (3.13),

$$I_z(\Theta) = \frac{A^2 N}{2\sigma^2} , \tag{3.16}$$

and the CRB of the estimator is

$$\text{var}\,\hat{\Theta}(y) \geq \frac{2\sigma^2}{A^2 N} = \frac{1}{\gamma N}\ , \tag{3.17}$$

where $\gamma = A^2/2\sigma^2$ is the SNR of the original signal $z[n]$.

It is clear from (3.17) that the CRB is inversely proportional to both γ and N. To better understand the behavior of the CRB and the performance of the estimator, it is useful to decompose the periodogram into signal and noise:

$$Z_N(e^{j\omega}) = X_N(e^{j\omega}) + W_N(e^{j\omega})\ , \tag{3.18}$$

where

$$X_N(e^{j\omega}) = \frac{1}{\sqrt{N}} \sum_{n=0}^{N-1} x[n] e^{-j\omega n} \tag{3.19}$$

and

$$W_N(e^{j\omega}) = \frac{1}{\sqrt{N}} \sum_{n=0}^{N-1} w[n] e^{-j\omega n}\ . \tag{3.20}$$

The power density of the signal periodogram is

$$|X_N(e^{j\omega})|^2 = \frac{A^2}{4N} \left\{ \left[\frac{\sin[(\omega-\omega_0)N/2]}{\sin[(\omega-\omega_0)/2]} \right]^2 + \left[\frac{\sin[(\omega+\omega_0)N/2]}{\sin[(\omega+\omega_0)/2]} \right]^2 \right\}\ , \tag{3.21}$$

and that of the noise is

$$E\left[|W_N(e^{j\omega})|^2\right] = \frac{1}{N} \sum_{n=0}^{N-1} \sum_{m=0}^{N-1} E[w[n]w[m]] e^{j\omega(n-m)} = \sigma^2\ . \tag{3.22}$$

As shown in Fig. 3-1, the power density of the periodogram reaches its peak at frequency $\omega = \omega_0$:

$$|X_N(e^{j\omega})|^2 = \frac{A^2 N}{4}\ . \tag{3.23}$$

By defining the SNR of the periodogram as

$$\gamma_{\hat{\Theta}}(\omega) = \frac{|X_N(e^{j\omega})|^2}{\sigma^2}\ , \tag{3.24}$$

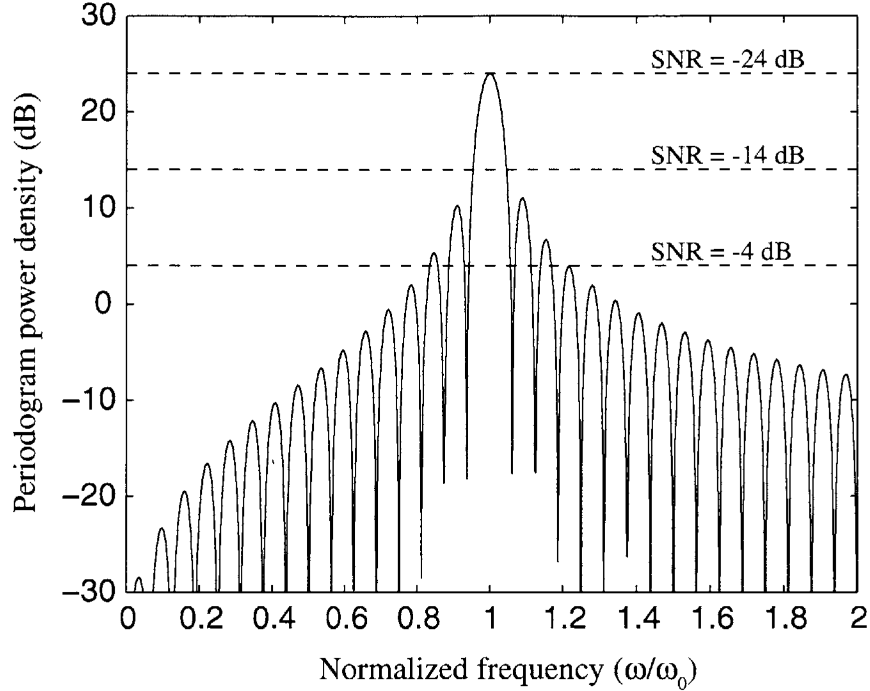

Figure 3-1: The solid curve plots the periodogram power density of the sinusoidal signal, $10\log_{10}(|X_N(e^{j\omega})|^2)$ for $\omega_0 = 4\pi/125$ and $N = 1000$, and the dashed lines depict the power density of the noise, $\sigma^2 = 10\log_{10}(E[|X_N(e^{j\omega})|^2])$, corresponding to various values of SNR of the original signal. The power density of the sinusoidal signal reaches its peak at $\omega = \omega_0$.

it also reaches its maximum at $\omega = \omega_0$

$$\gamma_{\hat{\Theta}}(\omega_0) = \frac{A^2 N}{4\sigma^2} = \frac{1}{2}\gamma N \ . \tag{3.25}$$

Comparing with the SNR of the original signal, the SNR of the periodogram-based estimator increases by a factor of $N/2$. This special property of the periodogram-based estimator is the key to the success of the position-detection algorithm.

The dashed lines in Fig. 3-1 represent the power densities of noise corresponding to various values of signal SNR. When the noise power density exceeds that of the sinusoidal signal, the phase can no longer be accurately detected. The performance of the phase estimator is also sensitive to the value of the phase. When Θ is close to $\pi/2$, the estimator requires a much higher SNR, or a much larger N for an accurate

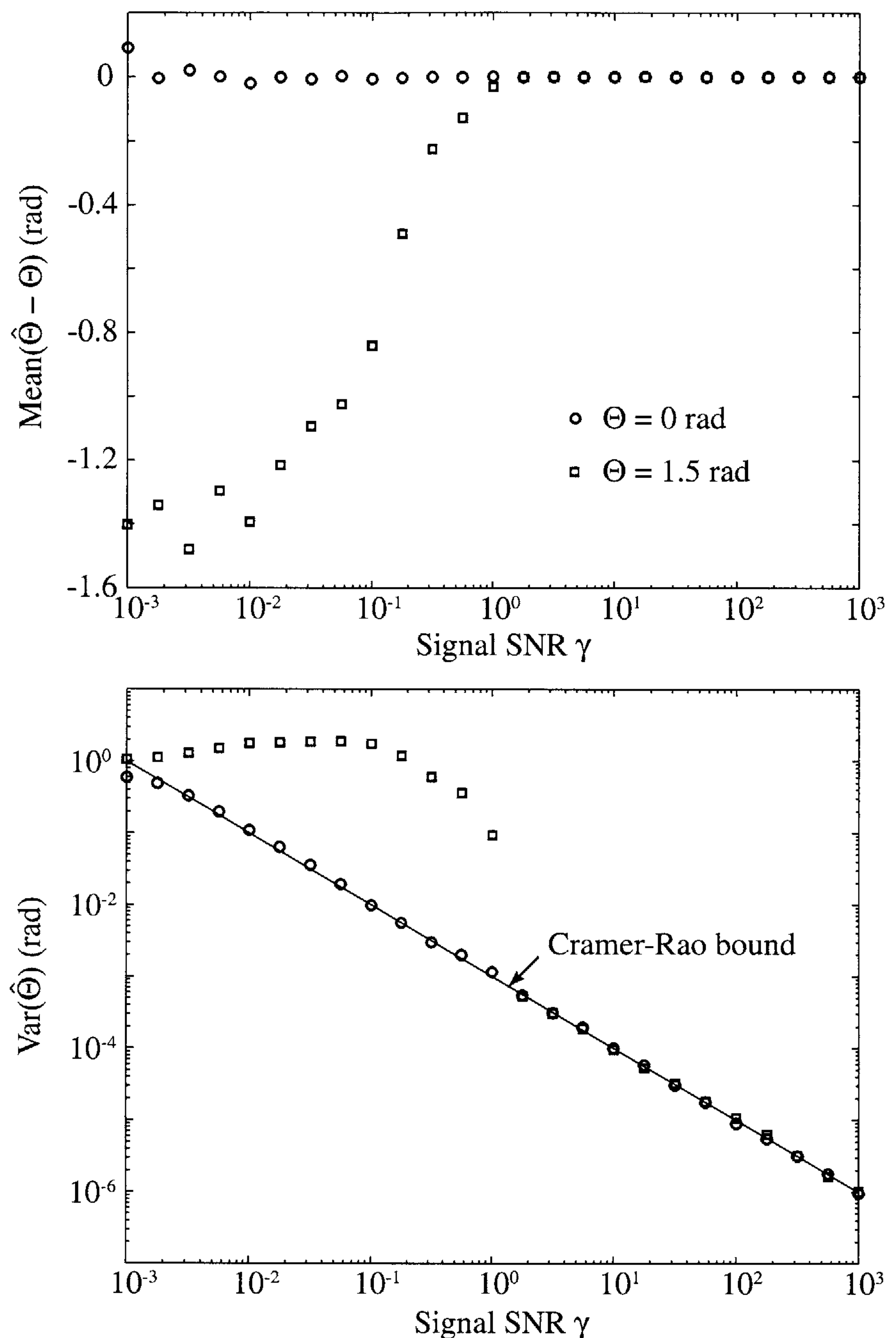

Figure 3-2: Simulation results of a phase estimator for a 16-period sinusoidal signal corrupted by additive Gaussian white noise with $N = 1000$. The upper graph plots the mean of the bias $\hat{\Theta} - \Theta$ for $\Theta = 0\,\text{rad}$ and $\Theta = 1.5\,\text{rad}$. For the case of $\Theta = 1.5\,\text{rad}$, the bias is very large for low signal SNR, and it converges to zero when $\gamma > 1$. The lower graph plots the variance and the Cramér-Rao bound (CRB) of the estimator. The variance converges to CRB when the signal SNR is greater than 1. This is called the capturing effect.

estimation than when Θ is close to zero. This behavior becomes quite clear in Fig. 3-2, and it is very undesirable. Note that when the bias is large, the CRB becomes meaningless.

In SPLEBL, the phase of the reference signal Θ_p at any given location is determined by pre-exposure calibration. The aim of the phase estimator is the phase error $\Delta\Theta$ caused by environmental disturbances, which is usually very small. This special characteristic of SPLEBL makes it possible to avoid estimating $\Theta \sim \pi/2$ by using $Z_N(e^{j\omega_0+\Theta_p})$ in (3.9), instead of $Z_N(e^{j\omega_0})$.

3.2 Spatial-phase-locking Algorithm

The extension of the phase estimator to the 2-D case is fairly straightforward. For simplicity, the derivation given below is conducted in the continuous-time domain, and the signal is assumed to extend over $(-\infty, +\infty)$.

Mathematically, any 2-D periodic function $f(x, y)$ can be expressed in terms of its Fourier series expansion:

$$f(x,y) = \sum_{m=-\infty}^{\infty} \sum_{n=-\infty}^{\infty} a_{m,n} e^{j(mk_{x0}\cdot x + nk_{y0}\cdot y)}, \tag{3.26}$$

where (m, n) are integers, and k_{x0} and k_{y0} are the fundamental spatial frequencies in the x and y directions, respectively. The spatial frequencies k_{x0} and k_{y0} are equivalent to ω_0 in the 1-D analysis. Letting $k_{x0} = k_{y0} = k_0$ and the two axes of symmetry to be orthogonal (as shown in Fig. 3-3), Equation (3.26) can be simplified as:

$$f(x,y) = a_0 + a_{1,0}\cos(k_0 \cdot x + \Theta_{1,0}) + a_{0,1}\cos(k_0 \cdot y + \Theta_{0,1}) + h.o. \tag{3.27}$$

The term "$h.o.$" represents the sum of all higher order terms with $|m| + |n| > 1$. These terms are generally ignored by the estimator for their low SNR.

Since SPLEBL scans in a raster fashion, it can acquire the x coordinate of the beam much faster than the y coordinate with the grid shown in Fig. 3-3. This is due

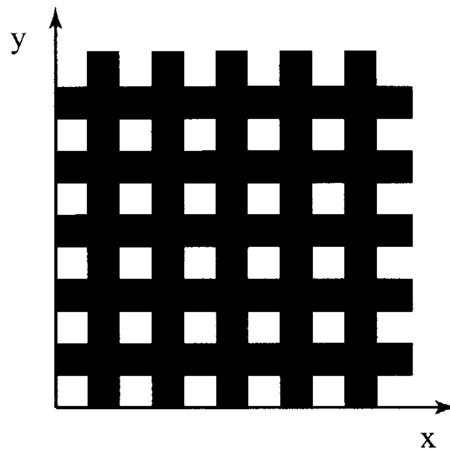

Figure 3-3: Orthogonal reference-grid pattern for SPLEBL. The axes of symmetry for the grid are parallel to the x and y axes, respectively. The fundamental spatial frequencies $k_{x0} = k_{y0} = k_0$.

to the fact that the phase estimator samples multiple grid periods before it can make an accurate calculation. The different detection speed will cause greater placement errors in the y direction than in the x direction. This problem can be easily solved by introducing a small rotation θ to the grid as shown in Fig. 3-4 [26, 29]. For such

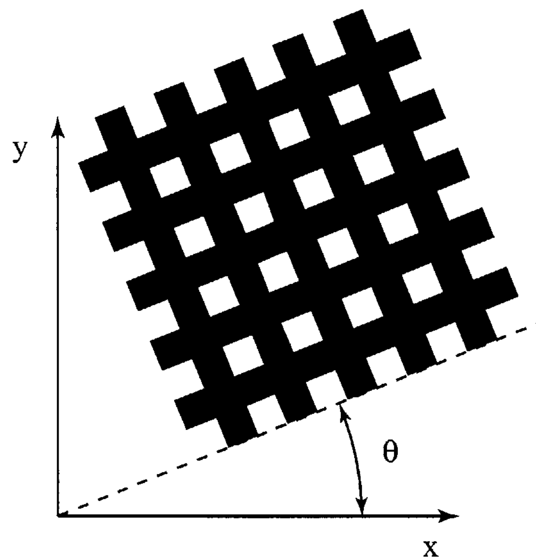

Figure 3-4: Reference grid for SPLEBL. Rotated by a small angle θ for simultaneous detection of both x and y coordinates [26, 29].

a setup, Equation (3.27) without the "h.o." terms becomes

$$\begin{aligned} f_{truncate}(x,y) = a_0 &+ a_{1,0}\cos[k_0(\cos\theta\cdot x + \sin\theta\cdot y) + \Theta_{1,0}] \\ &+ \ a_{0,1}\cos[k_0(-\sin\theta\cdot x + \cos\theta\cdot y) + \Theta_{0,1}] \ . \end{aligned} \tag{3.28}$$

Without loss of generality, we can define

$$\begin{aligned} k_{HI} &= k_0\cos\theta, & k_{LO} &= k_0\sin\theta, \\ a_{HI} &= a_{1,0}, & a_{LO} &= a_{0,1}, \\ \Theta_{1,0} &= 0, & \Theta_{0,1} &= 0, \end{aligned}$$

such that

$$\begin{aligned} f_{truncate}(x,y) = a_0 &+ a_{HI}\cos(k_{HI}\cdot x + k_{LO}\cdot y) \\ &+ \ a_{LO}\cos(-k_{LO}\cdot x + k_{HI}\cdot y) \ , \end{aligned} \tag{3.29}$$

where HI stands for the high frequency component and LO for the low frequency component since for small θ, $k_0\cos\theta > k_0\sin\theta$.

Figure 3-5 shows a grid used in actual exposure. This is a rotated Al grid on evaporated SiO with a period of 246 nm and $\theta = 21°$. The fundamental frequencies, k_{HI} and k_{LO}, the higher harmonics, and their sums and differences are all visible in the spectrum. To accurately estimate the phases of the fundamentals, the angle θ must be carefully chosen so that none of the components will overlap with the fundamentals. For example, when $\theta = 45°$, the two fundamentals will overlap, and their phases can no longer be detected separately.

By expressing the actual beam position as the sum of its nominal position (x_p, y_p) and a small perturbation $(\Delta x, \Delta y)$, Equation (3.29) becomes

$$\begin{aligned} f_{truncate}(x,y) = a_0 &+ a_{HI}\cos(k_{HI}\cdot x_p + k_{LO}\cdot y_p + k_{HI}\cdot\Delta x + k_{LO}\cdot\Delta y) \\ &+ \ a_{LO}\cos(-k_{LO}\cdot x_p + k_{HI}\cdot y_p - k_{LO}\cdot\Delta x + k_{HI}\cdot\Delta y) \ . \end{aligned} \tag{3.30}$$

For a single line-scan along x, the terms $k_{LO}\cdot y_p$ and $k_{HI}\cdot y_p$ are constant phase terms,

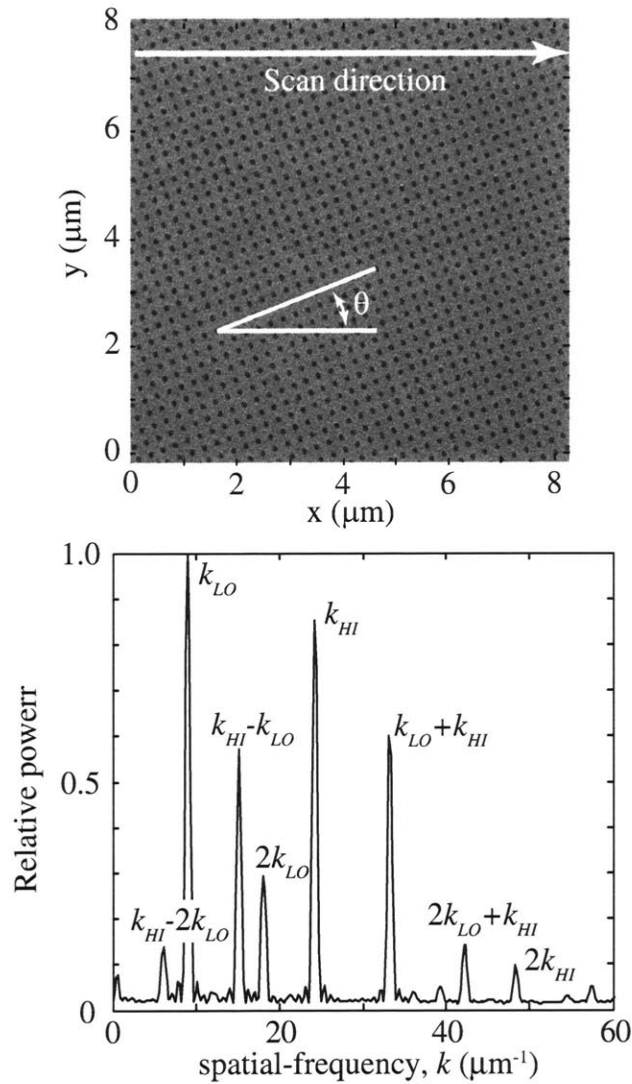

Figure 3-5: The top SEM image is a rotated 246 nm-period Al grid on evaporated SiO. The lower graph plots the power spectrum of the image. Besides the fundamental frequencies k_{HI} and k_{LO}, there are other components that have $|m| + |n| > 1$. (Taken from reference [26].)

which can be precalculated. The terms containing Δx and Δy correspond to phase errors that are to be estimated. Since the y_p terms are constant, one can take the Fourier transform of (3.29) with respect to x_p alone:

$$\begin{aligned} F_x(k, y_p) &= 2\pi a_0 \delta + \pi a_{HI} \delta(k \pm k_{HI}) e^{\pm j(k_{HI} \cdot \Delta x + k_{LO} \cdot \Delta y + k_{LO} \cdot y_p)} \\ &+ \pi a_{LO} \delta(k \pm k_{LO}) e^{\mp j(-k_{LO} \cdot \Delta x + k_{HI} \cdot \Delta y + k_{HI} \cdot y_p)} . \end{aligned} \tag{3.31}$$

Similar to the case in (3.9), the phase errors $\Delta\Theta_{HI}$ and $\Delta\Theta_{LO}$ can be calculated in four different ways depending on which pair of (k_{HI}, k_{LO}) terms are used. All of the four forms are listed below, and their performance is identical.

Form 1:

$$\begin{aligned} \Delta\Theta_{HI}(e^{-j(k_{HI} \cdot x + k_{LO} \cdot y)}) &= k_{HI} \cdot \Delta x + k_{LO} \cdot \Delta y \\ \Delta\Theta_{LO}(e^{-j(-k_{LO} \cdot x + k_{HI} \cdot y)}) &= -k_{LO} \cdot \Delta x + k_{HI} \cdot \Delta y \\ \Delta\hat{x} &= \frac{1}{k_0}(\cos\theta \cdot \Delta\hat{\Theta}_{HI} - \sin\theta \cdot \Delta\hat{\Theta}_{LO}) \\ \Delta\hat{y} &= \frac{1}{k_0}(\sin\theta \cdot \Delta\hat{\Theta}_{HI} + \cos\theta \cdot \Delta\hat{\Theta}_{LO}) \end{aligned} \tag{3.32}$$

Form 2:

$$\begin{aligned} \Delta\Theta_{HI}(e^{-j(k_{HI} \cdot x + k_{LO} \cdot y)}) &= k_{HI} \cdot \Delta x + k_{LO} \cdot \Delta y \\ \Delta\Theta_{LO}(e^{j(-k_{LO} \cdot x + k_{HI} \cdot y)}) &= k_{LO} \cdot \Delta x - k_{HI} \cdot \Delta y \\ \Delta\hat{x} &= \frac{1}{k_0}(\cos\theta \cdot \Delta\hat{\Theta}_{HI} + \sin\theta \cdot \Delta\hat{\Theta}_{LO}) \\ \Delta\hat{y} &= \frac{1}{k_0}(\sin\theta \cdot \Delta\hat{\Theta}_{HI} - \cos\theta \cdot \Delta\hat{\Theta}_{LO}) \end{aligned} \tag{3.33}$$

Form 3:

$$\begin{aligned} \Delta\Theta_{HI}(e^{j(k_{HI} \cdot x + k_{LO} \cdot y)}) &= -k_{HI} \cdot \Delta x - k_{LO} \cdot \Delta y \\ \Delta\Theta_{LO}(e^{-j(-k_{LO} \cdot x + k_{HI} \cdot y)}) &= -k_{LO} \cdot \Delta x + k_{HI} \cdot \Delta y \\ \Delta\hat{x} &= \frac{1}{k_0}(-\cos\theta \cdot \Delta\hat{\Theta}_{HI} - \sin\theta \cdot \Delta\hat{\Theta}_{LO}) \\ \Delta\hat{y} &= \frac{1}{k_0}(-\sin\theta \cdot \Delta\hat{\Theta}_{HI} + \cos\theta \cdot \Delta\hat{\Theta}_{LO}) \end{aligned} \tag{3.34}$$

Form 4:

$$
\begin{aligned}
\Delta\Theta_{HI}(e^{j(k_{HI}\cdot x+k_{LO}\cdot y)}) &= -k_{HI}\cdot\Delta x - k_{LO}\cdot\Delta y \\
\Delta\Theta_{LO}(e^{j(-k_{LO}\cdot x+k_{HI}\cdot y)}) &= k_{LO}\cdot\Delta x - k_{HI}\cdot\Delta y \\
\Delta\hat{x} &= \frac{1}{k_0}(-\cos\theta\cdot\Delta\hat{\Theta}_{HI}+\sin\theta\cdot\Delta\hat{\Theta}_{LO}) \\
\Delta\hat{y} &= \frac{1}{k_0}(-\sin\theta\cdot\Delta\hat{\Theta}_{HI}-\cos\theta\cdot\Delta\hat{\Theta}_{LO})
\end{aligned}
\tag{3.35}
$$

As described in the previous section, the beam position is calibrated against the fiducial grid prior to exposure. During exposure, the beam position is constantly monitored and corrected. Hence, the beam-position error $(\Delta x, \Delta y)$ and the associated phase error $(\Delta\Theta_{HI}, \Delta\Theta_{LO})$ are always extremely small, which in turn guarantees the best performance of the phase estimator. Since the estimation accuracies of $\Delta\Theta_{HI}$ and $\Delta\Theta_{LO}$ are entirely dependent on γ and N, the variances of $\Delta\hat{x}$ and $\Delta\hat{y}$ are identical. In other words, there is no performance difference in the estimation of the two coordinates. Using (3.33) as an example, the variance of $\Delta\hat{x}$ is simply

$$
\begin{aligned}
\sigma^2_{\Delta\hat{x}} &= \frac{1}{k_0^2}\mathrm{var}\,(\cos\theta\cdot\Delta\hat{\Theta}_{HI}+\sin\theta\cdot\Delta\hat{\Theta}_{LO}) \\
&= \frac{1}{k_0^2}(\cos^2\theta\cdot\mathrm{var}\,(\Delta\hat{\Theta}_{HI})+\sin^2\theta\cdot\mathrm{var}\,(\Delta\hat{\Theta}_{LO})) \\
&= \frac{\sigma^2_{\Delta\hat{\Theta}}}{k_0^2}(\cos^2\theta+\sin^2\theta) \\
&= \frac{\sigma^2_{\Delta\hat{\Theta}}}{k_0^2}\,,
\end{aligned}
\tag{3.36}
$$

where $\sigma^2_{\Delta\hat{\Theta}} = \mathrm{var}\,(\Delta\hat{\Theta}_{HI}) = \mathrm{var}\,(\Delta\hat{\Theta}_{LO})$, $\Delta\hat{\Theta}_{HI}$ and $\Delta\hat{\Theta}_{LO}$ are uncorrelated with each other. Assuming the spatial period of the grid is Λ_G, we have $k_0 = 2\pi/\Lambda_G$ and

$$
\sigma^2_{\Delta\hat{x}} = \left(\frac{\sigma_{\Delta\hat{\Theta}}\,\Lambda_G}{2\pi}\right)^2 . \tag{3.37}
$$

The same result can be obtained for $\Delta\hat{y}$.

3.3 Estimation Accuracy with SE Signal

When the phase estimator is able to achieve its best performance, the equivalent condition in (3.17) is met:

$$\sigma^2_{\Delta\hat{\Theta}} = \frac{1}{\gamma N} \,, \tag{3.38}$$

where γ is the SNR of the reference signal. Equation (3.37) becomes

$$\sigma^2_{\Delta\hat{x}} = \frac{\Lambda_G^2}{4\pi^2\gamma N} \,. \tag{3.39}$$

Suppose the bandwidth of the feedback loop is BW, it must be at least a factor of two greater than the bandwidth of the disturbances to satisfy the Nyquist criteria. In practice, BW is usually set to five times of the Nyquist rate. During exposure, the deflection speed is fixed at R (pixels/s), and the number of samples collected per correction is simply $N = R/BW$, assuming one sample is collected per pixel. Substituting this result into (3.39) yields the lower bound of $\sigma^2_{\Delta\hat{x}}$:

$$\sigma^2_{\Delta\hat{x}} = \frac{\Lambda_G^2\, BW}{4\pi^2\, \gamma R} \,. \tag{3.40}$$

Equation (3.40) indicates that the variance of $\Delta\hat{x}$ can be reduced by increasing the beam-deflection rate, or by decreasing the grid period. For a given EBL tool, the maximum deflection rate is usually limited by the hardware, and any modification on the hardware is simply impractical. The fiducial-grid period can be decreased, but the amount is very limited due to the complexity of the fabrication process. The third parameter that can be exploited is the SNR of the reference signal γ, which will be explored further below.

3.3.1 SNR Calculation of SE Signal

As described in the previous chapter, the SNR of the reference signal is limited by the noise bottleneck. For SE signals, the noise bottleneck is at the SE-generation-detection stage. To achieve a target placement accuracy, the SNR at the noise bot-

tleneck must satisfy

$$\gamma \geq \frac{\Lambda_G^2 \, BW}{4\pi^2 \, \sigma_{\Delta\hat{x}}^2 R} \; . \tag{3.41}$$

By defining

$\bar{n}$ = the average number of electrons deposited at each pixel,

δ_h = SE yield of the high-yield material,

δ_l = SE yield of the low-yield material,

g = fraction of the dose deposited during partial beam blanking,

f_c = the collection efficiency of the SE detector,

the amplitude of the reference signal A and its variance σ^2 can be expressed as

$$\begin{aligned} A &= \frac{1}{2} \, f_c \, g \, \bar{n} \, (\delta_h - \delta_l) \\ \sigma^2 &= f_c \, g \, \bar{n} \, \delta_h \; . \end{aligned} \tag{3.42}$$

The SNR of the reference signal can then be expressed in terms of the parameters of SE generation as

$$\gamma = \frac{f_c \, g \, \bar{n} \, (\delta_h - \delta_l)^2}{8 \, \delta_h} \; , \tag{3.43}$$

where

$$\bar{n} = \frac{\text{exposure dose} \times (\text{step size})^2}{\text{charge of electron}} \; . \tag{3.44}$$

Again, most parameters in (3.43) are determined by either the SEBL tool, or by the lithography process. For example, the collection efficiency is limited by the SE detector, and with an appropriate design, it can reach its theoretical limit of 1 [41]. The number $\bar{n}$ is directly related to the exposure dose of the e-beam resist and the beam step size. The factor g, whose details are given in the next chapter, should have a value no greater than 0.1. The only variable that we have control over is the grid materials, e.g., δ_h and δ_l. Let $a = \delta_l / \delta_h$, it is clear that

$$\gamma \propto (1 - a)^2 \, \delta_h \; , \tag{3.45}$$

which indicates that SNR of the SE signal can be improved by identifying materials with both higher yield (increasing δ_h) and lower yield (decreasing a).

When the Al grid is used, $\delta_h = 0.25$ (Al), $\delta_l = 0.06$ (PMMA), and

$$\frac{(\delta_h - \delta_l)^2}{\delta_h} = 0.144 \; . \tag{3.46}$$

Assuming the exposure parameters given in Table 3.1, the average detection accura-

BW	Λ_G	R	f_c	g	Step size
1 kHz	250 nm	10 MHz	1	0.1	10 nm

Table 3.1: Assumed exposure parameters for the SNR calculation.

cies that can be achieved for various exposure doses are:

$$\begin{aligned} \sigma_{\Delta\hat{x}} &= 4.19\,\text{nm} \quad @ \quad \text{dose} = 0.8\mu C/cm^2 \\ &= 1.33\,\text{nm} \quad @ \quad \text{dose} = 8\mu C/cm^2 \\ &= 0.42\,\text{nm} \quad @ \quad \text{dose} = 80\mu C/cm^2 \text{ (PMMA)} \; . \end{aligned} \tag{3.47}$$

The BW is set to 1 kHz to accommodate disturbances with frequencies up to 100 Hz. The calculation implies that 1 nm-placement accuracy is achievable, but not without problems. There are many factors that can prevent one from achieving the predicted results. For example, a low detector-collection efficiency or a reduced SE yield of the grid material can cause the estimator performance to suffer. A process that requires a much more sensitive resist than PMMA can also create difficulties. On the other hand, improvement in some parameters can make the task easier. For instance, a SEBL tool with a faster deflection rate R, or a better environmental control leading to a smaller BW requirement, will help to reduce $\sigma_{\Delta\hat{x}}$.

3.4 Implementation of Spatial-phase Locking

To evaluate its performance, real-time SPLEBL was implemented on MIT's Raith 150 SEBL system. The Raith 150 is an inexpensive, converted SEM system that combines

a LEO GEMINI column and a Raith ELPHY pattern generator. The GEMINI column has a well-designed in-lens detector, which provides low-noise SE signals. The ELPHY pattern generator is equipped with a 16-bit digital-to-analog converter (DAC), and it is capable of achieving 2 nm minimum step size in a 100 μm field at a maximum deflection speed of 10 MHz. The Raith 150 has a laser-interferometer-controlled stage, and the beam energy is adjustable from 100 eV to 30 keV.

The Raith 150 tool does not have raster-scan and signal processing capabilities required by SPLEBL. Hence, additional hardware must be added. Figure 3-6 shows a simple schematic diagram for SPLEBL. The solid boxes represent the existing hardware, and the dashed boxes represent the added hardware. The position-estimation algorithm is implemented on a high-performance computer, and raster scan is accomplished by controlling the beam blanker with a dedicated computer instead of the ELPHY pattern generator.

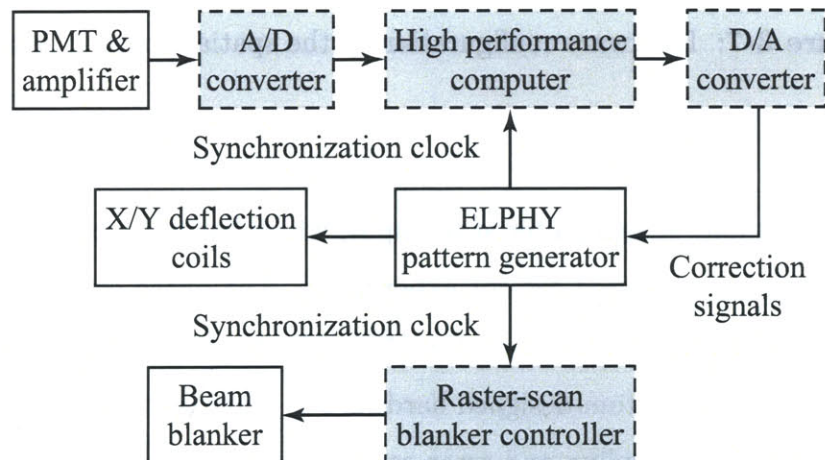

Figure 3-6: Schematic diagram of the control system for real-time SPLEBL. Dashed boxes represent additional hardware required to implement the feedback loop and raster-scan.

The reference-signal sampling and phase estimation are conducted on a Pentium III-based real-time controller (model PXI-8176) in combination with a multi-channel, digital-and-analog I/O board (model PXI-6115) from National Instruments. Figure 3-7 depicts the signal flow in the spatial-phase locking system. The reference signal is routed to a 10 MHz analog-to-digital converter (ADC) on the PXI-6115.

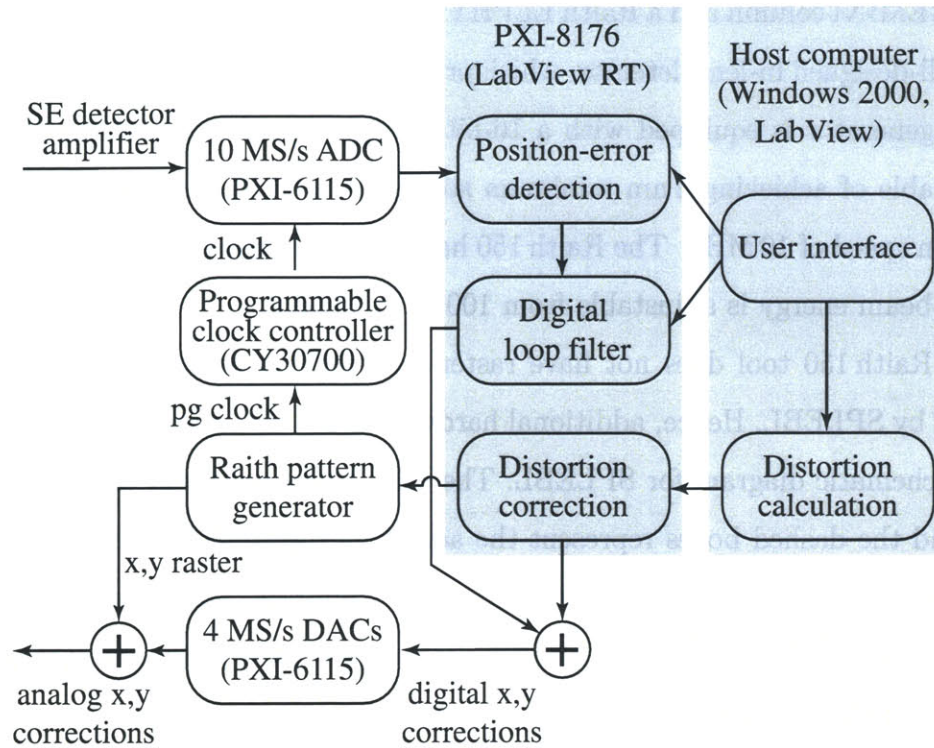

Figure 3-7: Hardware configuration of the spatial-phase locking system.

The ADC has an anti-aliasing filter at its input, which has two settings of 50 kHz and 500 kHz. The latter was used for our experiment. The phase estimation is entirely implemented in software running on the PXI-8176 for fast prototyping. It can be easily transferred to a custom-designed hardware to lower cost and improve speed [8]. For simplicity, signal sampling and error correction are synchronized with beam deflection, which is derived from the pattern-generator clock via a programmable-clock controller. Time-invariant distortions associated with the electron lenses can also be corrected through this system. An example of such a distortion is shown on the right plot of Fig. 3-8. The magnetic deflection system causes a pronounced distortion in the x direction that closely follows a second-order-ramp response. The result is shown in Fig. 3-8. Although this distortion can be precisely measured, its correction is restrained by physical limitations of magnetic devices, and complete elimination is impossible.

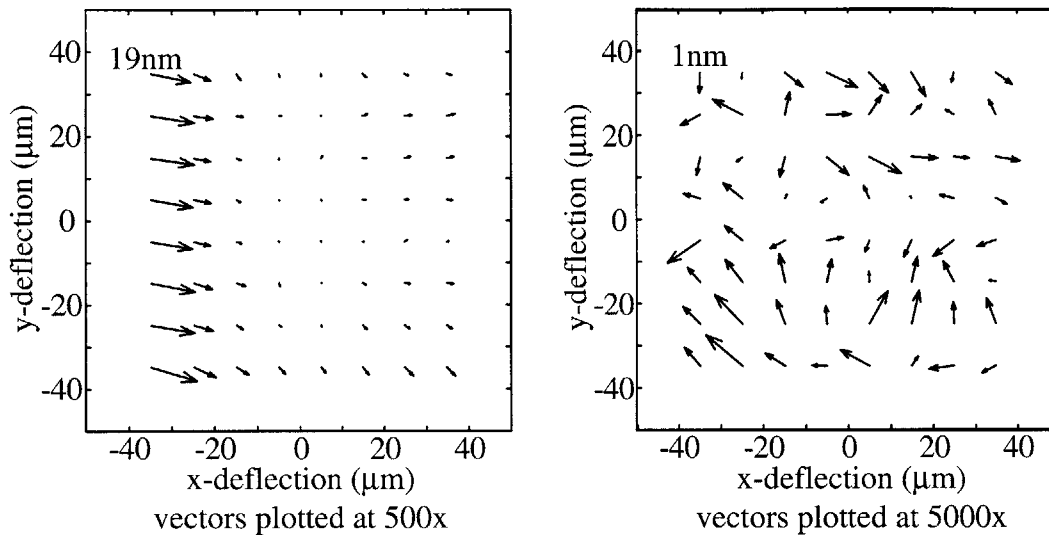

Figure 3-8: Distortions in the electron optics measured by Hastings [26]. Each error vector represents the displacement of the beam position, and is calculated over a 1000 pixel-by-1000 pixel block. The large distortion shown on the left is due to the magnetic deflection system. It closely follows a ramp response for a second-order system. After removing the second-order distortion, a much smaller distortion results as shown on the right. This distortion is caused by the imperfection in the electron lenses, and can be corrected through the deflection system as described above.

For convenience, the step size is set to 9.96235 nm for a field of 10^4 pixels. Because of hardware limitations, the estimation and correction are applied to 1000-pixel blocks instead of every single pixel. This is justified by the low-frequency content of the environmental disturbances. The fiducial grid used was a 246 nm period Al grid rotated by -0.352990 rad with respect to the deflection axis, i.e., the x axis. Details of the grid were provided in the previous chapter. The negative rotation introduced is due to a practical issue that the electron beam moves from top to bottom in y. In other words, the beam progresses along the negative y direction. This issue is solved by introducing a rotation of $-\theta$ to the grid while using θ in the calculation. The parameters above are chosen to obtain integer number of periods for k_{HI} and k_{LO} over 1000 pixels, and to simplify the estimation algorithm. Custom software was written to calibrate and align the stitching field to the grid.

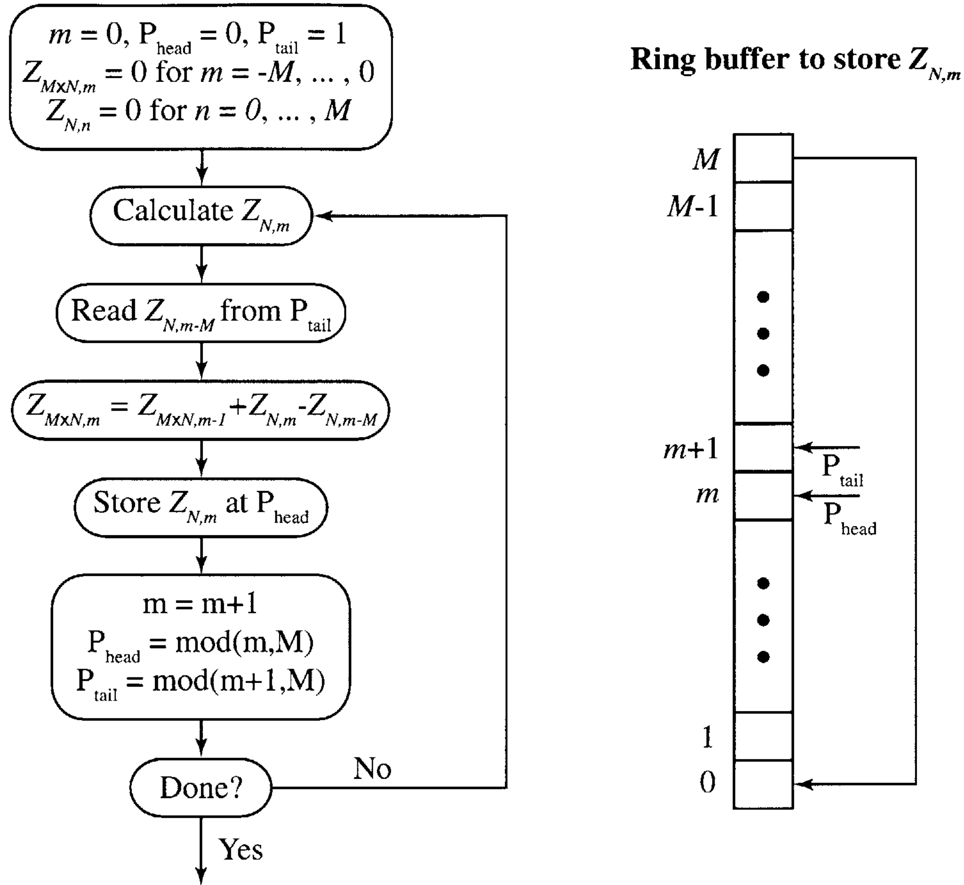

Figure 3-9: An estimator implementation based on an M number of N-pixel blocks. The periodogram of the mth block $Z_{N,m}$ is calculated according to (3.9). The total peridogram $Z_{M\times N,m}$ is computed by summing $Z_{N,m-M}$ to $Z_{N,m}$. A ring buffer is used to store periodograms for blocks $m - M$ to m.

The number of samples for each calculation is $N = 1000$, which is not sufficient to achieve high placement accuracy. In the original implementation, a user-defined loop filter was added after the phase estimator to reduce estimation errors. Although this method worked in this experiment, it did not take advantage of the full potential of the estimator. The estimator is nonlinear, and combining a nonlinear system with a linear loop filter may produce undesirable and unpredictable errors. For the estimator to achieve optimal performance, one should strictly follow (3.9). Figure 3-9 illustrates a method of calculating $Z_{M\times N}(e^{j\omega_0})$ over M continuous N-pixel blocks. In each N-pixel block, $Z_N(e^{j\omega_0})$ is computed according to (3.9). This method will be

implemented in the future.

3.4.1 Experimental Results

A field-stitching experiment was conducted by Hastings to evaluate the performance of the above-described system [26]. A set of 200-nm-period gratings as depicted

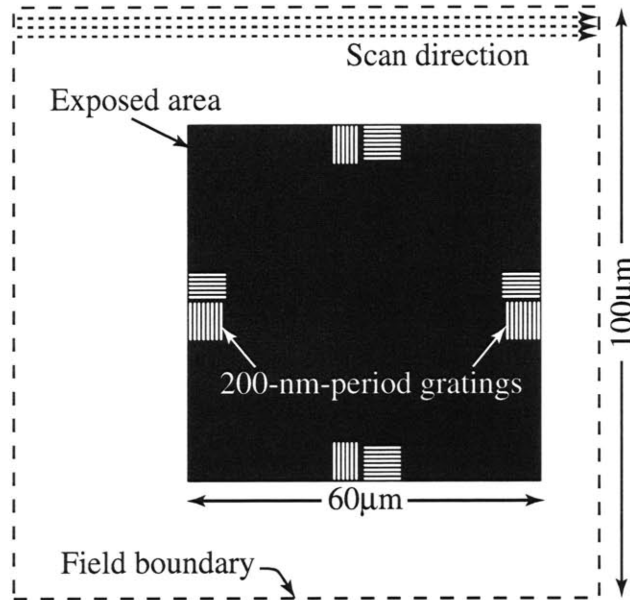

Figure 3-10: Exposing patterns for field-stitching test [26]. The black area represents exposed area. To avoid distortions caused by the deflection system, only the center 60 μm area is used.

in Fig. 3-10 are exposed over the center 60 μm area of each 100 μm field. Since a flexible dose modulation scheme is not currently implemented, the beam is turned on most of the time to facilitate continuous feedback, and it was only turned off over the grating area. As shown in Fig. 3-11, the same grating pattern was repeated over 49 fields, and the stitching error was evaluated at each boundary of adjacent fields. The measurement results are given in Fig. 3-12.

The measurements were conducted at horizontal and vertical boundaries for both x and y directions. The standard deviations are $\sim$1 nm. More details of exposure conditions and post-exposure processes are given in [26].

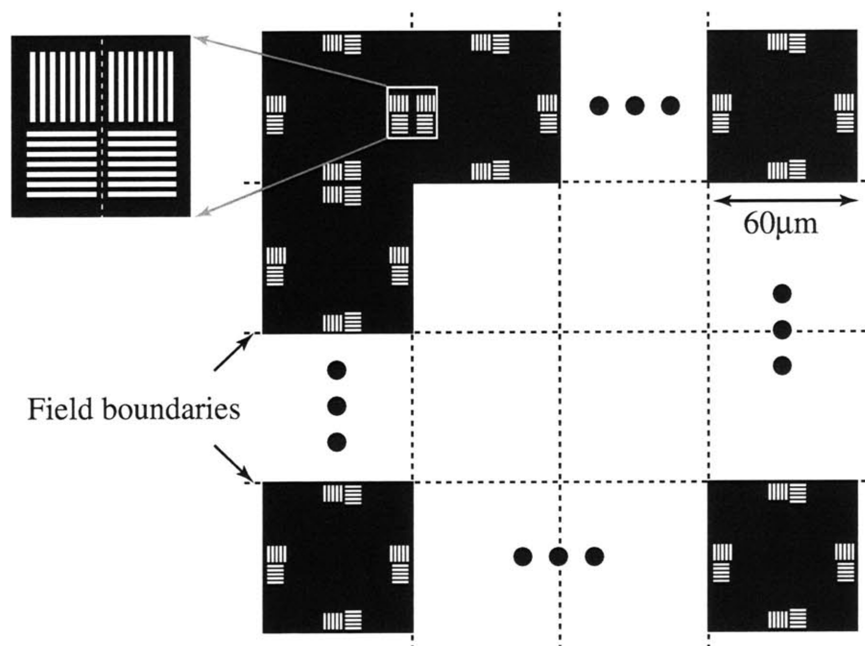

Figure 3-11: Exposing layout for field-stitching test. A matrix of 7-by-7 fields are exposed next to one another. The stitching errors are measured at each boundary of adjacent fields.

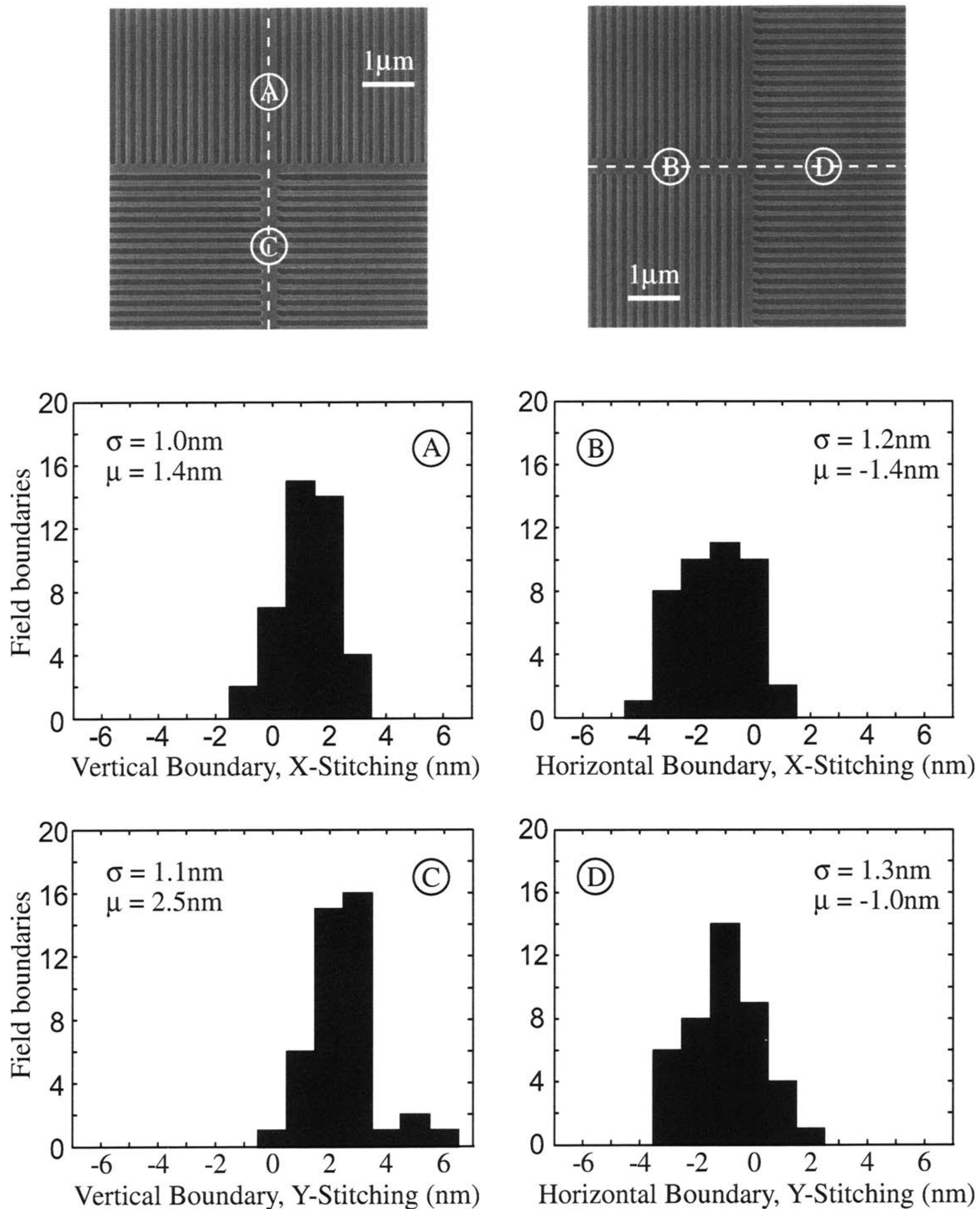

Figure 3-12: Stitching error measurements for real-time SPLEBL [26]. The measurements are conducted at horizontal and vertical boundaries, for both x and y directions. The corresponding location of each plot is indicated in the SEM shown on the top. The mean and standard deviation is listed in each plot.

Chapter 4

Partial Beam Blanker

As discussed in Chapter 3, the position-detection algorithm requires a large number of samples for an accurate phase estimation, and these samples must be equally spaced and continuous. Any disruption in the sampling, such as that experienced in a vector-scan system when the beam moves from one pattern to the next, will cause great difficulties for the estimator to make accurate beam-position calculations. Furthermore, a continuous reference signal will provide a continuous feedback, which can maximize the bandwidth of the system, and optimize the dynamic performance of SPLEBL. To achieve continuous sampling during normal exposure, a raster-scan-writing strategy should be adopted, and a dose-modulation scheme must be developed such that the number of electrons deposited over non-patterned areas is substantially less than that over pattern area, yet enough to generate the reference signal for beam-position detection. Ideally, the dose should be reduced by a factor of 10 or more. A device that can accomplish dose modulation is called a partial-beam blanker, because it stops some of the e-beam from reaching the sample.

4.1 Conventional E-beam Blanker

Conventional SEBL systems use a beam blanker to turn the e-beam on and off. An e-beam blanker can be either electrostatic or magnetic. Although a magnetic beam-blanker causes less beam distortion, SEBL systems almost exclusively use electrostatic

blanker for their high-speed operations. As depicted in Fig. 4-1, the simplest and most commonly used blanker design consists of a pair of metal plates and a beam stop. The

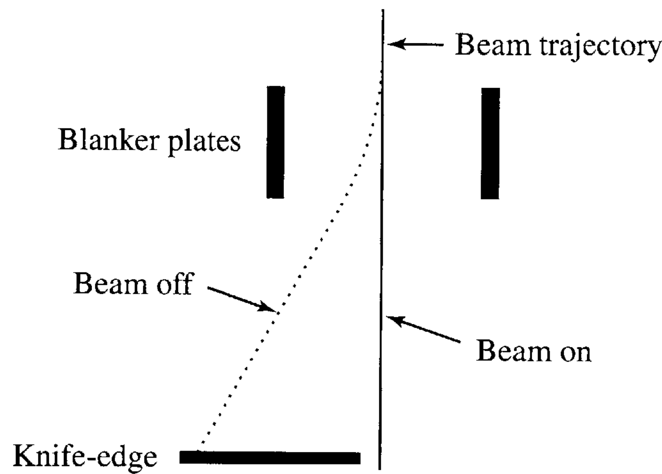

Figure 4-1: Conventional beam blanker design for SEBL consists of a pair of metal plates and a beam stop. During beam blanking, an electrostatic potential is applied to the metal plates, and the induced field between the plates pushes the beam off the axis so that it is blocked by the beam stop.

beam stop can be either a knife-edge or an aperture. When the beam is blanked, a differential voltage applied across the metal plates accelerates the beam in the lateral direction, causing it to hit the beam stop. The beam stop is usually located at one of the intermediate beam cross-overs for high-speed operations, which allows the edge of the beam stop to be placed close to the beam path, and facilitates a blanking voltage to be relatively low. Such a low blanking voltage is advantageous for high-speed operations.

This on-off-blanking scheme presents a problem for SPLEBL. When the beam scans over non-exposed areas, it is turned off completely, and the reference signal will not be available for the position-estimation algorithm. Since patterns to be exposed can be arbitrary, sometimes very sparse, the intermittent absence of the reference signal can hinder the accuracy of the position-estimation algorithm. Furthermore, the on-off transitions of the blanker introduce a time-dependent beam motion, i.e., spurious deflection at the sample, and it introduces additional errors in position de-

tection.

4.2 Partial-beam-blanking via Time Modulation

Traditionally, dose modulation has been implemented on SEBL tools to perform gray-level exposure. It is accomplished by varying the width of the blanking pulse [9]. Similarly, this method can be used to achieve partial-beam blanking. For example, turning the beam on for 10% of the time will effectively reduce the deposited dose by 90%. This scheme, however, requires an extremely fast beam blanker, i.e., ten times faster than the deflection speed. Several problems associated with fast beam blanking are beam jitter, i.e., spurious deflection [43, 51], transmission-line ringing, and eddy-current effects [22, 21] during blanking-signal transition.

Spurious deflection is caused by two transient phenomena. One is the rising and trailing edges of the blanker signal, and the other is the finite amount of time for the electrons to pass the blanker plates. During transitions of the blanker signal, the field created across the blanker plates will move the beam off axis, but not enough to push the beam completely over the beam stop. Part of the beam will reach the substrate with a little shift. Even if the transition happens instantaneously, the second transitional phenomenon will take place. Immediately after the blanker is on, the electrons travelling at the lower portion of the blanker will gain less speed in the lateral direction than those at the upper portion. The lower portion electrons will therefore miss the beam stop and reach the substrate. Besides spurious deflection, ringing and eddy-currents are common problems for this type of device, and they become much more pronounced at higher operating speed.

These problems cause undesired beam motion at the substrate, which result not only in greater line-edge roughness and poorer CD uniformity, but more importantly, have an adverse effect on the accuracy of beam-position detection. Figure 4-2 illustrates a double-deflection-blanker design that can reduce the impact of the transient effects. This design was first investigated by Guo et al. [43] via numerical simulations. They found that by replacing a single parallel-plate deflector with a double-deflection

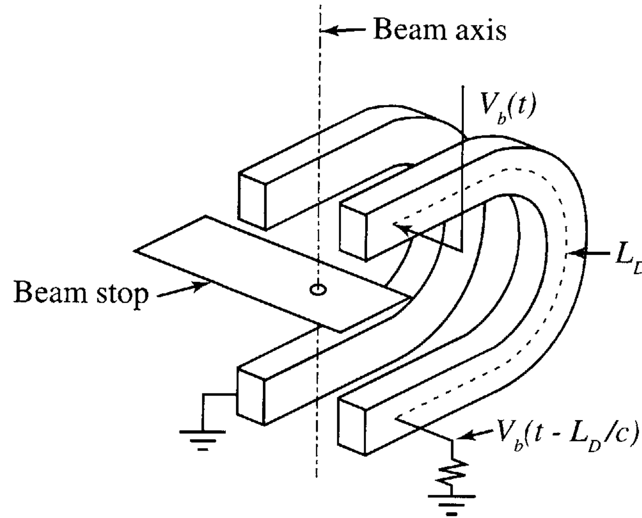

Figure 4-2: Double-deflection blanker used to reduce spurious deflection. The blanking signal $V_b(t)$ enters the upper blanker plate. The horseshoe-shaped blanker body introduces a delay of L_D/c when the blanking signal reaches the lower plate. (L_D is the length of the delay line, and c is the speed of light.) The amplitude of the spurious deflection is controlled by varying the length of the delay, usually a fraction of 1 ns.

blanker placed in tandem, and introducing a delay in the blanking signal to the lower blanker, the spurious deflection could be significantly reduced. Later, Paik et al. derived an analytical approximation [51] from their own numerical results [52]. As pointed out by Paik, the magnitude of the beam jitter was greatly affected by the delay. Precise control of the delay was however extremely difficult because it was usually a fraction of 1 ns. Finally, Gesley et al. came up with the design depicted in Fig. 4-2, which used a transmission line to precisely control the delay [22, 21]. As can be seen in [21], spurious deflection can be reduced, but not completely eliminated.

4.3 Partial-beam-blanking via Beam Shift

Controlling beam current is an alternative to controlling blanking signals for achieving dose modulation. Figure 4-3 illustrates an intuitive method that uses four pairs of blanker plates, and two apertures to achieve current modulation. During partial-

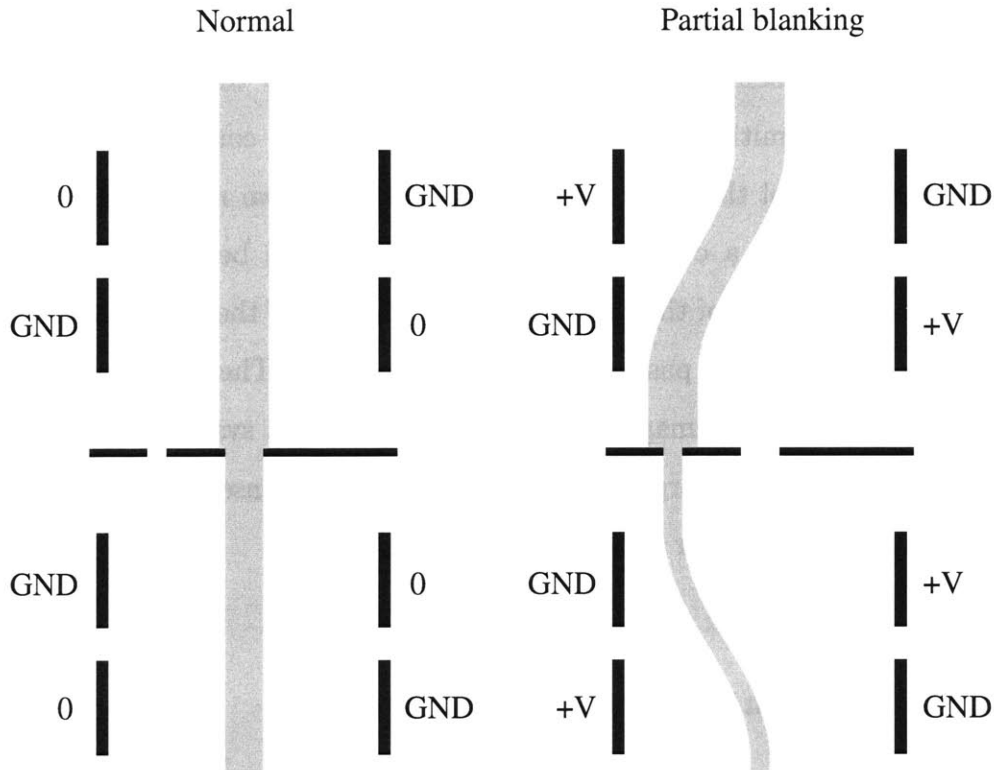

Figure 4-3: Quadruple-deflection partial-beam blanker uses four pairs of blanker plates and two apertures to achieve current modulation. During partial-beam blanking, the beam is shifted to the smaller aperture by the upper two deflectors. The lower two deflectors are used to shift the beam back.

beam blanking, the beam is shifted over to the smaller aperture by the upper two deflectors. It is then shifted back to the center axis by the lower two deflectors. As for the regular blankers, this partial-beam-blanker design also suffers from spurious deflection. However, since this blanker can operate at a much lower speed than the one introduced in the previous section, spurious deflection is much less of a problem.

The alignment between the returning beam and the axis must be very precise to minimize beam displacement during partial-beam blanking. This imposes a very tight tolerance on the physical dimensions of the deflectors, especially the size of the blanker plates and the gaps between the deflectors. The partial-beam blanker must be calibrated before exposure to ensure accurate alignment.

4.4 Partial-beam-blanking via Beam Expansion

Another method to achieve current modulation is to vary the size or shape of the beam at a current-limiting aperture. Figure 4-4 depicts a common scheme used by SEBL tools to control the beam current. It consists of two rotationally symmetric or "round" lenses and a current-limiting aperture placed between the two lenses. Altering the focal length of the top lens changes the size of the beam at the aperture and the amount of current passing through the aperture. The lower lens is adjusted accordingly to satisfy the imaging condition of the overall system [9]. Because this scheme requires switching large current or voltage to the lenses, it is not suitable for high-speed applications such as SPLEBL.

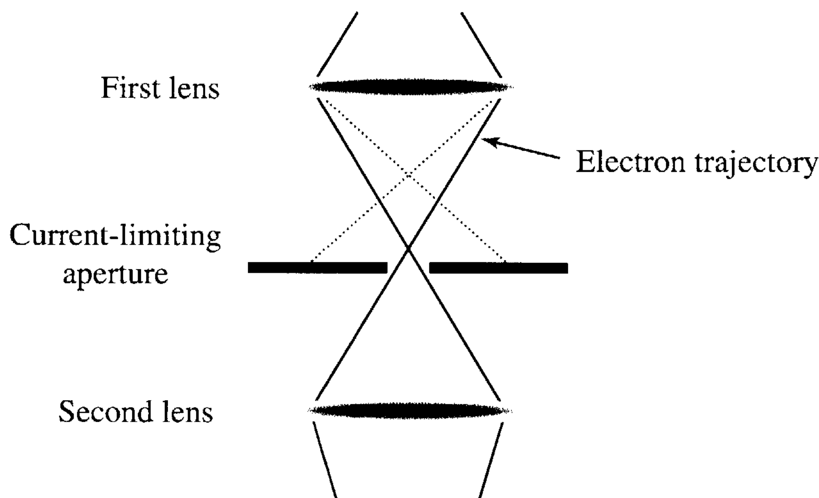

Figure 4-4: Beam current modulation via round lens. The current passing through the current-limiting aperture is determined by the focal length of the first lens, and the second lens is used to set the correct imaging condition.

For high-speed dose modulation, we have investigated a partial-beam-blanker which consists of a conventional rotationally-symmetric lens, a quadrupole lens and a current-limiting aperture. Because the quadrupole lens has a much stronger focusing ability than conventional round lenses, the operating voltage can be reduced to a practical level. Magnetic quadrupole lenses would not be compatible with high speed, and they will not be considered. This design has several desirable features. Firstly,

the center of mass of the beam does not shift during partial-beam blanking. Hence, spurious deflection is completely avoided, transmission-line ringing is no longer an issue, and no pre-exposure alignment is required. Secondly, the operating voltage can be very low, and a high modulation rate readily achieved. Thirdly, a typical SEBL tool has several beam crossovers to achieve demagnification and high-speed beam blanking; therefore, incorporating this device into existing column design should be fairly straightforward.

4.4.1 Electrostatic Quadrupole Lens

Multipole lenses play a unique and important role in charged-particle optics. They are usually used as stigmators to correct certain types of aberration associated with round lenses. At accelerating voltages exceeding a few hundred kilovolts where rotational symmetric lenses are considered "too weak", quadrupole lenses are often used as focusing devices.

As shown in Fig. 4-5(a), an electrostatic quadrupole lens consists of four electrodes. The electric potentials on adjacent electrodes are equal and opposite. Figure 4-5(c) plots the electrical field distribution for a quadrupole lens in the $x-y$ plane. When a collimated round beam travels through the quadrupole lens along the $z-$axis, it will be compressed in the x direction and stretched in the y direction, forming a line image at the focal plane of the lens. To better understand the focusing properties of the quadrupole lens, the paraxial equations are derived below.

The equations of motion for an electron in an electrostatic field is governed by Newton's second law

$$\frac{d\boldsymbol{g}}{dt} = \frac{d}{dt}(m\boldsymbol{v}) = Q\boldsymbol{E}(\boldsymbol{r}, t) \ , \tag{4.1}$$

with Q being the charge, $\boldsymbol{E}$ the electrical field, $\boldsymbol{v}$ the velocity of the electron, $\boldsymbol{r}$ the position, and $\boldsymbol{g}$ the *kinetic* momentum. The time-domain solution of this equation can be solved, but it is very inconvenient for deducing the properties of the quadrupole

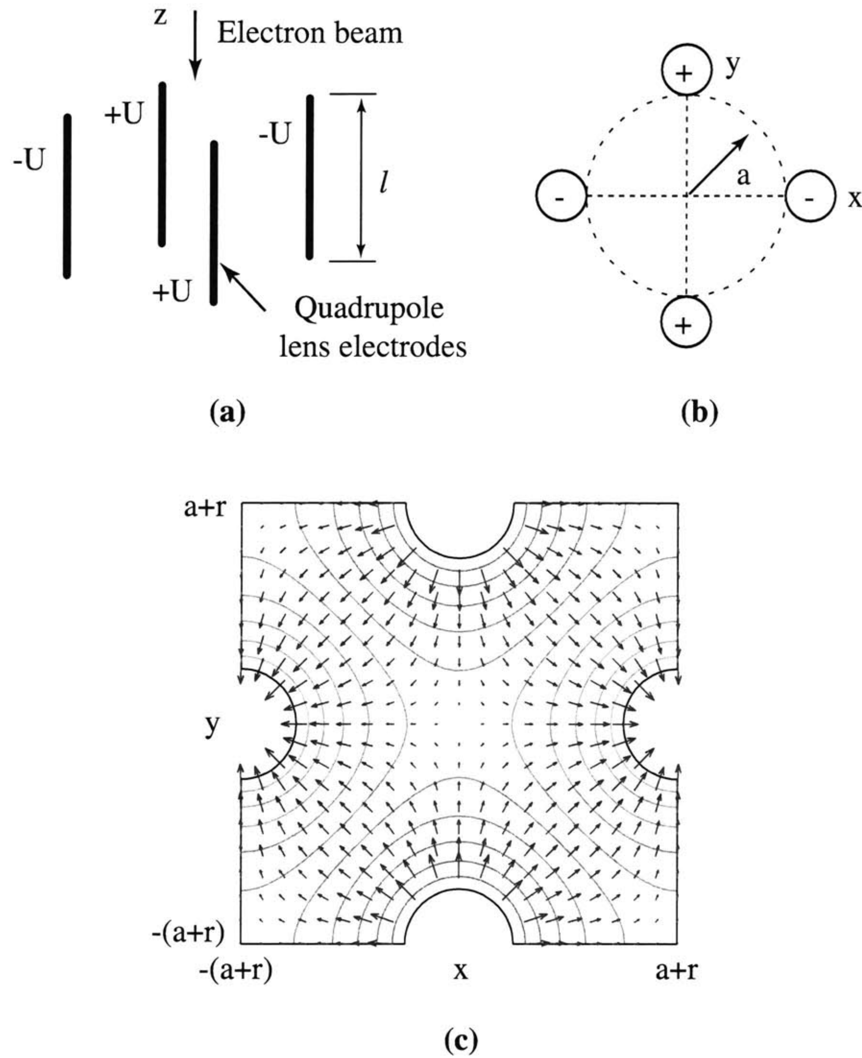

Figure 4-5: (a) 3-D structure of an electrostatic quadrupole lens. The length of the electrodes is l, and the mid-point of the lens is defined as $z = 0$. (b) The dimensions of the lens in the $x-y$ plane. (c) The electric field distribution of the quadrupole lens in the $x-y$ plane.

lens. Instead, we will provide the trajectory equations in the space domain, z [30]:

$$\begin{aligned} x'' &\equiv \frac{d^2x}{dz^2} = \frac{\varrho^2}{2\hat{\Phi}}\left(\frac{\partial\hat{\Phi}}{\partial x} - x'\frac{\partial\hat{\Phi}}{\partial z}\right) \\ y'' &\equiv \frac{d^2y}{dz^2} = \frac{\varrho^2}{2\hat{\Phi}}\left(\frac{\partial\hat{\Phi}}{\partial y} - y'\frac{\partial\hat{\Phi}}{\partial z}\right) \ , \end{aligned} \tag{4.2}$$

where $x' = \frac{dx}{dz}$, $y' = \frac{dy}{dz}$, ϱ denotes $\sqrt{1 + x'^2 + y'^2}$, and $(x(z), y(z))$ are the Cartesian

coordinates of the electron at z. The function $\hat{\Phi}$ is called the acceleration potential, and it is defined as

$$\hat{\Phi} = \Phi(1 + \epsilon\,\Phi) \tag{4.3}$$

where $\Phi(x, y, z)$ is the potential distribution of the electrostatic field, and

$$\epsilon = \frac{e}{2m_0c^2} \tag{4.4}$$

with $-e$ being the charge of the electron and m_0 its rest mass. Following the convention, the surface of the cathode is chosen to be zero potential. (Please refer to Appendix B for a detailed derivation.)

Although the electric potential Φ can be obtained by numerically solving the corresponding Poisson's equation with appropriate boundary conditions, there is in general no closed-form solution for (4.2). Fortunately, a paraxial approximation of the solution exists and will suffice to provide the focusing properties of the quadrupole lens. The paraxial approximation is further justified by the fact that most of the electrons travel close to the z axis.

For electrostatic devices, the electric potential Φ can be expressed as a series expansion of the axial potential $\phi(z) = \Phi(0, 0, z)$

$$\begin{aligned}\Phi(x, y, z) = {} & \phi - \frac{1}{4}(x^2 + y^2)\phi'' + \frac{1}{64}(x^2 + y^2)^2\phi^{(iv)} \\ & - xp_1(z) - yq_1(z) + \frac{1}{8}(x^2 + y^2)(xp_1'' + yq_1'') \\ & + \frac{1}{2}(x^2 - y^2)p_2(z) + xyq_2(z) \\ & - \frac{1}{24}(x^4 - y^4)p_2'' - \frac{1}{12}(x^3y + xy^3)q_2'' + \cdots\end{aligned} \tag{4.5}$$

in which $p_1(z)$, $q_1(z)$, $p_2(z)$ and $q_2(z)$ are all functions of z. Among them, $p_1(z)$ and $q_1(z)$ are the transverse components, and they are zero inside of the quadrupole lens. It is common practice to place the electrodes of the quadrupole along the x and y axes, so that $q_2(z) = 0$. Furthermore, because there is no rotational symmetry in the quadruple lens, the $(x^2 + y^2)$ term should also be zero, which forces $\phi'' = \phi^{(iv)} = 0$.

After applying these conditions to (4.5) and only keeping first- and second-order terms for the paraxial approximation, we obtain

$$\Phi(x, y, z) \approx \phi + \frac{1}{2}(x^2 - y^2)p_2(z) \ . \tag{4.6}$$

Finally, we substitute (4.6) into (4.2) and neglecting all quadratic terms in x, y, and their derivatives, we find

$$\begin{aligned}
\frac{\partial \hat{\Phi}}{\partial x} &= (1 + 2\epsilon\phi)\frac{\partial \Phi}{\partial x} = \gamma p_2 x \\
\frac{\partial \hat{\Phi}}{\partial y} &= (1 + 2\epsilon\phi)\frac{\partial \Phi}{\partial y} = -\gamma p_2 y \\
\frac{\partial \hat{\Phi}}{\partial z} &= (1 + 2\epsilon\phi)\frac{\partial \Phi}{\partial z} = \gamma \phi' \ ,
\end{aligned}$$

and

$$\begin{aligned}
\frac{1 + x'^2 + y'^2}{2\hat{\Phi}}\left(\frac{\partial \hat{\Phi}}{\partial x} - x'\frac{\partial \hat{\Phi}}{\partial z}\right) &\approx \frac{\gamma}{2\hat{\phi}}(p_2 x - x'\phi') \\
\frac{1 + x'^2 + y'^2}{2\hat{\Phi}}\left(\frac{\partial \hat{\Phi}}{\partial y} - y'\frac{\partial \hat{\Phi}}{\partial z}\right) &\approx -\frac{\gamma}{2\hat{\phi}}(p_2 y + y'\phi') \ ,
\end{aligned}$$

where $\gamma = 1 + 2\epsilon\phi$ and $\hat{\phi} = \phi(1 + \epsilon\phi)$. The paraxial ray equations take the form [31]

$$\begin{aligned}
x'' - \frac{\gamma}{2\hat{\phi}}(p_2 x - x'\phi') &= 0 \\
y'' + \frac{\gamma}{2\hat{\phi}}(p_2 y + y'\phi') &= 0
\end{aligned} \tag{4.7}$$

With the trajectory equations in (4.7), we can develop a set of transfer matrices to describe the imaging properties of the quadrupole lens. The position (x_1, y_1) and the trajectory angle (x'_1, y'_1) of an electron in the image space of the quadrupole can be related to those in the object space by the pair of transfer matrices:

$$\begin{aligned}
\begin{pmatrix} x_2 \\ x'_2 \end{pmatrix} &= T_x \begin{pmatrix} x_1 \\ x'_1 \end{pmatrix} \\
\begin{pmatrix} y_2 \\ y'_2 \end{pmatrix} &= T_y \begin{pmatrix} y_1 \\ y'_1 \end{pmatrix}
\end{aligned} \tag{4.8}$$

where the transfer matrices can be expressed as

$$\begin{aligned} T_x &= \begin{pmatrix} -(z_2 - z_{Fi}^{(x)})/f_{xi} & (z_2 - z_{Fi}^{(x)})(z_1 - z_{Fo}^{(x)})/f_{xi} + f_{xo} \\ -1/f_{xi} & (z_1 - z_{Fo}^{(x)})/f_{xi} \end{pmatrix} \\ T_y &= \begin{pmatrix} -(z_2 - z_{Fi}^{(y)})/f_{yi} & (z_2 - z_{Fi}^{(y)})(z_1 - z_{Fo}^{(y)})/f_{yi} + f_{yo} \\ -1/f_{yi} & (z_1 - z_{Fo}^{(y)})/f_{yi} \end{pmatrix} \end{aligned} \tag{4.9}$$

with $z_{Fi}^{(x)}, z_{Fo}^{(x)}, f_{xi}, f_{xo}$ and $z_{Fi}^{(y)}, z_{Fo}^{(y)}, f_{yi}, f_{yo}$ being the cardinal elements in the $x-z$ and $y-z$ plane, i.e., focal position and focal length, respectively. When the imaging conditions are satisfied, i.e., $(T_x)_{12} = 0$, a point source on the object plane $z = z_{xo}$ will form a line image on its conjugate image plane $z = z_{xi}$, which agrees with our intuition. In general, multiplets of quadrupole lenses are used to form stigmatic images. The Russian quadruplet, introduced by the Leningrad group led by S. Ya. Yavor, is the most commonly used design [16, 44].

Figure 4-6 demonstrates how to use the quadrupole lens to achieve current modulation. Suppose that the quadrupole is initially inactive, i.e., all electrodes are at equal potential as shown in Fig. 4-6(a), and the beam is focused to a spot at the current-limiting aperture by some focusing element not shown in the figure. When the quadrupole is excited, the beam crossover in the $x-z$ plane will move up due to the compressive force, and that in the $y-z$ plane will move down due to the stretching force, as shown in Fig. 4-6(b) and (c). With the appropriate excitation conditions, the beam will form, at the current-limiting aperture, a barrel-shaped square that is much larger than the original spot, and the beam current will decrease proportionally to the increase of the area.

For an electrostatic quadrupole with long rod-shaped electrodes, the electric field can be modelled as a rectangular function, and closed form solutions are readily available for (4.7). Figure 4-5 defines the physical and electrical properties of the

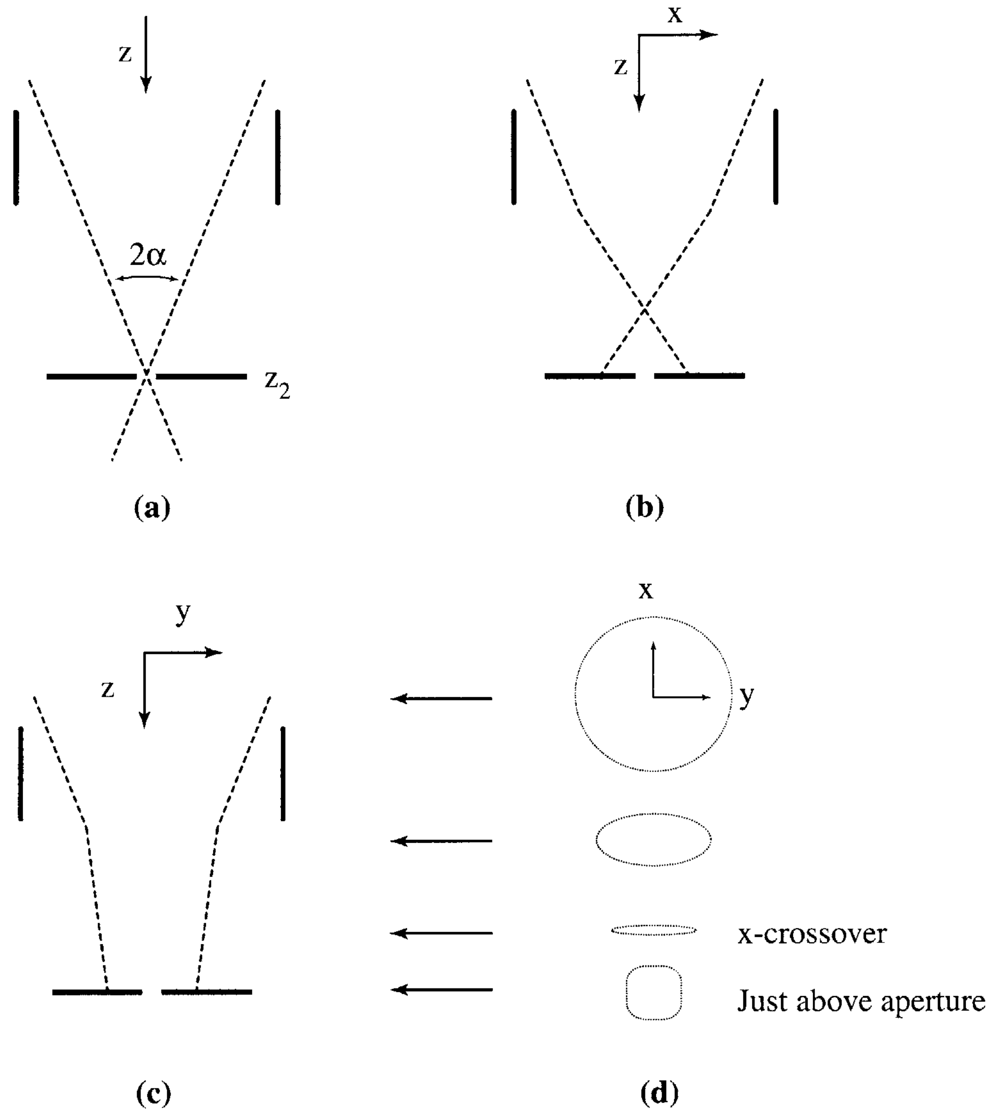

Figure 4-6: **(a)** The beam is focused at the current-limiting aperture. The quadrupole is inactive. **(b)** The beam crossover moves up in the $x-z$ plane when the quadrupole is excited. **(c)** The beam crossover moves down in the $y-z$ plane when the quadrupole is excited. **(d)** Cross-sectional views of the beam at various places along z.

quadrupole. To satisfy the boundary condition,

$$p_2(z) = -\frac{2U}{a^2}q \tag{4.10}$$

where $-U$ is the potential on the x electrodes with respect to the axial potential, a is the distance between the optical axis and the electrodes, and q is defined as

$$q = \begin{cases} 1 & |z| < L/2 \\ 0 & |z| > L/2 \end{cases} \tag{4.11}$$

with L being the effective length of the quadrupole. It is related to the physical length of the electrode l and a by $L = l + 1.1a$. With this setup, it is conceivable that $\phi' = 0$.

Letting

$$\beta^2 = \frac{\gamma U}{a^2 \hat{\phi}} \tag{4.12}$$

solutions to (4.7) can be expressed in terms of $\sin(\beta z)$, $\cos(\beta z)$, $\sinh(\beta z)$ and $\cosh(\beta z)$. Defining

$$\theta := \beta L \tag{4.13}$$

the cardinal elements are given by

$$\begin{aligned} z_{Fx} &:= z_{Fi}^{(x)} = -z_{Fo}^{(x)} = \left(\frac{\cot\theta}{\theta} + \frac{1}{2}\right) L \\ z_{Fy} &:= z_{Fi}^{(y)} = -z_{Fo}^{(y)} = \left(-\frac{\coth\theta}{\theta} + \frac{1}{2}\right) L \\ f_x &:= f_{xi} = f_{xo} = \frac{L}{\theta \sin\theta} \\ f_y &:= f_{yi} = f_{xo} = \frac{L}{\theta \sinh\theta} \end{aligned} \tag{4.14}$$

The transfer matrices defined in (4.9) can then be expressed as functions of the design parameters of the quadrupole. As shown in the above equation, the variable z_{Fx} can have multiple values if $\theta > \pi/2$, which corresponds to multiple beam crossovers inside the quadrupole lens. For simplicity and reasons discussed in the following section, we set $0 < \theta < \pi/2$. This condition implies that there will be no beam crossover inside the quadrupole, and $z_{Fx} > L/2$.

Suppose that the convergence angle at the current-limiting aperture is 2α (Fig. 4-6), we can set $z_1 = -z_{Fx}$ and calculate (x_2, y_2) at the aperture located at z_2 through

$$x_2 = -(z_2 - z_{Fx})x_1/f_x + f_x x_1' \tag{4.15}$$

$$y_2 = -(z_2 - z_{Fy})y_1/f_y + ((z_2 - z_{Fy})(-z_{Fx} + z_{Fy})/f_y + f_y)y_1' \tag{4.16}$$

with $x_1' = y_1' = \tan(\alpha)$ and $x_1 = y_1 = (z_{Fx} + z_2)\tan(\alpha)$.

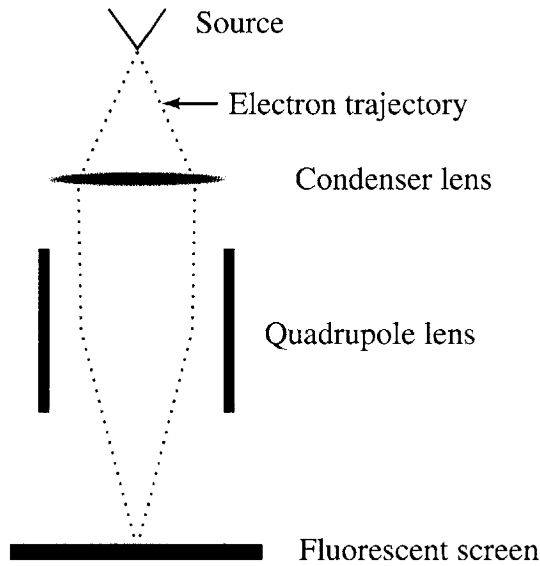

Figure 4-7: Partial-beam blanker test setup for the results in Fig. 4-8. It uses a tungsten hairpin tip, an electrostatic condenser lens designed by Rempfer [57], and an electrostatic quadrupole lens formed by four 40 mm long metal rods. The fluorescent screen is made of a 75 mm quartz wafer coated with a thin layer of ZnS powder.

Figure 4-8 shows fluorescent images of a 5 keV e-beam through a quadrupole-lens-based partial-beam blanker. The test setup is given in Fig. 4-7. The upper-left image shows a beam finely focused by the condenser lens when the quadrupole lens is inactive. The images (a) to (e) illustrate the effect of the quadrupole lens when its operating voltage is increased. The two focal planes are a result of combining the quadrupole lens with the condenser lens as described in Fig. 4-6. Ideally, the partial-beam blanker should be designed so that the beam forms a symmetric image at the current-limiting aperture, as shown in Fig. 4-8(c), when the blanker is active.

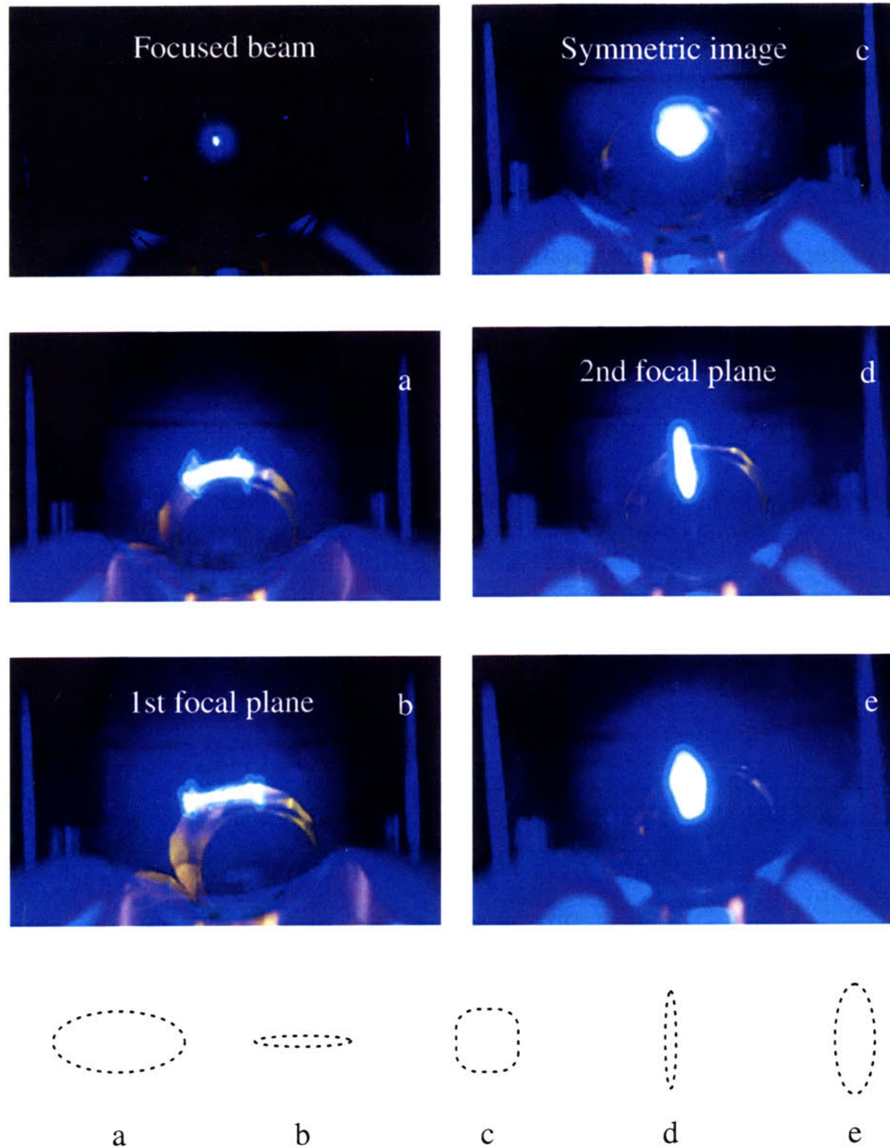

Figure 4-8: Fluorescent images of an e-beam through a quadrupole-lens-based partial-beam blanker. The upper-left image shows a focused beam when the partial-beam blanker is off. The diameter of the focused beam is about 1 mm. The images from (a) to (e) illustrate the effect of the quadrupole lens when the voltage on its electrodes is increased. Ideally, the current-limiting aperture would be placed at the location where the symmetric image is obtained.

4.4.2 Design Procedure and Considerations

The design parameters to be optimized, based on a given set of system configurations, are l, a, U and z_2. The set of system configurations includes the axial potential ϕ, where $e\phi$ is the beam energy, the convergence angle at the current-limiting aperture α, and the magnified beam size (x_2, y_2). Since there are more unknowns than equations, a set of solutions will be available, and we can select an optimal solution based on additional criteria, such as minimizing the driving voltage, or minimizing the electrode length. Because the equations needed to solve for the design parameters are rather complex, it is more convenient to solve for z_2 and y_2 based on l, a, U and a fixed x_2, and then to find the set of values of l, a and U that provide the desired y_2.

Figures 4-9(a) and (b) plot solutions for z_2 and y_2 based on the following conditions:

$$\phi = 100\,\text{kV}$$
$$\alpha = 2\,\text{mrad}$$
$$a = 1\,\text{mm}$$
$$x_2 = -120\,\mu\text{m}$$
$$20\,\text{mm} \leq l \leq 80\,\text{mm}$$
$$4\,\text{V} \leq U \leq 26\,\text{V}$$

with the assumption that the radius of the aperture hole is $40\,\mu$m, and the beam is magnified by three in the x direction. As we can see from the plots, we sometimes have to trade one parameter for another. For example, if we want to match y_2 to x_2, or minimize the driving voltage U, we will have to place the quadrupole further away from the aperture, which may require increasing the overall length of the optical column.

Since the quadrupole lens will change the size of the beam at the beam crossover, its effect on the probe size should be carefully evaluated. In this design, the current-limiting aperture is located at a beam crossover, and the aperture opening is no

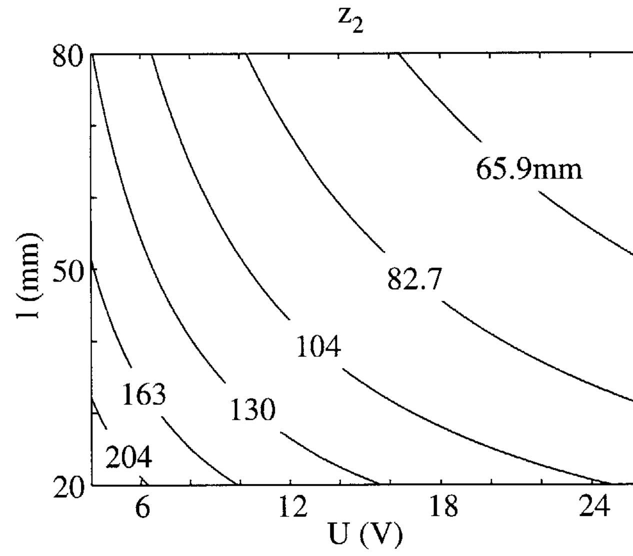

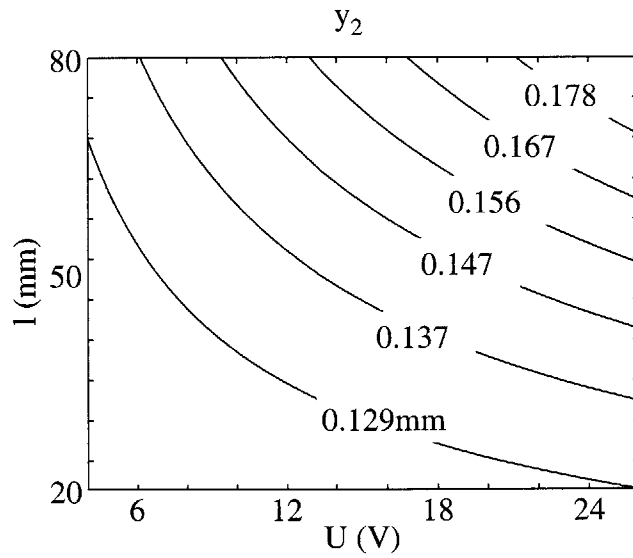

Figure 4-9: Plots for solutions of **(a)** z_2 and **(b)** y_2 against design parameters l and U.

larger than the size of the crossover, hence the probe formed at the substrate can be considered the image of the aperture. In this case, the probe size will depend on two factors: the size of the aperture and the maximum convergence angle α_{max} for the electrons passing through the aperture. When the crossover gets "magnified" by the quadrupole lens, α_{max} reduces a little in the y direction. The same argument would be true in the x direction if there is no beam crossover inside of the quadrupole lens or $\theta < \pi/2$. Since we only allow θ to take values in the range $(0, \pi/2)$, the condition is satisfied. Therefore, the probe size will not increase. However, the depth of focus will suffer from the action of the quadrupole lens. With the same reasoning, we can argue that the magnifications in the x and y directions do not have to match perfectly. The mismatch will influence the electron density distribution along those two directions, but as long as the mismatch is not significant, it will not effect the exposure. Even if the aperture is larger than the beam crossover, it should not impose much limitation on the application of this partial-beam-blanker design in SPLEBL, because as long as the final probe size is less than half of the fiducial-grid period of 250 nm, the beam-position detection should not be affected much. For example, if the normal probe size is 5 nm, and the current-limiting aperture is twice that of the beam crossover, the probe size will be, in the worst case scenario, 10 nm during partial-beam blanking, and that is still significantly less than the fiducial-grid period.

Because the angular magnifications are, in general, different for the x and y direction, the shape of the beam will no longer be circularly symmetric. Careful numerical analysis and 3-D simulation should be conducted for the actual design because design parameters of other parts of the column also play a vital role. In addition, multiplets may be introduced to have a better control the angular magnifications.

Chapter 5

Conclusion

This thesis described our approach to implementing real-time SPLEBL on an SEBL system. The implementation is divided into three major components, the global-fiducial-reference grid, the beam-position detection algorithm, and the partial-beam blanker.

As an absolute reference for beam-position locking, the quality of the fiducial grid, in terms of SNR and long-range-spatial coherence, directly determines the performance of SPLEBL. The SE signal was chosen to serve as the reference signal due to its high-generation efficiency, high-spatial resolution, and well-established detector design. The complexity of the fabrication process for the SE grid, however, becomes a major technical challenge. A non-perturbative, user-friendly process based-on IL was developed for fabricating Cu grids. This process is fairly simple and straightforward, and it is suitable for average users. Some improvements are required to optimize this process and further simplify it. For example, an optimized evaporation process can provide stress-free Cu films, and eliminate the use of the SiO layer and the HF etch.

IL provides an effective method of producing gratings with long-range spatial-coherence over large areas. There are, however, several issues in using conventional IL for grid fabrication: the hyperbolic-phase progression generated by interfering two spherical beams; the requirement of double exposures with extremely tight angular alignment to pattern grids; the time-consuming setup process. Several lithographic techniques based on masks/templates, such as NFIL, AIL and NIS are much better

suited for this task. The masks and templates can be patterned by SBIL to ensure long-range-spatial coherence. These process need to be further evaluated and optimized.

To further increase the SNR of the reference signal, and improve the dynamic performance and detection accuracy of SPLEBL, new grid materials with both very high and very low SE yields are under investigation. SWCNT and C_{60} fullerenes are among the high-yield materials, and TCNQ is among the low-yield materials. New grid materials must be compatible with EBL process, and not complicate the grid-fabrication process.

The beam-position-detection algorithm was fully developed, and ~1 nm placement accuracy was demonstrated experimentally. Because of the nonlinearity of the algorithm, implementing the algorithm in a sub-optimized way may severely hinder its detection accuracy. Further improvement can be made in the current software implementation to improve the detection accuracy and the dynamic performance of the system. Compared with the software implementation, a dedicated hardware implementation of the algorithm can accommodate faster beam deflection, provide more frequent corrections, and thereby improve the dynamic performance of SPLEBL.

A new type of beam blanker was developed for achieving partial-beam blanking. This partial-beam blanker uses an electrostatic quadrupole lens to vary the size and shape of the beam at the current-limiting aperture. Since it does not move the center of the beam during blanking, spurious deflection and beam jitter are completely eliminated. Furthermore, with a careful design, this partial-beam blanker can operate at a very low voltage, and is suitable for high-speed systems.

The implementation of the partial-beam blanker in a commercial SEBL tool requires a redesign of the electron-optical column. Hence, experimental verification of the blanker design was conducted on a simple test column. The result agrees well with the theory.

As minimum-feature size is approaching that of the molecules, nanometer-level-placement accuracy becomes more important than ever for scientists and engineers in nanotechnology. SPLEBL is currently the only technology that is able to achieve

such a level of placement accuracy. Furthermore, being a closed-loop system, SPLEBL can help to relax the requirements on environmental control, and significantly reduce the cost of EBL systems. We sincerely hope that, with the help of the industry, this technology can be made available for the scientific community and the industry, which will greatly benefit the general public.

Appendix A

The Phase and the Periodogram of a Sinusoidal Signal

The Fourier transform pair of a discrete-time signal is defined as [50]

$$X(e^{j\omega}) = \sum_{n=-\infty}^{\infty} x[n]e^{-j\omega n} \ , \tag{A.1}$$

$$x[n] = \frac{1}{2\pi} \int_{-\pi}^{\pi} X(e^{j\omega})e^{j\omega n}\, d\omega \ . \tag{A.2}$$

A discrete-time signal of limited duration can be modelled as $y[n] = x[n] \cdot h[n]$, where $x[n]$ can be an infinite sequence, and $h[n]$ is a rectangular windowing function

$$h[n] = \begin{cases} 1, & 0 \leq n \leq N-1 \\ 0, & \text{otherwise} \end{cases} \tag{A.3}$$

The Fourier transform of the product $x[n] \cdot h[n]$ is given by

$$\mathscr{F}\{x[n] \cdot h[n]\} = X \otimes H(e^{j\omega}) = \frac{1}{2\pi} \int_{-\pi}^{\pi} X(e^{j\theta})H(e^{j(\omega-\theta)})\, d\theta \ . \tag{A.4}$$

The Fourier transform of the windowing function $h[n]$ is simply

$$H(e^{j\omega}) = \frac{\sin(\omega N/2)}{\sin(\omega/2)}\ e^{-j\omega(N-1)/2} \ . \tag{A.5}$$

Supposing $x[n]$ is a sinusoidal function $\cos(\omega_0 n + \Theta)$, as in the case of the phase estimator introduced in Chapter 3. Its Fourier transform is

$$X(e^{j\omega}) = \pi e^{j\Theta} \sum_{r=-\infty}^{\infty} \delta(\omega - \omega_0 + 2\pi r) + \delta(\omega + \omega_0 + 2\pi r) \ . \tag{A.6}$$

The right-hand side of (A.4) becomes

$$\begin{aligned} X \otimes H(e^{j\omega}) =& \frac{e^{j\Theta}}{2} \sum_{r=-\infty}^{\infty} \frac{\sin((\omega - \omega_0 + 2\pi r)N/2)}{\sin((\omega - \omega_0 + 2\pi r)/2)} \, e^{-j(\omega-\omega_0+2\pi r)(N-1)/2} \\ &+ \frac{\sin((\omega + \omega_0 + 2\pi r)N/2)}{\sin((\omega + \omega_0 + 2\pi r)/2)} \, e^{-j(\omega+\omega_0+2\pi r)(N-1)/2} \end{aligned} \tag{A.7}$$

Letting $\omega = \omega_0$, $N \gg 0$, and $r = 0$, we obtain

$$\frac{\sin((\omega + \omega_0)N/2)}{\sin((\omega + \omega_0)/2)} \approx 0 \ , \tag{A.8}$$

because $2\omega_0 \gg 0$. Then,

$$X \otimes H(e^{j\omega_0}) = \frac{e^{j\Theta}}{2} \, N \ . \tag{A.9}$$

Finally, the periodogram of $x[n]$ can be defined as

$$X_N(e^{j\omega}) = \frac{1}{\sqrt{N}} \, X \otimes H(e^{j\omega}) = \frac{\sqrt{N}}{2} \, e^{j\Theta} \ , \tag{A.10}$$

and the phase Θ can be calculated by

$$\Theta = \tan^{-1} \left(\frac{\mathrm{Im}\{X_N(e^{j\omega_0})\}}{\mathrm{Re}\{X_N(e^{j\omega_0})\}} \right) \ . \tag{A.11}$$

Similar result can be obtained by letting $\omega = -\omega_0$:

$$\Theta = -\tan^{-1} \left(\frac{\mathrm{Im}\{X_N(e^{-j\omega_0})\}}{\mathrm{Re}\{X_N(e^{-j\omega_0})\}} \right) \ . \tag{A.12}$$

Appendix B

Trajectory Equations for Electrons

The motion of charged particles in an electromagnetic field is governed by the Lorentz equation

$$\frac{d\boldsymbol{g}}{dt} = \frac{d}{dt}(m\boldsymbol{v}) = Q\left\{\boldsymbol{E}(\boldsymbol{r},t) + \boldsymbol{v}\times\boldsymbol{B}(\boldsymbol{r},t)\right\} \ , \tag{B.1}$$

in which $\boldsymbol{v} = d\boldsymbol{r}/dt$ represents the velocity, and $\boldsymbol{g} = m\boldsymbol{v}$ the *kinetic* momentum. (Boldface letters are used to distinguish vectors from scalars.) For electrons, $Q = -e$. To include relativistic corrections in the derivation, we define

$$\begin{aligned} \beta &:= \frac{|\boldsymbol{v}|}{c} = \frac{v}{c} \\ \gamma &:= \frac{1}{\sqrt{1-\beta^2}} \ , \end{aligned} \tag{B.2}$$

where c is the speed of light. The relativistic mass is simply

$$m = \frac{m_0}{\sqrt{1-\beta^2}} = \gamma m_0 \ . \tag{B.3}$$

To derive the characteristics of the electrostatic quadrupole lens, we are only interested in the steady-state solutions. Therefore, we can let $\boldsymbol{E}(\boldsymbol{r},t) = \boldsymbol{E}(\boldsymbol{r})$ and $\boldsymbol{B}(\boldsymbol{r},t) = 0$.

Both electric and magnetic fields are conservative fields for charged particles, and the total energy can be expressed as the sum of the kinetic energy $T(v) = m_0c^2(\gamma-1)$

and potential energy $V(\boldsymbol{r}) = Q\Phi(\boldsymbol{r})$

$$E_0 = m_0c^2(\gamma - 1) + Q\Phi(\boldsymbol{r}) = constant \ . \tag{B.4}$$

The electrostatic potential $\Phi(\boldsymbol{r})$ is defined as

$$\boldsymbol{E}(\boldsymbol{r}) = -\nabla\Phi(\boldsymbol{r}) \ , \tag{B.5}$$

and it is uniquely determined by the boundary conditions at the surfaces of the electrodes. Since the reference point of the potential can be set arbitrarily, we choose $\Phi(\boldsymbol{r}) = 0$ at the cathode surface, where the kinetic energy of the electrons is also zero. Hence, the total energy $E_0 = 0$, and

$$T(\boldsymbol{r}) = -Q(\boldsymbol{r}) \ . \tag{B.6}$$

In Einstein's theory of Special Relativity, the energy of the electrons can be expressed in terms of kinetic momentum $g = |\boldsymbol{g}|$ as

$$mc^2 = \sqrt{(m_0c)^2 + g^2c^2} = m_0c^2 + T \ . \tag{B.7}$$

Solve for g:

$$\begin{aligned} g &= \sqrt{2m_0T\left(1 + \frac{T}{2m_0c^2}\right)} \\ &= \sqrt{2m_0e\Phi(\boldsymbol{r})\left(1 + \frac{e\Phi(\boldsymbol{r})}{2m_0c^2}\right)} \ . \end{aligned} \tag{B.8}$$

To simplify this expression, we define

$$\begin{aligned} \epsilon &:= \frac{e}{2m_0c^2} \\ \eta &:= \sqrt{\frac{e}{2m_0}} \\ \hat{\Phi}(\boldsymbol{r}) &:= \Phi(\boldsymbol{r})\{1 + \epsilon\Phi(\boldsymbol{r})\} \ . \end{aligned} \tag{B.9}$$

Substitute into (B.8)

$$g = \sqrt{2m_0 e\hat{\Phi}} \ . \tag{B.10}$$

The dilatation factor γ and the speed can also be expressed in terms of $\hat{\Phi}$

$$\begin{aligned} \gamma &= \frac{T}{m_0 c^2} + 1 = \sqrt{1 + 4\epsilon\hat{\Phi}} = 1 + 2\epsilon\Phi(\boldsymbol{r}) \\ v &= \frac{g}{m_0 \gamma} = 2\eta\sqrt{\frac{\hat{\Phi}}{1 + 4\epsilon\hat{\Phi}}} \ . \end{aligned} \tag{B.11}$$

The gradients of $\hat{\Phi}$ and Φ are related by

$$\nabla\hat{\Phi} = (1 + 2\epsilon\Phi)\nabla\Phi \ . \tag{B.12}$$

Finally, the electrostatic field

$$\boldsymbol{E} = -\frac{1}{\gamma}\nabla\hat{\Phi} = -(1 + 4\epsilon\hat{\Phi})^{-\frac{1}{2}} \ \nabla\hat{\Phi} = -\frac{v}{e}\nabla g \ . \tag{B.13}$$

In practical calculations, trajectory equations expressed in time domain $\boldsymbol{r} = \boldsymbol{r}(t)$ are not very convenient and useful, especially for developing a theory of focusing and aberrations for various elements. For this application, the Cartesian representation as functions of z, i.e. $x = x(z)$ and $y = y(z)$, becomes extremely valuable.

By defining the differential arc-length $ds := |d\boldsymbol{r}| = v\,dt$, the differential operator $d/dt = v\,d/ds$, and Equation (B.1), without the magnetic term, can be rewritten as

$$\frac{d\boldsymbol{g}}{ds} = -e\frac{\boldsymbol{E}}{v} = \nabla g(\boldsymbol{r}) \ . \tag{B.14}$$

Since

$$\frac{d\boldsymbol{g}}{ds} = \frac{d}{ds}\left(m\frac{d\boldsymbol{r}}{dt}\right) = \frac{d}{ds}\left(mv\frac{d\boldsymbol{r}}{ds}\right) = \frac{d}{ds}\left(g(\boldsymbol{r})\frac{d\boldsymbol{r}}{ds}\right) \ , \tag{B.15}$$

we have

$$\frac{d}{ds}\left(g(\boldsymbol{r})\frac{d\boldsymbol{r}}{ds}\right) = \nabla g(\boldsymbol{r}) \ . \tag{B.16}$$

Now, we define the derivative with respect to z as $x' = dx/dz$ and $y' = dy/dz$,

and

$$\varrho := \sqrt{1 + x'^2 + y'^2} \ , \tag{B.17}$$

the differential operator d/ds becomes

$$\frac{d}{ds} = \frac{dz}{ds}\frac{d}{dz} = \frac{1}{\varrho}\frac{d}{dz} \ . \tag{B.18}$$

Substituting this into (B.16) gives

$$\frac{d}{ds}\left(g(\boldsymbol{r})\frac{d\boldsymbol{r}}{ds}\right) = \frac{1}{\varrho}\frac{d}{dz}\left(\frac{g}{\varrho}\frac{d\boldsymbol{r}}{dz}\right) \ . \tag{B.19}$$

Expanding the right-hand side yields

$$\frac{g}{\varrho^2}\boldsymbol{r}'' + \frac{\boldsymbol{r}'}{\varrho}\frac{d}{dz}\left(\frac{g}{\varrho}\right) = \nabla g \ . \tag{B.20}$$

In the Cartesian coordinate system,

$$\boldsymbol{r} = x\boldsymbol{i}_x + y\boldsymbol{i}_y + z\boldsymbol{i}_z \ .$$

Hence, the vector equation in (B.20) corresponds to three scalar equations with the $\boldsymbol{i}_z$ equation

$$\frac{1}{\varrho}\frac{d}{dz}\left(\frac{g}{\varrho}\right) = \frac{\partial g}{\partial z} \tag{B.21}$$

being dependent on the $\boldsymbol{i}_x$ and $\boldsymbol{i}_y$ equations. By substituting this equation into the $\boldsymbol{i}_x$ and $\boldsymbol{i}_y$ equations, we can obtain

$$\begin{aligned} x'' &= \frac{\varrho^2}{g}\left(\frac{\partial g}{\partial x} - x'\frac{\partial g}{\partial z}\right) \\ y'' &= \frac{\varrho^2}{g}\left(\frac{\partial g}{\partial y} - y'\frac{\partial g}{\partial z}\right) \ . \end{aligned} \tag{B.22}$$

Since

$$\begin{aligned}
g &= \sqrt{2m_0 e\hat{\Phi}} \\
\frac{\partial g}{\partial x} &= (2m_0 e\hat{\Phi})^{-\frac{1}{2}} m_0 e \frac{\partial \hat{\Phi}}{\partial x} \\
\frac{\partial g}{\partial y} &= (2m_0 e\hat{\Phi})^{-\frac{1}{2}} m_0 e \frac{\partial \hat{\Phi}}{\partial y} \\
\frac{\partial g}{\partial z} &= (2m_0 e\hat{\Phi})^{-\frac{1}{2}} m_0 e \frac{\partial \hat{\Phi}}{\partial z} \ ,
\end{aligned} \tag{B.23}$$

Equation (B.22) becomes

$$\begin{aligned}
x'' &= \frac{\varrho^2}{2\hat{\Phi}} \left(\frac{\partial \hat{\Phi}}{\partial x} - x' \frac{\partial \hat{\Phi}}{\partial z} \right) \\
y'' &= \frac{\varrho^2}{2\hat{\Phi}} \left(\frac{\partial \hat{\Phi}}{\partial y} - y' \frac{\partial \hat{\Phi}}{\partial z} \right) \ .
\end{aligned} \tag{B.24}$$

Bibliography

[1] International technology roadmap for semiconductors, 2004. `http://public.itrs.net`.

[2] T. Bailey, B. Smith, B. J. Choi, M. Colburn, M. Meissl, S. V. Sreenivasan, J. G. Ekerdt, and C. G. Willson. Step and flash imprint lithography: Defect analysis. *J. Vac. Sci. Technol. B*, 19(6):2806–2810, 2001.

[3] M. berger and S. Seltzer. Tables of energy-losses and ranges of electrons and positrons. In U. Fano, editor, *Penetration of charged Particles in Matter*, National Academy of Sciences-Natinal Research Council Publication 1133, pages 205–227, Washington, D.C., 1964.

[4] S. D. Berger, J. M. Gibson, R. M. Camarda, R. C. Farrow, H. A. Huggins, J. S. Kraus, and J. A. Liddle. Projection electron-beam lithography: A new approach. *J. Vac. Sci. Technol. B*, 9(6):2996–2999, 1991.

[5] H. Boersch and K. H. Hamisch, H. and; Löffler. Electron optical preparation of self-supporting microgrids. *Die Naturwissenschaften*, 46(21):596, 1959.

[6] I. Bojko, N. Hilleret, and C. Scheuerlein. Influence of air exposures and thermal treatments on the secondary electron yield of copper. *J. Vac. Sci. Technol. A*, 18(3):972–979, 2000.

[7] D. A. Buck and K. R. Shoulders. An approach to microminiature printed systems. In *Proceedings of the Eastern Joint Computer Conference*, pages 55–59, Philadelphia, P.A., December 1958. American Institute of Electrical Engineers.

[8] C. Caramana. Pattern-placement-error detection for spatial-phase-locked e-beam lithography (splebl). Master's thesis, Massachusetts Institute of Technology, June 2004.

[9] J. M. Chabala, D. Cole, H. Pearce-Percy, W. Phillips, M. Lu, S. Weaver, D. Alexander, T. Coleman, C. Sauer, and F. Abboud. Lithography and CD performance of advanced MEBES® mask pattern generators. *Proceedings-of-the-SPIE-The-International-Society-for-Optical-Engineering*, 3996:200–215, 2000.

[10] G. C. Chen, P. T. Konkola, R. K. Heilmann, C. Joo, and M. L. Schattenburg. Nanometer-accurate grating fabrication with scanning beam interference lithography. *Proceedings-of-the-SPIE-The-International-Society-for-Optical-Engineering*, 4936:126–134, 2002.

[11] Gang Chen. *Beam Alignment and Image Metrology for Scanning Beam Interference Lithography – Fabrication Gratings with Nanometer Phase Accuracy.* PhD thesis, Massachusetts Institute of Technology, June 2003.

[12] S. Y. Chou, P. R. Krauss, and P. J. Renstrom. Nanoimprint lithography. *J. Vac. Sci. Technol. B*, 14(6):4129–4133, 1996.

[13] M. Colburn, S. C. Johnson, M. D. Stewart, S. Damle, T. C. Bailey, B. Choi, M. Wedlake, T. B. Michaelson, S. V. Sreenivasan, J. G. Ekerdt, and C. G. Willson. Step and flash imprint lithography: a new approach to high-resolution patterning. *Proceedings-of-the-SPIE-The-International-Society-for-Optical-Engineering*, 3676:379–389, 1999.

[14] R. S. Dhaliwal, W. A. Enichen, S. D. Golladay, M. S. Gordon, R. A. Kendall, J. E. Lieberman, H. C. Pfeiffer, D. J. Pinckney, C. F. Robinson, J. D. Rockrohr, W. Stickel, and E. V. Tressler. PREVAIL – electron projection technology approach for next-generation lithography. *IBM journal of research and development*, 45(5):615–638, 2001.

[15] Z. J. Ding, H. M. Li, X. D. Tang, and R. Shimizu. Monte Carlo simulation of absolute secondary electron yield of Cu. *Applied Physics A*, 78(4):585–587, 2004.

[16] A. D. Dymnikov, T. Ya. Fishkova, and S. Ya. Yavor. Spherical aberration of compound quadrupole lenses and systems. *Nuclear Instruments and Methods*, 370(2):268–275, 1965.

[17] H. Farhang, E. Napchan, and B. H. Blott. Electron bachscattering and secondary electron emission from carbon targets: comparison of experimental results with Monte Carlo simulations. *Journal of Physics D: Applied Physics*, 26(12):2266–2271, 1993.

[18] J. Ferrera, M. L. Schattenburg, and H. I. Smith. Analysis of distortion in interferometric lithography. *J. Vac. Sci. Technol. B*, 14(6):4009–4013, 1996.

[19] Juan Ferrera. *Nanometer-Scale Placement in Electron-Beam Lithography.* PhD thesis, Massachusetts Institute of Technology, June 2000.

[20] M. A. Finlayson. Scintillator for spatial-phase-locked e-beam lithography. Master's thesis, Massachusetts Institute of Technology, June 2001.

[21] M. Gesley, D. Colby, F. Raymond, D. McClure, and F. Abboud. Electrodynamic of fast beam blankers. *J. Vac. Sci. Technol. B*, 11(6):2378–2385, 1993.

[22] M. Gesley and P. Condran. Electron beam blanker optics. *J. Vac. Sci. Technol. B*, 8(6):1666–1672, 1993.

[23] J. Goldstein, D. Newbury, D. Joy, C. Lyman, P. Echlin, E. Lifshin, L. Sawyer, and J. Michael. *Scanning Electron Microscope and X-Ray Microanalysis.* Kluwer Academic/Plenum Publishers, New York, N.Y., 3rd edition, 2003.

[24] A. D. Grishina, M. G. Tedoradze, and A. V. Vannikov. Polymer light-sensitive layers for photochemical etching of Al films. *Journal of Photochemistry and Photobiology A*, 92(3):223–228, 1995.

[25] J. G. Hartley, T. R. Groves, H. I. Smith, M. K. Mondol, J. G. Goodberlet, M. L. Schattenburg, J. Ferrera, and A. Bernshteyn. Spatial-phase locking with shaped-beam lithography. *Review of Scientific Instruments*, 74(3):1377–1379, March 2003.

[26] J. T. Hastings. *Nanometer-Precision Electron-Beam Lithography with Applications in Integrated Optics.* PhD thesis, Massachusetts Institute of Technology, June 2003.

[27] J. T. Hastings, M. H. Lim, J. G. Goodberlet, and H. I. Smith. Optical waveguides with apodized sidewall gratings via spatial-phase-locked electron-beam lithography. *J. Vac. Sci. Technol. B*, 20(6):2753–2757, 2002.

[28] J. T. Hastings, F. Zhang, M. A. Finlayson, J. G. Goodberlet, and H. I. Smith. Two-dimensional spatial-phase-locked electron-beam lithography via sparse sampling. *J. Vac. Sci. Technol. B*, 18(6):3268–3271, 2000.

[29] J. T. Hastings, F. Zhang, and H. I. Smith. Nanometer-level stitching in raster-scanning electron-beam lithography using spatial-phase locking. *J. Vac. Sci. Technol. B*, 21(6):2650–2656, 2003.

[30] P. W. Hawkes and E. Kasper. *Priciples of Electron Optics Volume 1: Basic Geometrical Optics.* Academic Press, London ; San Diego, 1996.

[31] P. W. Hawkes and E. Kasper. *Priciples of Electron Optics Volume 2: Applied Geometrical Optics.* Academic Press, London ; San Diego, 1996.

[32] R. J. Hawryluk, A. M. Hawryluk, and H. I. Smith. Energy dissipation in a thin polymer film by electron beam scattering. *Journal of Applied Physics*, 45(6):2551–2566, 1974.

[33] M. B. Heritage. Electron-projection microfabrication system. *J. Vac. Sci. Technol.*, 12:1135–1140, 1975.

[34] N. Hilleret, C. Scheuerlein, and M. Taborelli. The secondary-electron yield of air-exposed metal surfaces. *Applied Physics A*, 76(7):1085–1091, 2003.

[35] P. D. Hooper, M. I. Newton, G. McHale, and M. R. Willis. Electrical properties of nickel phthalocyanine (NiPc) sandwich devices incorporating a tetracyanoquinodimethane (TCNQ) layer. *Semiconductor Science and Technology*, 12(4):455–459, 1997.

[36] D. C. Joy, M. S. Prasad, and H. M. Meyer. Experimental secondary electron spectra under SEM conditions. *Journal of Microscopy*, 215(1):77–85, 2004.

[37] David C. Joy. A database of electron-solid interactions, 2001. `http://web.utk.edu/~srcutk/database.doc`.

[38] K. Kanaya and S. Okayama. Penetration and energy-loss theory of electrons in solid targets. *Journal of Physics D: Applied Physics*, 5(1):43–58, 1972.

[39] H. N. G. King. Eletron beam lithography. *Microelectronics*, pages 28–30, November 1967.

[40] K. Kojima, A. Maeda, and M. Ieda. Electrical conduction and electroluminescence of vacuum-evaporated thin TCNQ films. *IEEE Transactions on Electrical Insulation*, 27(3):629–635, 1992.

[41] V. Kolarik and J. Mejzlik. A design of a new axially symmetric secondary electron detector for the transmission electron microscope. *Meas. Sci. Technol.*, 1(5):391–395, 1990.

[42] P. Konkola. *Scanning Beam Interference Lithography.* PhD thesis, Massachusetts Institute of Technology, 2003.

[43] H. Kuo, J. Foster, W. Haase, J. Kelly, and B. M. Oliver. A high speed blanker for a 300 MHz lithography system. In R. Bakish, editor, *Proceedings of the Electron and Ion Beam Science and Technology: 10th International Conference, Montreal*, volume 83-2, page 78, Princeton, NJ, 1983. Electrochemical Society.

[44] G. J. F. Legge. Proton and nuclear microprobe developments. *Nuclear Instrument and Methods in Physics Research*, 197(1):243–253, 1982.

[45] J. Miller and G. Brandes. Effects of dopant concentration, crystallographic orientation, and crystal morphology on secondary electron from diamond. *Journal of Applied Physics*, 82(9):4538–4545, 1997.

[46] G. Möllenstedt and R. Speidel. Elektonenoptischer mikroschreiber unter elektronenmikroskopischer arbeitskontrolle. *Physikalische blätter*, 16:192, 1960.

[47] R. D. Moore, G. A. Caccoma, H. C. Pfeiffer, E. V. Weber, and O. C. Woodard. EL-3: a high throughput, high resolution e-beam lithography tool. *J. Vac. Sci. Technol.*, 19(4):950–952, 1981.

[48] K. Murooka, K. Hattori, and O. Iizuka. Initial results of a 50 kV electron beam writer EBM-4000 for a 90 nm node photomask. *J. Vac. Sci. Technol. B*, 21(6):2668–2671, 2003.

[49] M. Nakasuji, K. Kuniyoshi, T. Takigawa, and H. Wada. Simplified variable shaped beam for electron beam lithography. *J. Vac. Sci. Technol. A*, 3(2):424–429, 1985.

[50] A. V. Oppenheim and R. W. Schafer. *Discrete-Time Signal Processing.* Prentice Hall, Inc., Englewood Cliffs, N.J., 1989.

[51] H. Paik, E. J. Kirkland, and B. M. Siegel. Analytical calculation of electrostatic beam blanker performance. *J. Phys.E: Sci. Instrum.*, 20(1):61–66, January 1987.

[52] H. Paik, G. N. Lewis, E. J. Kirkland, and B. M. Siegel. Systematic design of an electrostatic optical system for ion beam lithography. *J. Vac. Sci. Technol. B*, 3(1):75–81, 1985.

[53] T. Patterson, J. Pankow, and N. R. Armstrong. Tetracyanoquinodimethane thin-films on Cu, Au, Pt, and SnS_2 – characterization by x-ray photoelectron-spectroscopy. *Langmuir*, 7(12):3160–3166, 1991.

[54] H. C. Pfeiffer. Variable spot shaping for electron-beam lithography. *J. Vac. Sci. Technol.*, 15(3):887–890, 1978.

[55] H. C. Pfeiffer and K. H. Loeffler. A high current square spot probe for micro pattern generation. In Pierre Favard, editor, *Proceedings of the 7th international congress on electron microscopy, Grenoble*, pages 63–64, Paris, France, 1970. Soc. Francaise de Microscopic Electronique.

[56] H. C. Pfeiffer and W. Stickel. PREVAIL – an e-beam stepper with variable axis immersion lenses. *Microelectronic Engineering*, 27:143–146, 1995.

[57] G. F. Rempfer. Unipotential electrostatic lenses: Paraxial properties and aberrations of focal length and focal point. *Journal of Applied Physics*, 57(7):2385–2401, 1984.

[58] R. Renoud, F. Mady, C. Attard, J. Bigarré, and Ganachaud J.-P. Secondary electron emission of an insulating target induced by a well-focused electron beam – Monte Carlo simulation study. *Physica Status Solidi A*, 201(9):2119–2133, 2004.

[59] Rösler and Brauer W. *Particle induced electron emission I*, volume 122 of *Springer Tracts in Modern Physics*. Spring-Verlag, Berlin; New York, 1991.

[60] T. A. Savas, M. L. Schattenburg, J. M. Carter, and H. I. Smith. Large-area achromatic interferometric lithography for 100 nm period gratings and grids. *J. Vac. Sci. Technol. B*, 14:4167–4170, 1996.

[61] T. A. Savas, S. N. Shah, M. L. Schattenburg, J. M. Carter, and H. I. Smith. Achromatic interferometric lithography for 100-nm-period gratings and grids. *J. Vac. Sci. Technol. B*, 13(6):2732–2735, 1995.

[62] J. Schou. Transport theory for kinetic emission of secondary electrons from solids. *Physical Review B*, 22(5):2141–2174, 1980.

[63] A. Shih, J. Yater, P. Pehrsson, J. Butler, C. Hor, and R. Abrams. Secondary electron emission from diamond surfaces. *Journal of Applied Physics*, 82(4):1860–1867, 1997.

[64] Y. Sohda, Y. Nakayama, N. Saitou, H. Itoh, and H. Todokoro. Electron optics for high throughput electron beam lithography system. *J. Vac. Sci. Technol. B*, 9(6):2940–2943, 1991.

[65] D. M. Tennant, R. Fullowan, H. Takemura, M. Isobe, and Y. Nakagawa. Evaluation of a 100 kV thermal field emission electron-beam nanolithography system. *J. Vac. Sci. Technol. B*, 18(6):2139 – 2145, 2000.

[66] A. V. Vannikov, A. D. Grishina, and M. G. Tedoradze. Dry photochemical etching of Bi films. *Journal of Materials Chemistry*, 2(7):755–757, 1992.

[67] A. V. Vannikov, A. D. Grishina, and M. G. Tedoradze. Dry photochemical etching of metallic films. *Mendeleev Communications*, 2(2):62–64, 1992.

[68] M. P. Villard. Sur les rayons cathodiques. *Journal de Physique Théorique et Appliquée*, 8(1):5–16, 1899.

[69] M. E. Walsh. *On the design of lithographic interferometers and their application.* PhD thesis, Massachusetts Institute of Technology, September 2004.

[70] M. E. Walsh and H. I. Smith. Method for reducing hyperbolic phase in interference lithography. *J. Vac. Sci. Technol. B*, 19(6):2347–2352, 2001.

[71] Oliver C. Wells. *Scanning electron microscopy.* McGraw-Hill, New York, 1974.

[72] J. L. Wilbur, A. Kumar, E. Kim, and G. M. Whitesides. Microfabrication by microcontact printing of self-assembled monolayers. *Advanced Materials*, 6(7-8):600–604, 1994.

[73] A. S. Willsky, G. W. Wornell, and J. H. Shapiro. *Stochastic Processes Detection and Estimation (class notes).* Massachusetts Institute of Technology, Cambridge, MA, 1998.

[74] Y. N. Xia and G. M. Whitesides. Soft lithography. *Annual Review of Materials Science*, 28:153–184, 1998.

[75] M. Yasuda, Nobuo Y., and H. Kawata. A Monte Carlo calculation of secondary electron emission from organic compounds. *Japanese Journal of Applied Physics*, 43(6B):4004–4008, 2004.